# Memory effects and yielding in a mesoscale model of amorphous plasticity

Dheeraj Kumar

## ▶ To cite this version:

Dheeraj Kumar. Memory effects and yielding in a mesoscale model of amorphous plasticity. Solid mechanics [physics.class-ph]. Université Paris sciences et lettres, 2023. English. NNT : 2023UPSLS075 . tel-04651902v2

HAL Id: tel-04651902
https://hal.science/tel-04651902v2

PSL
UNIVERSITÉ PARIS

THÈSE DE DOCTORAT
DE L'UNIVERSITÉ PSL

Préparée au laboratoire PMMH, à l'ESPCI
Physique et Mécanique des Milieux Hétérogènes

# Memory effects and yielding in a mesoscale model of amorphous plasticity
# Effets de mémoire dans un modèle mésoscopique de plasticité amorphe

Soutenue par
**Dheeraj Kumar**
Le 21 Décembre 2023

École doctorale n°564
**Physique en Île-de-France**

Spécialité
**Physique**

Composition du jury :

| | |
|---|---|
| Anke LINDNER<br>Professeure, ESPCI Paris | *Présidente du Jury* |
| Paulo E. ARRATIA<br>Professeur,<br>University of Pennsylvania | *Rapporteur* |
| Jérôme CRASSOUS<br>Professeur, Université de Rennes 1 | *Rapporteur* |
| Giuseppe FOFFI<br>Professeur, Université Paris Saclay | *Examinateur* |
| Anne TANGUY<br>Professeure, INSA Lyon | *Examinatrice* |
| Frédéric LECHENAULT<br>Chargé de recherche, ENS Paris | *Examinateur* |
| Muhittin MUNGAN<br>Professeur, University of Cologne | *Examinateur* |
| Sylvain PATINET<br>Chargé de recherche, ESPCI Paris | *Co-Directeur de thèse* |
| Damien VANDEMBROUCQ<br>Directeur de recherche, ESPCI Paris | *Directeur de thèse* |

ESPCI PARIS | PSL

*To my Parents*

# Declaration

I hereby declare that except where specific reference is made to the work of others, the contents of this dissertation are original and have not been submitted in whole or in part for consideration for any other degree or qualification in this, or any other university. This dissertation is my own work and contains nothing which is the outcome of work done in collaboration with others, except as specified in the text and Acknowledgements.

Dheeraj Kumar
September 2024

# Acknowledgements

I would like to thank my supervisors Profs. Damien Vandembroucq, Muhittin Mungan, and Sylvain Patinet for their guidance. I thank them for there patience and kindness throughout my thesis. I also thank the administration at ESPCI and PMMH especially Virginie, Alexandra, Fred, and Claudette for their help.

I thank Mert Terzi for discussions on the Preisach model. Former labmates and friends of Bureau 126: Matthias, PH, Hector, and Francesco. I thank them for there cheerful company and interesting conversations during coffee breaks and Les Arenes. I would also like to thank former members of our group Armand and Matthias for their help during my early days in Paris. Also Cristian, Anushree, Manon, Chloé, and Saurabh for there wonderful company.

I thank my friends: Arjun Sharma, Rahul Chajwa, Sumit Birwa, Yagyik Goswami, Niloyendu Roy, Chakram Sundar Deepak, and Biswadeep Roy. I have always cherished their company and their choice in music.

This thesis would not have been possible without the unconditional support of my parents. Finally, I thank my brother Shubham and sister Chanda for their support.

# Abstract

Amorphous solids under oscillatory shear, at small to moderate driving amplitudes under athermal quasi-static conditions, settle in reversible steady states such that further driving at the same amplitude leaves the system unchanged in particle positions. Beyond a critical amplitude of driving such periodic responses holding reversible plastic deformation, also known as limit cycles, disappear and the particles exhibit diffusive motion. This irreversibility transition presents typical features of a critical transition and has served as a probe to understand yielding in cyclically sheared amorphous solids. Recent particle scale simulations probed the nature of this transition as a function of initial degree of annealing of the glass sample. These shown that a threshold degree of annealing separates the ductile from a brittle failure of glass under cycle driving in an attempt to reconcile similar observations made under uniform shear.

As a first step, we develop a novel mesoscale elastoplastic model that can faithfully capture limit cycles as observed in experiments and atomic-scale simulations of amorphous solids under oscillatory shear. The novel ingredient is the quenched nature of the random landscape which governs the local threshold to plastic re-arrangements at the mesoscale level. With such a model, when we shear a glass sample at low driving amplitudes we always find limit cycles. If the driving amplitude is large no limit cycles are found. Our model shows that the transition between the two regimes becomes sharper with increasing system size.

By introducing a simple glass preparation protocol we tune the initial degree of annealing of the sample. For poorly annealed samples, the number of driving cycles required to settle in a limit cycle increases with the forcing amplitude and shows a power-law divergence as we approach the irreversibility transition from below. The measured exponent is consistent with those observed in particle scale simulations. Better annealed samples show a contrasting behavior. Limit cycles are either attained quickly in a few driving cycles or not at all. Such results further strengthen observations on particle scale simulations and mean-field models that predict a threshold degree of annealing separating brittle from ductile failure of glasses.

Using our model, we use a recently developed transition graph technique to study the response of amorphous solids under arbitrary shear deformation protocol. The technique projects the deformation trajectory of sheared amorphous solids on a directed transition graph. Nodes represent mechanically stable particle configurations while the edges as connections between them represent plastic re-arrangements. By looking at a key topological property of these transition graphs, we reveal the emergence of a phase-separation like process associated with the aging of the glass.

We also use our elasto-plastic model to study memory effects in amorphous solids. We begin by capturing memory of single amplitude of training and propose and demonstrate a method to read memory of shear direction. We compare the robustness of these memories with respect to read-out protocols and the amplitude of training. We also discuss the effect of frustrated interactions through multi-period limit cycles and their effect on memory of training amplitude. We compare and contrast the evolution of such memories as function of number of driving cycles imposed on the initial undeformed state. Depending on the ordering of training amplitudes, we also show that a sheared glass sample can remember multiple amplitudes of training. We show that a training sequence that encodes multiple memories can be manipulated to erase or recover memories of training amplitudes by altering the state on which a read-out operation is performed. We also study the effect of mechanical training on further encoding of memories of training amplitude in amorphous solids and discuss differences with mean-field models.

# Table of contents

# Chapter 1

# Introduction

## 1.1 Plasticity and yielding in amorphous solids

Amorphous materials are ubiquitous in nature. These include *hard* glasses such as oxide or metallic glasses, glassy polymers etc. but can also cover a wide range of *soft* materials such as colloidal assemblies, gels, emulsions, and pastes[21, 82]. The length scales at which the elementary constituents making up these solids live span from the Angstrom scale for the molecular glasses to millimeter scale for some of their soft counterpart. How these materials respond under externally applied stress or strain is a question of both industrial and fundamental importance that remains not well answered to the day[82, 106, 111].

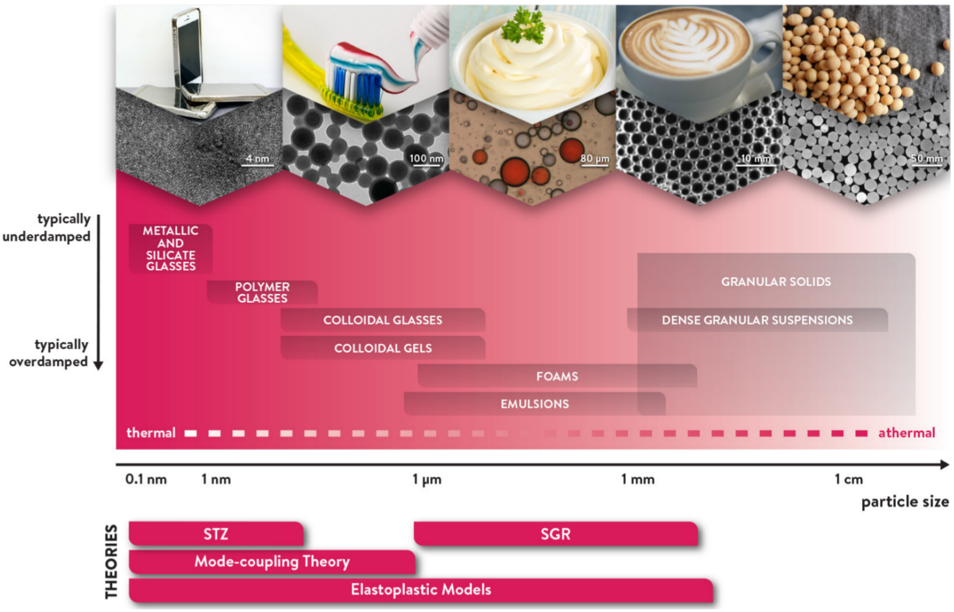

Fig. 1.1 An overview of range of amorphous solids with constituent particle sizes spanning several orders of magnitude and the corresponding damping regime of the constituents. Figure taken from [82].

## Elementary carriers of plasticity: Shear transformations

The lack of long-range order in amorphous solids makes understanding their mechanical properties more complex than their crystalline counterpart. Indeed, in contrast to crystalline solids[69], their structural disorder eliminates the notion of isolated defects as elementary carriers of plasticity. It was the pioneering work of Argon and Kuo with bubble rafts as an analog for metallic glass[6] who first showed that the elementary process of plasticity in such disordered solids are local events in space that involve the rearrangement of a few particles called *shear transformations* (ST). Strikingly, similar shear transformations have since been observed at different length scales including experiments on colloidal systems[110], granular media[4], concentrated emulsions[99], and many atomistic simulations of low-temperature shear[39, 75, 119, 121]. These studies have thus showed that the shear transformations are a universal characteristic and carriers of plasticity in amorphous solids.

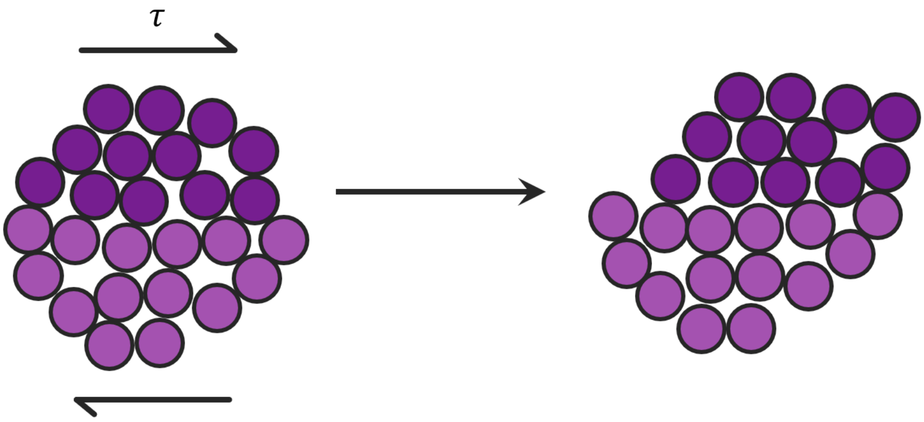

Fig. 1.2 Schematic of the elementary mechanism of plasticity in amorphous solids: localized rearrangement of a few tens of atoms. Figure taken from [112].

Fig. 1.2 shows a sketch of a localized atomic rearrangement of a few dozen of atoms that are seen as units of plasticity in amorphous solids as early proposed by Argon[5].

## Yielding in amorphous solids

At small deformations amorphous solids respond elastically, but the behavior becomes fluid like with a plastic-flowing state at large deformations[21]. This transition from the elastic response to the flowing state is known as *yielding*. An important and a well debated aspect[11, 32, 86–88, 92, 115, 117] of yielding under uniform shear is on the dependence on the initial degree of annealing of the amorphous solid. When subjected to uniform deformation, soft (or poorly aged) glasses yield to the flowing state in a smooth ductile manner while the hard (or well aged) glasses show an abrupt brittle response through a macroscopic stress drop. Yielding in the well annealed case, under athermal quasistatic shear (AQS), have been shown to follow a discontinuous non-equilibrium transition, accompanied by sudden appearance of system spanning shear bands[86–88, 117]. These studies considered the AQS response of amorphous systems at different degrees of annealing to understand the nature of yielding transition under uniform shear[86]. The response could be categorised into two groups: samples that were well-annealed showed that the yielding transition was abrupt while it was gradual for the poorly annealed samples. It was shown that that the two kinds of responses were separated by a critical degree of annealing with the corresponding critical point described to belong in the random-field Ising model universality class. Such an observation has been questioned regarding the existence of a well defined ductile to brittle transition under uniform shear[11].

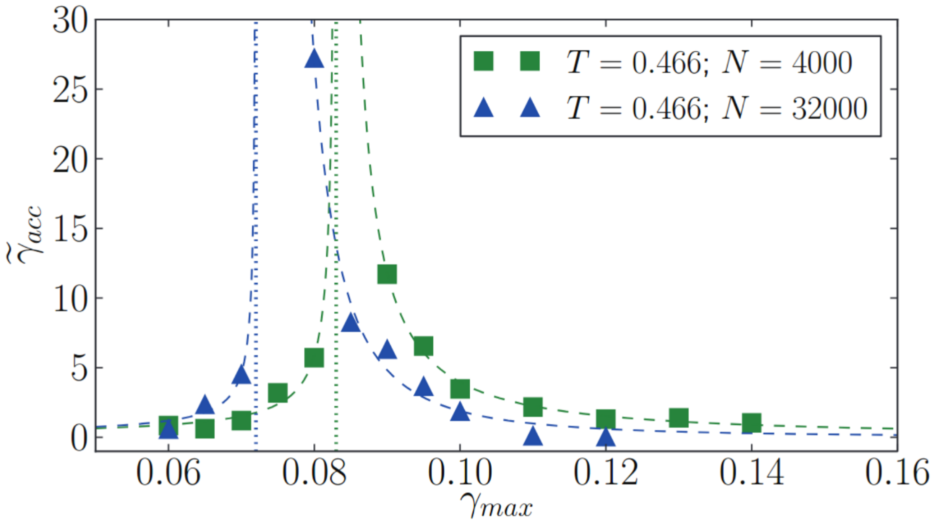

Fig. 1.3 Transient time (on the vertical axis) to steady state under cyclic driving versus strain amplitude (horizontal axis) at strains below and above the critical amplitude in particle scale simulations of 3-dimensional amorphous solids at two different system sizes for the same initial degree of annealing of the glass sample. The steady state is an arrested state when the driving amplitude is lower than the critical amplitude. The system settles in a diffusive state for driving amplitude above the critical value. The transient time diverges as the transition between the two regimes is approached. Figure taken from [42].

Yielding of amorphous solids under cyclic driving has also been studied. When subjected to cyclic shear loading, amorphous solids tend to either evolve into periodic response or reach a diffusive regime, depending on the value of the amplitude of the loading cycles. This transition presents typical features of a critical transition. In particular, power-law divergence of the number of loading cycles to reach the periodic response below the transition, as well as the power law dependence of the diffusivity above the transition have been observed both for atomistic and mesoscopic models [16, 42, 66, 90, 98, 103, 104, 129]. The features of the irreversibility transition depend on glass preparation [16–18, 129].

For example, in figure 1.3 taken from reference [42], we show the transient time required for the system to settle in a steady state as a function of driving amplitude in particle scale simulations of amorphous solids in 3-dimensions obtained at two different system sizes. The system settles in an arrested state for amplitudes below the critical amplitude. For amplitudes above the critical amplitude, the system dettles in a diffusive state with a well defined diffusion constant for the steady state. The transient time diverges as the transition between the two regimes is approached. We also note that the amplitude at which the transient time diverges depends on the system size.

One of the main objectives of this thesis is to understand yielding in cyclically sheared solids through a coarse-grained model of amorphous plasticity. In particular, we will be interested in studying the effects of system size and degree of annealing as we approach yielding from below. To facilitate this study, we will introduce a novel yet simple glass preparation scheme which will help us prepare and tune the initial degree of annealing of our glass sample in a continuous manner. We will then introduce a novel quenched landscape for driving under an athermal quasistatic protocol which plays a central role in capturing the non-trivial steady states known as *limit cycles* which have been observed in experiments[31, 34, 57, 96] and atomic scale simulations[42, 63, 98, 103] at strain amplitudes below and approaching the yield point.

## 1.2 Memory in cylically driven amorphous systems

Disordered systems with many interacting or non-interacting degrees of freedom can be trained under periodic driving to encode memory reflecting features of driving[59**?** ]. Examples include systems ranging from ferromagnets[10, 97, 113], crumpled sheets[116], spin glass[36] to dense amorphous materials[59]. The diversity of such materials can be classified based on the type of interactions that are at play in the dynamics of the individual constituents of the system. For example, rearrangements of individual constituents in systems with ferromagnetic interactions, such as ferromagnets, enable rearrangements in the same direction. On the contrary, systems with anti-ferromagnetic interactions suppress rearrangements in the same direction. A mixture of ferromagnetic and anti-ferromagnetic interactions, as in crumpled sheets, spin glass and dense amorphous solids, can give rise to rich dynamics under external forcing leading to various features of memory which are otherwise not present in purely-ferromagnetic or anti-ferromagnetic systems alone[127].

We show for example in figure 1.4, adapted from reference [116], the force response of crumpled sheet against applied displacement under oscillatory driving. Interaction among the mechanical bits of the system are a mixture of ferromagnetic and anti-ferromagnetic interactions. After a certain number of driving cycles, the system settles in an approximate limit cycle which is charaterised by a repeating feature encoded in the force jumps in the hysteresis cycle which happen nearly at the same displacement values. Such limit cycles can also show a form of memory known as return point memory (RPM) which is related to our studies in amorphous solids.

Experiments[54, 77] and particle scale simulations[43, 103, 104] have shown that dense amorphous materials under cyclic driving, in the absence of thermal fluctuations, below a critical strain amplitude settle in periodic states such that particle positions under stroboscopic measurements remain unchanged[59]. Such periodic states, also known as limit cycles, hold memory of the driving history such as the amplitude of cyclic driving which can be read using suitable read-out protocols[55].

Plastic rearrangements in amorphous solids have recently been modelled as hysterons, two-state hysteretic elements which switch states under the effect of an externally applied field[58, 72]. Such

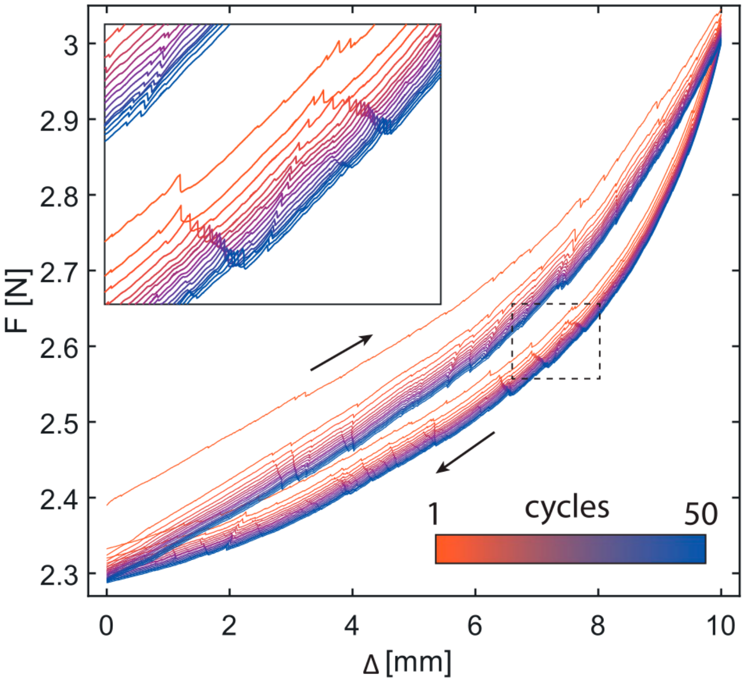

Fig. 1.4 Limit cycle in a cyclically driven crumpled sheet: Force as a function of displacement for a crumpled sheet under oscillatory drive. The response after a few driving cycles settles in an approximate limit cycle during which the force jumps occur at nearly the same displacement values. The response is hysteretic, interspersed with sudden force jumps throughout the cycle with near repeating features signalling the presence of a limit cycle. Figure adapted from [116].

models have complemented studies on memory formation in amorphous materials. The simplest such model, known as a Preisach model[97], uses a collection of non-interacting hysterons. The disorder is encoded in the threshold values (or swiching fields) of the external field at which hysterons change states which are drawn from a distribution. The model shows that under cyclic driving the system finds a limit cycle bearing memory of the training amplitude. However, the absence of interactions in the model leads to many features at odds with those observed in experiments and particle scale simulations on amorphous solids[59]. Among important differences, the model is guaranteed to hold return point memory (RPM). RPM, which we describe soon below, was proven to hold exactly for non-interacting/ferromagnetically interacting systems[113]. Amorphous solids violate RPM because the interactions between the potential plastic re-arrangements is of the Eshelby type which provide both positive and negative stress kicks on the surrounding material following a local plastic event[59]. Among other differences, the number of driving cycles to a limit cycle in a Preisach model can be at most 1 with period of limit cycles not exceeding unity. The same holds true for systems with purely ferromagnetic interactions[59]. Absence of interactions also eliminates the possibility of avalanches which play a key role in the dynamics of sheared amorphous systems.

Amorphous solids under shear accumulate plastic deformation through local plastic events. Plastic events in amorphous solids do not occur independently of each other. To improve on the Preisach model, interacting hysteron-based models have been invented to fill the gap. Interactions are incorporated in the model such that the applied field for a hysteron to switch between the two states depends on the state of other hysterons[58, 72]. The interactions are modelled as perturbations on the switching fields that allow the flexibility of introducing a mixture of ferromagnetic and anti-ferromagnetic interactions between individual hysterons. With such an ingredient, the model shows various features in line with sheared amorphous materials. Number of driving cycles to limit cycles and the corresponding period both exceed unity. Avalanches can be observed. RPM can be violated. When driven to a limit cycle, the model encodes memory of the driving amplitude. Hoewever, doubts have been cast over the possibility of such models to correctly capture the transients during external driving which are responsible for capturing yielding in cyclically sheared amorphous systems.

Elastoplastic models have also been used extensively in studies on sheared amorphous solids[106]. Many studies have been devoted to understanding the yielding transition in amorphous solids under unidirectional or uniform shear[82]. These models have only recently been accomodated to understand the yielding behaviour of cyclically sheared amorphous systems[60]. In particular, these models could capture the diveregence of the transient time to limit cycle at the critical amplitude of cyclic driving. Above the critical amplitude, the system becomes diffusive with a diffusion coefficient that shows a power law dependence on the amplitude of cyclic driving. One of the main aims of the thesis is to extend these class of models to also study memory effects in amorphous solids.

## 1.3 t-graphs

Quite recently, deformation pathways of amorphous solids in response to external shear under athermal quasi-static conditions have been mapped to directed transition graphs or t-graphs[78]. A t-graph is a collection of nodes which are connected by edges. In the context of driven amorphous solids, nodes represent mechanically stable particle configurations while the edges are connections between nodes representing avalanches triggered in response to external forcing. Given an initially stable configuration, and under athermal quasi-static conditions, a t-graph then encodes all the possible deformation trajectories obtainable under any combination of forward and reverse shear[78]. As has been demonstrated recently, such t-graphs serve as a valuable tool to understand various features relating to response of sheared amorphous solids[101]. Such t-graphs have also been constructed in experiments to study the effect of interactions on various possible topological features of t-graphs and their relation to return point memory in disordered materials[14]. Other simulation studies on t-graphs have concentrated on the topological features in the absence of interactions which become identifiers of motifs signalling weak Preisach like interactions in sheared amorphous materials and also served as a starting point to study memory capacity in such solids[101, 123].

In this thesis, with the novel ingredient that helps our elastoplastic model capture limit cycles, we generate t-graphs to further understand the role of sample preparation on the dynamics of sheared amorphous solids. This becomes all the more useful as elastoplastic models can easily access larger system sizes which is a limitation for particle scale simulations. Also, in our thesis we demonstrate a well defined glass preparation protocol that helps tune the initial degree of annealing of the sample. With such a preparation protocol we can also prepare initial samples that are very well annealed, a feature that is difficult to obtain in particle scale simulations. Thus, our studies using elastoplastic model set the stage for understanding the effect of degree of annealing, ranging from poorly annealed to very well-annealed glass samples, on the detailed dynamics of such solids under shear and possible role of finite size effects through the features encoded in and associated with the t-graphs. In this section, we briefly underline some key conclusions that such t-graphs have drawn in explaining the dynamics of driven amorphous solids[78, 101] and make connections to our own studies in this thesis where possible.

### 1.3.1 Transient time to limit cycles and the irreversibility transition

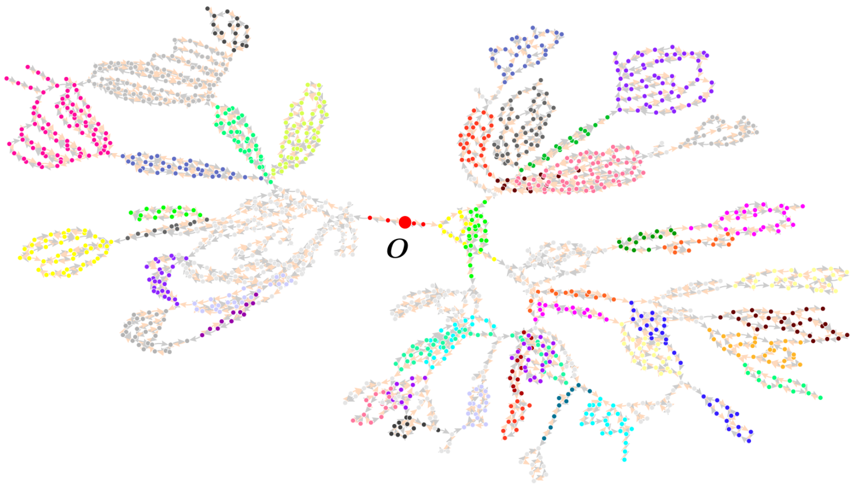

Fig. 1.5 A t-graph from our elastoplastic model for a ductile glass sample. Nodes represent mechanically stable states while the edges represent avalanches triggered under forward or reverse shear. The color of each node indicates the strongly connected component (SCC) of the graph that it belongs to and the initial state of the prepared glass has been marked with a larger red vertex labeled **O**. Nodes/vertices belonging to SCCs of size less than 10 have been colored in light gray.

Recent studies have focussed on the response of cyclically sheared amorphous solids as a complementary means to studying yielding in such solids[16, 53, 102, 103]. As a first step, these studies established a rather striking observation where, under the effect of cyclic driving, the system settles in a periodic state such that stroboscopic measurements on particle configurations remained unchanged. The reason this observation was taken with surprise is because within a cycle plastic re-arrangements occured in a manner precise enough to revert all re-arrangements and recover the state at the beginning of the cycle exactly. This implied that the trajectory of all the individual particles in response to plastic re-arrangements were such that their trajectories formed closed loops under a cycle of the externally imposed forcing.

Given the fact that a sheared amorphous solid has access to a plethora of metastable states, locking into a periodic response (also known as a limit cycle) was therefore considered a very non-trivial behaviour. The existence of limit cycles also implied that plasticity in driven amorphous solids become reversible. The existence of limit cycles is contingent on the amplitude of cyclic driving. If the amplitude is low the system always finds limit cycles. If the amplitude is large, limit cycles disappear and the system settles in a state such that particles exhibit diffusive motion. The two contrasting types of responses, existence of limit cycles at low driving amplitudes and diffusive state at large driving amplitudes, were infact found to be separated by a critical behaviour[102]. As the critical driving amplitude is approached from below, the number of driving cycles required to settle in limit cycles diverges like a power law. On the other hand, for driving amplitude greater than the critical amplitude a non-zero diffusion constant appears with a power law dependence on the driving amplitude. These have been well documented in the following references [16, 42, 66, 90, 98, 103, 104, 129].

t-graphs help us understand the response of amorphous solids as one approaches the critical driving amplitude from below[101]. More precisely, it explains the divergence of the transient time to limit cycles. To understand this, one must first understand a key topological property of t-graphs known as strongly connected components (SCCs) of the graph. An SCC is a collection of nodes (nodes are also termed as mesostates in the original study) such that it is possible to use a deformation trajectory to reach any node from any other in that SCC. This implies that a pair of nodes belonging to the same SCC are mutually reachable. In the language of t-graphs, a limit cycle is nothing but a collection of nodes connected by a deformation trajectory that form a closed loop on the t-graph. Thus, a limit cycle must belong to a single SCC by definition. The size of an SCC is then defined as the number of nodes that it contains. Coming back to the question, transient time to limit cycles diverges as one approaches the irreversibility transition. In a recent study, it was observed that the available sizes of SCCs at driving amplitudes close to the irreversibility transition were multiple standard deviations away from average SCC sizes that were actually available[101]. It must be noted that as the driving amplitude increases, number of plastic events increase during a cycle which implies that if a limit cycle is found it must also belong to an SCC atleast containing as many number of nodes as the number of stable configurations in the limit cycle. Diverging transients to limit cycles at critical amplitude was then understood as a search for an SCC of appropriate size which became increasingly rare to find under external forcing[101].

We end our discussion by showing show a t-graph extracted from our simulations of elastoplastic model for a ductile glass sample in figure 1.5. As stated before, each node represents a mechanically stable state. A node has two outgoing transitions, one under forward shear (in gray) and another under reverse shear (in orange). Nodes belonging to the same SCC use the same color. The t-graph encodes various possible deformation trajectories under forward and reverse shear beginning from the initial state **O**. These include trajectories leading to SCCs, the carriers of limit cycles. In Chapter 5, using the t-graphs obtained from our elastoplastic model we will show, among other things, how the irreversibility transition can impose strong constraints on the structure of the t-graphs when combined with the physical properties associated with the dynamics of sheared amorphous solids. We also contrast such a dependence on degree of annealing of the glass sample.

### 1.3.2 Reversible and irreversible transitions

Existence of limit cycles under periodic forcing implies that particle positions remain unchanged stroboscopically. This means that plastic events belonging to a limit cycle are reversible. However, plastic events also occur during the period in which the search for limit cycle is not complete. Such plastic events have been termed as irreversible because the system does not visit the same states during the transient. However, both reversible and irreversible plastic events involve particle re-arrangements and it is therefore difficult to distinguish them from each other. t-graphs help distinguish reversible from irreversible plastic events unambiguously. To understand this let us revisit the SCCs. Since any pair of nodes belonging to an SCC are mutually reachable, it must mean therefore that any plastic event or avalanche (represented by an arrow on the t-graph in figure 1.5) belonging to an SCC must be reversible. In other words, an avalanche or plastic event belonging to an SCC is part of atleast one deformation trajectory that forms a closed loop on the t-graph in that SCC such that the effect of the avalnche can be undone completely. Such a plastic event must therefore be reversible. On the other hand, plastic events connecting nodes of different SCCs are irreversible. This means that there is a deformation path consisting of a plastic event, the irreversible plastic event, leading from a node in an SCC to a node in another SCC but no deformation path back. t-graphs thus make a clear distinction between plastic events which are reversible and those which are not.

For example, in figure 1.5 arrows connecting nodes of the same color represent plastic events that are reversible while those connecting nodes of different color are irreversible. In Chapter 4, we will demonstrate through our elastoplastic model that amorphous systems under cyclic driving can learn features of driving, for example the amplitude. We will explain some of these features using the distinction between reversible and irreversible transitions and their role in memory formation in driven amorphous systems. Additionally, we will use this distinction to understand some of our results in Chapter 5 where we study the effect of degree of annealing and system size on the toplogical features of t-graphs.

### 1.3.3 Return Point Memory

In this thesis, we will study memory effects in driven amorphous systems using our elastoplastic model. In contrast to amorphous systems, systems possessing purely ferromagnetic or no interactions are guaranteed to hold return point memory[113]. Although return point memory can be violated in systems possessing anti-ferromagnetic interactions[14, 127], driven amorphous solids can show behaviour consistent with RPM, if not perfectly[78]. In case of amorphous solids, the change in stress experienced due to a local plastic event elsewhere in the system can be negative or positive depending on the position with respect to the re-arranging site. Such interactions can then be seen as a mixture of ferromagnetic and anti-ferromagnetic interactions in space. The presence of anti-ferromagnetic interactions in amorphous solids raises the expectation that RPM be violated. However, recent studies used a t-graph construction to map out the deformation trajectory of sheared amorphous solids to observe a near-perfect RPM[78]. Since we interpret our results on memory effects in light of RPM, below we describe what it means.

We demonstrate RPM through a non-interacting Preisach model[97] for ferromagnets that describes the response in magnetisation of the system driven by an external magnetic field. It is a non-interacting model useful to understand memory formation in periodically driven disordered systems. The basic building block of such a model are what are known as hysterons. A hysteron represents a magnetic domain which can take a $+1$ or $-1$ state. The switching of state of a hysteron is determined by its threshold values $H^+$ and $H^-$ which follow a constraint $H^+ > H^-$ implying a dissipative system. Further, to account for disorder in the material the thresholds have a distribution. If the external magnetic field $H > H^+$ then the hysteron is in $+1$ state. It takes a $-1$ state if $H < H^-$. The state of the hysteron depends on the driving history when $H^- < H < H^+$. A switching of state of a hysteron does not affect other hysterons implying that the system is non-interacting. A collection of such hysterons under the effect of external magnetic field displays return point memory.

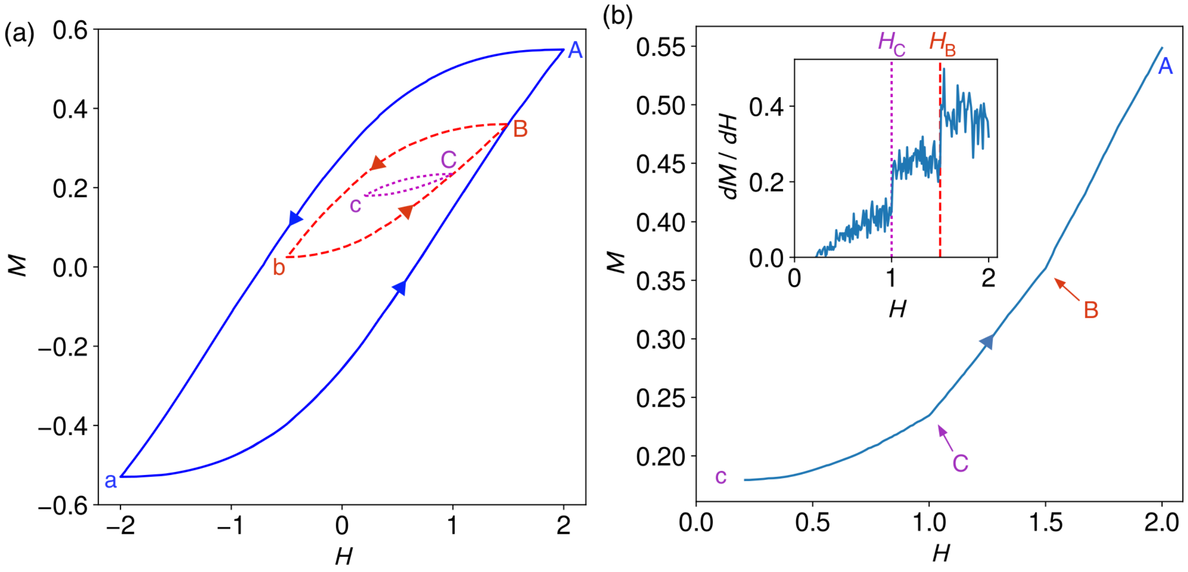

Fig. 1.6 (a) Average magnetisation $M$ of a simulated Preisach sample as the external field $H$ is varied. (b) Signature of the memories at $H = H_C$ and $H = H_B$ as the external field is varied from $H_c$ to $H_A$. The inset shows signatures of memories as discontinuity in the slope $\frac{dM}{dH}$ at $H = H_C$ and $H = H_B$. Figures adapted from [59].

RPM in Figure 1.6 (a) is visible in the driving sequence that takes the sample from $a \rightarrow B \rightarrow b \rightarrow B$. RPM means that returning the external field $H = H_B$ will always restore the system to the same microstate when it first left the outer loop (in blue), provided the external field during the excursion, for example on the inner loop, obeys the constraint that $H_a < H < H_B$. The system holds memory of the turning point in the external field as long as the previously applied extremum values (or turning points) were not exceeded. The sub-sequence $a \rightarrow B \rightarrow b$, which has a turning point at $H = H_B$, has created a memory of the state at $H = H_B$ and persists as long as $H_a < H < H_B$ is satisfied.

RPM also opens the possibility of storing multiple memories. A driving sequence $b \rightarrow C \rightarrow c$, as shown in Figure 1.6 (a), obeying the constraint $H_b < H < H_C$ encodes a second memory, that of the state at $H = H_C$. As the external field is swept from $H_c$ to $H_A$, the memories of the states at $H = H_C$ and $H = H_B$ are seen as clear discontinuities in the slope $\frac{dM}{dH}$ at the corresponding points. The nested structure of loops in Figure 1.6 (a) imply that storage of multiple memories of $H$ demand a nested ordering on the turning points in $H$, which are the values being stored, to be satisfied. We refer the reader to references [59, 114] for a more detailed description of the subject. Finally, we note that RPM can be violated in systems which contain both ferromagnetic and anti-ferromagnetic interactions. RPM violation in the Figure 1.6 (a) would mean that driving in the external field through the sub-sequence $H_b \rightarrow H_B$ will not end in the same state as it when it the left the parent loop (in blue) at $H = H_B$ during the excursion $B \rightarrow b$. Such RPM violations, as observed in particle scale simulations on amorphous solids [78], prohibit a strict hierarchical nesting of loops within loops like in Figure 1.6 (a).

Systems with interactions ranging from ferromagnets [10, 97, 113] to high temperature superconductors [89] also show RPM. Interactions between individual elements of these systems are cooperative meaning that a local state change encourages other elements to change their state in the same direction. A simple example is the well-studied Random Field Ising Model (RFIM) for ferromagnets in which the the individual spin sites could either take a +1 or -1 state. The model uses cooperative interactions meaning that a spin flip to +1 state encourages others to do so. Systems with such kind of interactions were proven to hold return point memory [113]. RPM allows a system to remember a nested series of turning points in the externally applied driving field thus permitting the storage of multiple amplitudes of training [59]. The nesting of turning points in the external field implies that there is a constraint on the order in which these turning points can be arranged. Storage of multiple amplitudes thus demand that such a constraint on the ordering of turning points be satisfied.

In Chapter 4, using our elastoplastic model, we will also show that cyclically driven amorphous systems under variable amplitude driving can encode memory of multiple amplitudes of training. We will manipulate such a training sequence to elucidate responses that are single shear cycle apart to erase/recover some or all memories, respectively, of training. With this, we raise the question whether the trained state holding multiple memories of training can hold features effectively that of ferromagnetic systems and thus return point memory? Our results will leave certain open questions like the possibility of correlations in the soft-spots which are active within the limit cycles in the light of observations made under multiple memory case.

## 1.4 Summary and Overview

Yielding and memory effects in cyclically driven amorphous systems have so far been studied in experiments and particle scale simulations. These studies, performed under athermal-quasistatic (AQS) conditions, have highlighted the role of non-trivial steady states, i.e. limit cycles, in how these systems yield and encode memories of training. Limit cycles, as observed under a shear cycle, visit the same sequence of metastable states implying that stroboscopic measurements on particle configurations remain unchanged. Moreover, such limit cycles can have period $T > 1$ such that reaching the same state requires $T$ driving cycles. Given the structural disorder of amorphous solids such observations remain highly non-trivial. In addition to holding memory of training, such limit cycles also remain sensitive to the amplitude of cyclic driving and disappear beyond a certain critical amplitude which marks the irreversibility transition. Hysteron-based models have only recently been developed to capture and explain some of these observations. These models underline the importance of nature of interactions in determining limit cycles, associated periods, and memory effects. However, they do not capture and explain many observations made on cyclically driven amorphous solids including yielding under cyclic driving and the effect of sample preparation. Coarse-grained elastoplastic models, on the other hand, are commonly used in studies on yielding in sheared amorphous solids. In this thesis, we utilise simple and novel ingredients to develop a mesoscale elastoplastic model capable of capturing limit cycles to study the irreversibility transition in cyclically driven amorphous solids. A key ingredient is a quenched local landscape for potential soft-spots in the system which allow the possibility of finding limit cycles. We also use a tunable preparation protocol to generate glass samples with different degrees of annealing. This helps us understand the nature of irreversibility transition for glass samples with different degrees of annealing. Using the same coarse-grained model, we also study memory effects in cyclically sheared amorphous systems. In our studies on memory effects, we first show that under suitable driving/training protocols our model can hold memories of single and multiple amplitudes of training and then setup various studies thereafter. Additionally, we perform a t-graph construction of the AQS response of sheared amorphous solids in our elastoplastic model to understand the role of annealing of the glass sample in determining the response of such solids to arbitrary shear driving protocols. In particular, we combine topological features of the t-graph with physical properties of sheared amorphous systems to reveal the effect of degree of annealing of the glass samples. Through these studies we probe the interplay of sample preparation and finite size effects on the structure of t-graphs.

This thesis is organised as follows:

(i) In chapter 2, we discuss general ingredients of various elastoplastic models (EPMs) popular in literature aimed at capturing sheared response of amorphous solids. We then describe features of our EPM which includes a quenched landscape for shear driving.

(ii) In chapter 3, we introduce a simple and physically motivating glass preparation protocol that helps us tune the initial degree of annealing of the glass sample at the mesoscale level. We then perform unidirectional (or uniform) shear tests on these samples as a test on our preparation protocol. We then perform extensive simulations of the mesoscale model to study the response of cyclically sheared amorphous solids for different degrees of annealing and system size to probe the nature of the irreversibility transition.

(iii) In chapter 4, we study memory effects in cyclically sheared amorphous solids using our elastoplastic model. We begin by showing that our model is able to capture single and multiple memories of driving/training amplitude under suitably designed training and read-out protocols. These studies are complemented by studying the effects of multi-periodic limit cycles and large driving amplitudes spanning across the irreversibility transition to question the robustness of such memories.

We show that memory of training can be revealed in novel ways that have remained unexplored in the literature so far. We complement some of our results using observations from our studies on t-graphs. We also study the effect of prior training under cyclic driving on further encoding of memories in amorphous solids and attempt to make some comparisons with existing results from mean-field hysteron-based models.

(iv) In chapter 5, we capture the transition graph representation of AQS response of amorphous solids using our elastoplastic model. We study some of the key topological features of these transition graphs and combine our observations on plasticity and yielding in amorphous solids to reveal the effect of degree of annealing of the glass samples. We also study the effect of system size on the structure of t-graphs. We also complement our observations from t-graphs obtained from atomic scale simulations of model amorphous solids.

(v) In chapter 6, we summarise the main findings of our thesis and discuss potential directions which could further be explored.

Results of the thesis presented in Chapter 3 and Chapter 5 belong to our published work [61]. Results of the thesis presented in Chapter 4 is part of an article under preparation.

# Chapter 2

# Mesoscopic Elasto-Plastic Model

In this chapter, we will introduce the building blocks of the elastoplastic model (EPM) used in the thesis. The first part of the discussion will pertain to common ingredients of EPM with typical variations in the literature complemented with references. This will be followed by a brief history of such models and their extensions in the studies of yielding and rheology of amorphous solids. Finally, we will introduce the details of our elastoplastic model in the context of the problems addressed in the thesis. The details of our model can be found in Section 2.3 onwards.

## 2.1 Building blocks of elasto-plastic models

In this section, we first highlight general ingredients used in building mesoscale models and then motivate and underline the features we choose to pick for this thesis.

Studies on amorphous solids using elastoplastic models are built on the idea of dividing the material into mesoscopic cells which can alternate between elastic and plastic states. For example, see figure 2.1 for a schematic illustration. A cell switching from an elastic to a plastic state is considered a proxy for shear transformations which mimic local plastic rearrangements in space. This local state switching induces stress perturbations in the system, allowing the cells to interact with each other elastically, forms the basis of these models. The main aim of these models has been to use minimal ingredients, and thus catch applicability in a wide range of materials, to reproduce various universal properties as observed in the mechanical response of amorphous solids in experiments and atomistic simulations [82].

EPM models [9, 23, 70, 81, 82, 94] share some key common features listed below:

- A local yield criterion to determine the onset of a plastic rearrangement.
- An elastic coupling that accounts for the effect of a plastic rearrangement on the surrounding medium.
- An evolution rule for the local yield criterion following plastic rearrangements to account for local structural changes.

- A flow rule that associates slip amplitude and/or a time scale to these plastic rearrangements. Various possibilities exist, for example: the model can be built in the athermal quasistatic limit or time and temperature effects could be put in by using, for example, a kinetic Monte Carlo algorithm.

Below, we expand on the points mentioned above.

### 2.1.1 Onset of local plastic transformation

Most of the EPM models, including the one used in this thesis, are scalar in nature. This means that the tensorial nature of local stress or strain is neglected in the mesoscopic cells making up the system. Such an assumption holds only when local volume changes can be neglected and the externally applied shear acts uniformly on the system. The external deformation then simplifies to affecting only the deviatoric part of the local stress or strain tensor, thus fitting the scalar description [82]. The scalar approximation thus amounts to consider that at microscopic scale (within a cell) the material slips along the very same direction as the one imposed by the external loading. The criterion determining the onset of shear transformations then becomes simpler.

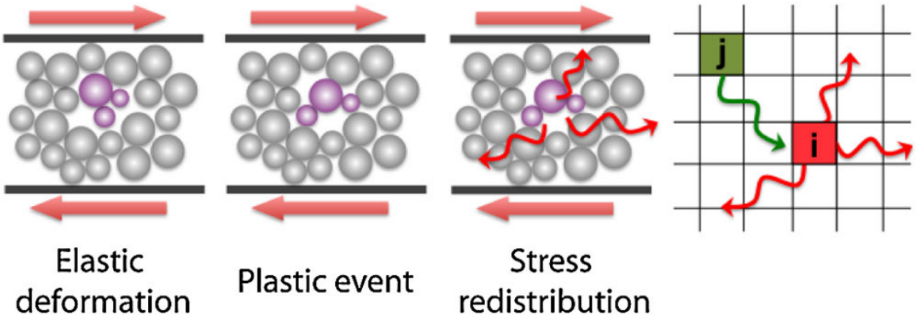

Fig. 2.1 A cartoon depicting a local plastic event in amorphous media. Such an event comprises an elastic response followed by mechanical instability resulting in a plastic rearrangement. This plastic rearrangement results in a stress redistribution throughout the system that may further trigger a cascade of such events. Figure taken from [20].

#### Local yield criterion

Plasticity in amorphous solids is known to proceed through shear transformations which are localized plastic rearrangements in space. In scalar EPMs, the onset of such rearrangements is modelled by assuming a stress-based criterion:

$$\sigma(x) = \sigma^{+}(x). \tag{2.1}$$

where, $\sigma(x)$ is the local shear stress and $\sigma^+$ the local yield stress at a cell position $x$, implying that a local plastic event is triggered when $\sigma(x) \geq \sigma^+(x)$. Such a criterion assumes that thermal effects are negligible [82].

Local yield stresses can be chosen to be spatially homogeneous [94, 95] or heterogeneous [9, 33, 51, 120]. In the case of spatially homogeneous yield stress, cells do not yield instantly upon exceeding the threshold but do so with some fixed rate. The associated time delay is thought to capture the stochasticity of rearrangement processes in the system. On the other hand, the heterogeneous picture treats the local yield stress as random variables drawn from some statistical distribution without correlations. In this case, a cell yields instantly upon exceeding the threshold. In the thesis, we will always concern ourselves with disorder of the latter type.

Elastoplastic models have also been proposed that take thermal activation of plastic events into account. Such a criterion introduces a probability for activating plastic regions following $\propto \exp(-F/T)$, where $F$ is the free energy required for the local plastic event and $T$ is the temperature [24].

### 2.1.2 Evolution rule for the local yield criterion

Another essential ingredient in the EPMs concerns the evolution of the yield criterion. Once a plastic rearrangement has taken place, the local structure of the rearranging region changes which may change the local yield stress. In some models, the local yield stress does not change post-plastic event [24, 48, 49, 94, 95] while in others a new value is drawn from a stationary distribution without correlation [9, 120]. In this thesis, we will resort to the second option and consider only stationary renewal threshold distributions after local yielding. Finally, new models deal with the gradual evolution of this renewal law with plastic deformation in order to be able to take into account the effect of the different preparation protocols on the mechanical response [27, 124].

The above three ingredients can be summarised in figure 2.1. The figure shows a cartoon of a potential STZ local in space under the effect of external loading. It first responds elastically before reaching a critical state and suffering a plastic rearrangement. This transition is marked by an irreversible change of neighbours, the effect of which is felt throughout the system through long-range stress distribution. Qualitatively, the same figure then demonstrates an EPM approach of dividing the system into individual cells which act as candidates for such events and interact with each other via Eshelby stresses, as disussed in the following sections.

### 2.1.3 Interaction via the elastic matrix

Since EPMs aim to capture the collective effects of shear transformations (STs), their interactions must be specified. These interactions result due to the stress distribution following a plastic event to restore mechanical balance. Indeed, successive STs are not independent, as evidenced in numerical simulations and experiments [64, 76]. This mechanism is based on the surrounding medium's elastic nature, which is key to transmitting elastic waves post a local yield event. Continuum equations of elasticity [62] can then be used to determine the shear stress increment caused by the local rearranging zone through what is known as the elastic propagator $G$. Eshelby first solved this plastic inclusion problem in 3D [37], where an ellipsoidal inclusion of arbitrary size was considered to be embedded in an elastic medium. Eshelby's results highlighted two important features of the propagator $G$ [94], first it is long-range, and second it has a varying sign. For example, the stress field induced by a plastic inclusion under pure shear, in the far field has the form: $ACos\,4\theta/r^2$.

EPMs, including ours, use this equation as the basis for interaction among the mesoscopic cells. As a demonstration, we show in figure 2.2 the stress redistribution due to a plastic rearrangement in the central block. One notices a striking agreement between all the three approaches: Experiments, Simulations, and theory.

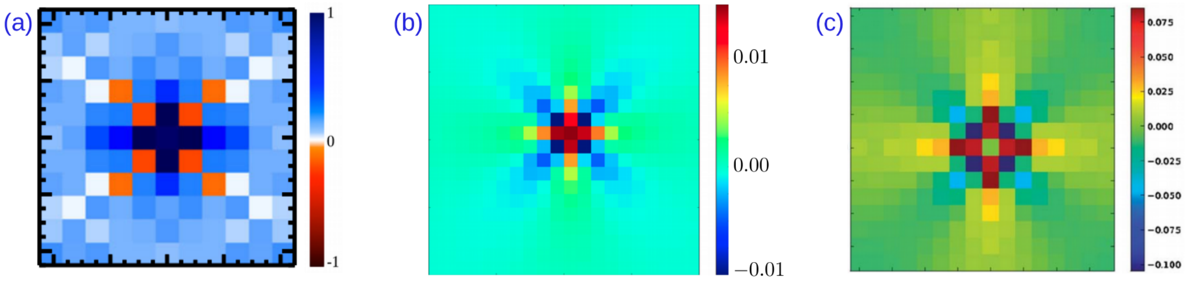

Fig. 2.2 Average stress redistribution due to a plastic event. (a) In an experiment on dense emulsions. (b) In an atomistic simulation using a binary Lenard-Jones glass. (c) In Theory: Far field solution of an Eshelby inclusion. Figure taken from [82].

Analytical results have also been achieved by employing mean-field extensions of EPM [46, 118]. These models ignore the spatial features of the propagator G. These can use a constant stress distribution throughout the system following a local slip event or statistical variants in which the elastic responses following a slip event are drawn from an uncorrelated random distribution [82]. However, the relative simplicity of these models in treating the stress redistribution results in failure to capture the build-up of spatially correlated plastic events, for example, the shear banding phenomena in brittle glasses.

### 2.1.4 Driving

One can make two main choices while driving the system through external loading. The first method is athermal and quasistatic in nature which ignores thermal and rate effects [9, 33, 95, 120]. The second method, also known as the kinetic Monte Carlo algorithm, considers thermal and rate effects [24, 49, 50]. We will use the former method in this thesis.

To mimic athermal quasistatic driving protocol, we use an extremal dynamics (Baret et al., 2002; Lin et al., 2014b; Talamali et al., 2012) to shear our mesoscopic system. At each step, this driving protocol triggers one and only one plastic event resulting in a vanishing shear rate. In the algorithm, starting with a mechanically stable state, the weakest site in the system is identified by finding the cell with the smallest value of $\sigma^+(x) - \sigma(x)$. The cell is then subjected to a local slip event followed by a stress distribution according to the Eshelby kernel. The local yield stress is updated according to the evolution rule mentioned in section 2.1.2. From this single destabilisation an avalanche of plastic events can occur. The process is repeated when the avalanche terminates.

## 2.2 A brief history of mesomodels

Before we discuss our model in detail, we give a brief survey of mesomodels for the reader to contrast various historical objectives of elastoplastic models put in the context of the problems studied in the later chapters of the thesis.

To our knowledge, the first discrete model to study plasticity in amorphous solids was proposed by Argon and Bulatov in 1994 [24–26]. This model was based on an earlier work of Argon and Kuo [6], which showed that the elementary unit of plasticity in such solids is the localized rearrangement of particles in space called shear transformations. The model tesselated the material into hexagonal cells forming a hexagonal lattice. Once a shear transformation was triggered at a cell location due to fluctuations in local stress, stress released by the local plastic event would be redistributed throughout the system according to the Eshelby propagator resulting from mechanical equilibrium constraint. The effect of temperature on plasticity was captured by allowing plastic events to be thermally activated through an activation probability $\propto \exp(-F/T)$, where $T$ is temperature and $F$ is the free energy barrier of local plastic rearrangement. Homer and Schuh [49, 50] proposed an extension of this model by introducing a kinetic Monte Carlo method to follow the dynamics of plastic deformation and study their spatial correlations in the amorphous media.

Baret et al. [9] came up with another model to study amorphous plasticity but instead at zero temperature. It used structural disorder and long-ranged interactions for stress redistribution following plastic events. The model displayed critical behaviour much like statistical models for earthquakes [13, 28]. In close spirit, Picard et. al. [95] studied the spatiotemporal behavior of a yield stress fluid using an athermal model with quadrupolar elastic interaction between the cells. This model was the first model to study finite shear rate rheology with the aim of capturing the Herschel-Bulkley (HB) law. In this model, disorder was introduced through rates at which the cells switched from elastic to plastic states. The model showed consistency with experimental results by predicting flow governed by spatially correlated plastic events with diverging correlation length as the shear rate decreased to vanishing values. Interestingly, Nicolas et. al. [83] in 2014, building on the ideas of the Picard model, successfully recovered the HB law by instant trigger of plastic events beyond a threshold stress for which a distribution was defined. The plastic events in the model were given a fixed duration to relax locally.

Mean field versions of elastoplastic modelling have also proved valuable in understanding plasticity in amorphous solids. These models allow for an analytical extension of elastoplastic models as they discard correlated dynamics of plastic events. One of the most popular among such models is the so-called Hébraud-Lequeux (HL) model [118] designed for athermal materials at fixed shear rate rheology. The HL model uses Gaussian noise to model the effect of stress redistribution due to slip events on the surrounding medium. It can, however, be shown that the Eshelby stress propagator leads to a power-law distributed noise [71]. This power law distribution is not surprising if one looks at the singularity present in the far field solution of the Eshelby inclusion, which becomes more pronounced in the low shear rate limit due to increasingly correlated plastic events. Inspite of this simplification, the HL model was able to recover the transition between an arrested state to a flowing state through a Herschel-Bulkley law [47], which fits well for the stationary flow regime of yield stress fluids [21]. The non-Gaussian nature of the mechanical noise was later studied and confirmed through a more general HL model [71].

The Kinetic Elastoplastic (KEP) Theory of Bocquet et al. [20], building on the HL model, predicted a decrease of correlation length (dictated by the spatial plastic activity) with shear rate as one moved away from the dynamic yield stress through the Herschel-Bulkley law with an exponent 1/4, in contrast to work of Lemaıtre and Caroli [67] based on modulecular dynamics simulations, who predicted an exponent of 1/2.

The above discussion on mean field models is for athermal materials. In contrast, the Soft Glassy Rheology model of Sollich et al. [118] treats mechanical noise as an effective temperature to handle the effect of slip events. More precisely, cells below yield stress are assigned an yield rate according to an Arrhenius law while the unstable ones are made to slip immediately. As the temperature in the model is reduced, the shear rate dependence of steady state stress transits from a Newtonian regime to a power law regime. Decreasing the temperature further, a yield stress emerges recovering the celebrated HB law for athermal soft amorphous solids.

## 2.3 Our Model

In this section, we will introduce our elastoplastic model which, among other details, bears the novel ingredient that is a local landscape that is quenched in the direction of plastic deformation. Such an ingredient is central to capturing limit cycles and study yielding and memory effects in cyclically sheared amorphous solids.

We consider a scalar 2D lattice-based mesoscale elasto-plastic model. The physics of this class of models relies on the coupling between a threshold dynamics and an elastic interaction induced by the incremental local plastic slip which arises as a result of a mechanical instability [82]. We use here a variant of the model introduced in Refs.[120, 125, 126].

We consider a square grid of $N \times N$ cells of size $a \times a$. The model is scalar, so that we account for one and only one shear direction, along which we can shear the system forward and backwards. We assume a uniform shear modulus $\mu$. Each individual cell $(i, j)$ is characterized by a stack of local elastic branches indexed by a variable $\ell$, each of which relates the local stress $\sigma_{ij}$ to the local strain $\varepsilon_{ij}$, as shown in Fig. 2.3. The stability of each such local elastic branch $\ell$ is limited by two bounds: a maximum stress threshold $\sigma^+_{ij,\ell}$, and a minimum stress threshold $-\sigma^-_{ij,\ell}$. Note that in order to ease notation, whenever no explicit reference to a particular branch number $\ell$ is made, we will omit it in the following. The two thresholds $\sigma^+_{ij}$ and $\sigma^-_{ij}$ are drawn from a random distribution with support in $\mathbf{R}^+$ so as to ensure $-\sigma^-_{ij} < \sigma^+_{ij}$, i.e. the existence of a stability domain for the cell $(i, j)$. Whenever the local stress $\sigma_{ij}$ overcomes one of the two bounds, the cell experiences a plastic event and its stability domain is shifted to a neighboring elastic branch. Since the cell is surrounded by other cells, and can be seen as an Eshelby inclusion within an elastic matrix, this plastic event induces a stress redistribution in the system so that other cells can get destabilized.

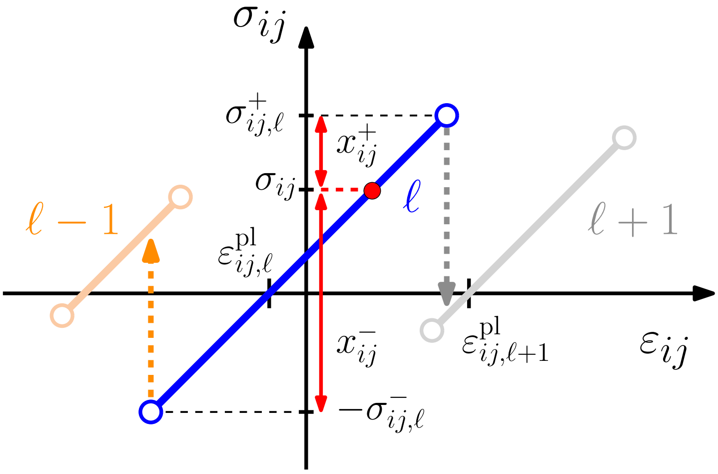

Fig. 2.3 Local elastic branches associated with a cell $(i,j)$. Each elastic branch $\ell$ is characterized by a pair of stress thresholds $\sigma^{\pm}_{ij,\ell}$ and a plastic strain $\epsilon^{\rm pl}_{ij,\ell}$, which prescribe the behavior of the local stress $\sigma_{ij}$ under elastic strain $\epsilon^{\rm el}_{ij} = \epsilon_{ij} - \epsilon^{\rm pl}_{ij}$, as shown for the branch labeled $\ell$ in the figure. When the stress reaches the upper or lower stress threshold, a transition to the corresponding neighbouring branches, $\ell \pm 1$ occurs. The current stress state of the cell is denoted by a red filled symbol on the elastic branch $\ell$. This allows us to define the local plastic strengths $x^{+}_{ij} = \sigma^{+}_{ij} - \sigma_{ij}$ and $x^{-}_{ij} = \sigma^{-}_{ij} + \sigma_{ij}$ which give the distance to threshold in the forward and backward directions, respectively. The slopes of the local branches are identical and equal to $2\mu$.

In the present model, the local stress $\sigma_{ij}$ experienced by the cell $(i,j)$ originates from two distinct contributions: a global stress $\Sigma$ due to the external loading, and an internal stress associated to the interactions with other cells, so that $\sigma_{ij} = \Sigma + \sigma^{\rm int}_{ij}$. The latter contribution fluctuates spatially and is by definition of zero average so that we have $\overline{\sigma^{int}_{ij}} = 0$, and therefore $\overline{\sigma_{ij}} = \Sigma$. Here $\overline{A}$ denotes the spatial average of the observable $A$.

Due to the external loading and the stress interactions, the local stress $\sigma_{ij}$ is in general non-zero so that the amount of (external) stress that needs to be applied in order to reach one of the boundaries of the elastic branch is not a priori equal to the stress thresholds $\sigma^{+}_{ij}, \sigma^{-}_{ij}$. Instead, it is given by the *local plastic strengths* in the positive and negative directions, which we define as $x^{+}_{ij} = \sigma^{+}_{ij} - \sigma_{ij}$ and $x^{-}_{ij} = \sigma_{ij} + \sigma^{-}_{ij}$, respectively. Note that for a mechanically stable configuration we require that $-\sigma^{-}_{ij} < \sigma_{ij} < \sigma^{+}_{ij}$, so that the quantities $x^{\pm}_{ij}$ must be positive in that case.

The separation $\Delta\varepsilon$ between two neighboring local elastic branches that belong to a given cell $(i,j)$ defines the local plastic strain $\varepsilon^{\rm pl}_{ij,\ell}$ experienced by the cell after the local stress has reached the threshold in one or the other direction.

### Stress interaction

Local plastic strains are generated within an elastic matrix (the other cells of the lattice). This incompatibility induces an internal Eshelby stress field of quadrupolar symmetry [38]. Since we assume homogeneous elasticity, the elastic response to a unit plastic slip can be computed once and for all. The internal stress thus directly arises from the convolution of the field of plastic strain with the Green function of Eshelby stresses. The latter is computed from the discrete Fourier Transform of the analytical solution in the reciprocal space. Details on the implementation and a discussion can be found in Refs. [120, 125].

The typical stress drop associated to a rearrangement of plastic strain $\Delta\varepsilon$ is of order $\mu\Delta\varepsilon$. For the sake of comparisons with atomistic simulations, we consider here $\mu = 10$, a typical value observed in Lennard-Jones binary model glasses [91, 103]

### Random landscape

The stress thresholds are drawn from a random distribution $P(\sigma^{\pm})$. Here we consider a Weibull distribution of parameters $\lambda = 1.0, k = 2.0$, where $\lambda$ and $k$ are constants in the cumulative density function given by $1 - e^{-(\sigma^{\pm}/\lambda)^k}$. The plastic strain increment $\Delta\varepsilon = \varepsilon^{\text{pl}}_{ij,\ell+1} - \varepsilon^{\text{pl}}_{ij,\ell}$ between two neighbor elastic branches $\ell$ and $\ell+1$ is also a random variable, *cf.* Fig. 2.3. We choose it to be correlated to the two plastic thresholds associated with the transition $\ell \to \ell+1$, i.e. $\sigma^{+}_{ij,\ell}$ in the forward direction and $\sigma^{-}_{ij,\ell+1}$ in the backward direction. More specifically, we choose $\Delta\varepsilon$ from a uniform distribution in $[0, \Delta\varepsilon_{max}]$ with $\Delta\varepsilon_{max} = \eta(\sigma^{+}_{ij,\ell} + \sigma^{-}_{ij,\ell+1})/(2\mu)$, where $\eta$ is a tunable parameter. Note that the parameter $\eta$ thus controls the strength of the elastic interaction [22, 120]: the larger $\eta$, the larger the short-range stress kicks that trigger the avalanche, but also the larger the amplitude of the mechanical noise arising from the small positive and negative contributions of the long-range stress interaction. We have set $\eta = 1$ in our simulations.

### Nature of disorder

In the following we will consider two different cases:

(i) An annealed disorder where after a plastic slip new values of the thresholds $\sigma^{+}_{ij}$, $\sigma^{-}_{ij}$ are computed in the absence of any memory;

(ii) A quenched disorder, as a result of which the stress landscape of any given cell remains fixed so that the very same elastic branches are revisited in the course of a back and forth motion.

The landscape with quenched disorder is implemented through the use of a counter-based random number generator (CRNG) [109] so that the value of a threshold at the local elastic branch $\ell$ only depends on the index $\ell$ of that branch and on a previously defined key $\kappa$. In this way, the access to, say, $\sigma^{+}_{\ell} = f_{\kappa}(\ell)$ requires just a simple call to the generator without the need of storing a full sequence of random numbers.

In the following we will use an annealed disorder throughout the glass preparation step and a quenched disorder throughout the quasi-static shear driving steps. More specifically, we first “fabricate” our glasses using a two-step process, which mimics a thermalization step at high $T$ and a subsequent aging step at vanishing temperature. We control the degree of aging of our glasses in this manner. Details regarding the glass preparation protocol is discussed in Chapter 3. At the end of this preparation protocol the different fields (thresholds in the forward/backward directions $\sigma_{ij}^{\pm}$ and internal stress $\sigma_{ij}$) are stored; the plastic strain field is reinitialized at zero and this initial configuration is inserted as the slice of index $\ell = 0$ of a stack of quenched disorder thresholds at each cell $(i, j)$. This quenched configuration is then used to perform mechanical loading.

### Driving

Two kinds of mechanical loading are considered in this study: monotonous shear loading and cyclic loading. In both cases, the driving is strain controlled and changed quasi-statically. The elementary steps consist in:

(i) identifying the first site[1] $(i^*, j^*)$ which becomes unstable in the shear loading direction, i.e. the *extremal site*;

(ii) incrementing the external strain $\varepsilon$ up to the point where the extremal site $(i^*, j^*)$ becomes unstable;

(iii) incrementing the plastic strain of $(i^*, j^*)$ by $\Delta\varepsilon$ to trigger the transition $\ell \to \ell \pm 1$ to the next elastic branch by the instability (*plastification*);

(iv) updating the internal stresses of all sites;

(v) identifying any site that has in turn become unstable due to the internal stress update, plastifying these sites as well, updating the internal stress *etc.* until the end of the *avalanche*, i.e. until all sites have become stable again;

(vi) repeat steps (i)–(v) as needed.

### Avalanches

The precise treatment of step (v), i.e. the avalanche, deserves more detail. Once a list of unstable sites has been identified, the question remains about the order in which these sites will be updated. Indeed, since the elastic interaction can induce both positive and negative stress kicks, an unstable site can be healed and get stable again after another one has been plastified and the resulting internal stresses at the other sites have been updated, steps (iii) and (iv). Hence the order of the updates matters. The effect of the ordering of updates on the dynamical properties has been recently discussed by Ferrero and Jagla [41]. Some of us opted for a synchronous update [126]: all unstable sites are plastified simultaneously in

---

[1] We will henceforth use the terms cell and site interchangeably

parallel; the internal stress is updated afterwards; after this first sweep, a new configuration is reached, a stability test is performed, if all sites are stable, the avalanche is over, otherwise a new list of unstable sites is identified and the process is iterated until a stable configuration is reached. Here we make a different choice and perform a sequential update: the most unstable site, i.e. the extremal site, is updated first (plastic slip followed by an update of the associated elastic stress field) and we repeat this procedure until all sites become stable again. This choice of updating protocol happens to be very close to the extremal driving proposed in Ref. [9]

## 2.4 Summary

In this chapter, we started by explaining various building blocks of EPM and common variants employed in studies on plasticity in driven amorphous solids. We then proceeded to briefly discuss the history of EPMs so that the one can appreciate these advances while moving on to the later chapters of the thesis. Finally, we discussed the novelty of our model built to study the history-dependence of such solids to shear but also aimed at capturing limit cycles for probes on yielding and memory under cyclic loading in amorphous solids.

# Chapter 3

# Cyclic driving and the irreversibility transition

In this chapter, we will first introduce a glass preparation protocol to tune the initial degree of annealing of the glass samples at the mesoscale level. We will then test our preparation protocol against uniform shear tests. Using the samples from our glass preparation protocol, we will then study the response of cyclically driven amorphous system at different degrees of annealing and system sizes to reveal the effect on the nature of the irreversibility transition.

## 3.1 Preparation of initial states

The structure and the mechanical behavior of glasses depend on their thermo-mechanical history. In order to account for this preparation dependence in mesoscopic elastoplastic models, one usually specifies a particular distribution of local thresholds and/or internal stress in the initial configuration [107, 128]. In contrast to atomistic simulations these distributions do not derive from a well-defined quench protocol but must be introduced by hand. Here we propose two simplistic protocols of preparation allowing us to mimic (i) an instant quench from a high-temperature liquid, and (ii) an aging process at vanishing temperature. Although they are un-realistic caricatures of actual glass preparations, the combination of these two protocols allows us to continuously tune the system from a very disordered fresh soft glass to a very aged hard glass in a (statistically) reproducible way. Since we have observed that the use of the quenched local landscape during the aging protocol in our elastoplastic model lead to responses that become cyclic and hence aging the glass sample becomes difficult, we will use an annealed disorder in our glass preparation protocols. We note at this point that despite the absence of an explicit energy landscape in our model, which would allow us to equilibrate the system at a finite temperature and to perform a quench to zero temperature [24], it is possible to implement the two limit-cases of glass preparation as we discuss next.

### 3.1.1 Instant quench of a high temperature liquid

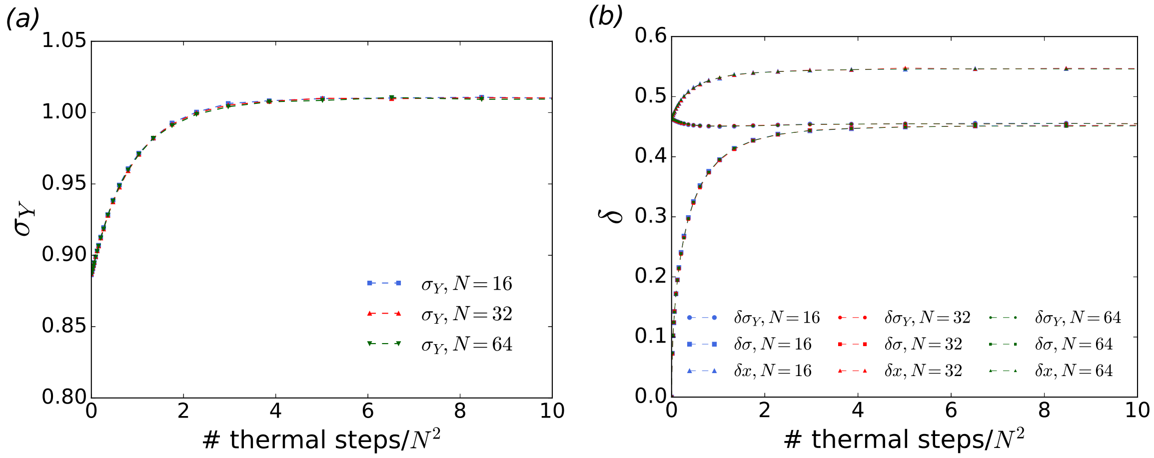

Fig. 3.1 Glass preparation - mimicking instant quench from high T: (a) evolution of the mean stress-threshold $\overline{\sigma^+}$ with the number of (random) thermalization steps per site and for system sizes $N = 16, 32$, and 64. The inset shows the same (b) Evolution for the standard deviations of the stress thresholds $\delta\sigma^+$, internal stresses $\delta\sigma$, and local plastic strength $\delta x^+$ with the number of thermalization steps per site for system sizes $N = 16, 32$, and 64.

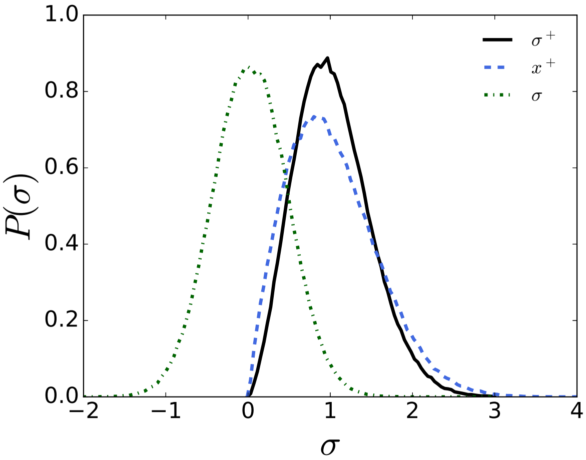

Fig. 3.2 Glass preparation - mimicking instant quench from high T: Stationary distributions of the fields $\sigma$, $\sigma^+$ and $x^+$ for $N = 64$.

At high temperature the local energy barriers associated with the stress thresholds are very low with respect to the available thermal energy so that in the $T \to \infty$ limit, all plastic rearrangements are equally probable. We then define a *thermal* step by selecting a site uniformly in space at random and choosing one of the two directions with probability $1/2$. The chosen site thus experiences a plastic slip and jumps onto a new elastic branch, which is characterized by two new plastic thresholds. Next, the stress field is updated to account for the stress redistribution. The stress redistribution can make some other sites mechanically unstable and thereby induce an avalanche. Updates are then performed until the avalanche stops and the system is stable again. The system is subjected in this manner to a sequence of thermal steps until it reaches a stationary state. In Fig. 3.1(a) we show for different system sizes $N$ how the mean stress-threshold $\overline{\sigma^+}$ of our samples evolves with the number of thermal steps. We see that when plotted against the average number of thermal steps per site, the curves for the different sizes collapse and $\overline{\sigma^+}$ reaches a stationary value rather quickly, after about 4-5 thermal events per site. Fig. 3.1(b) shows at different system sizes the corresponding evolution of the standard deviations $\delta\sigma^+, \delta\sigma$, and $\delta x^+$, of the stress threshold, the internal stress, and the plastic strength, respectively. When plotted against the average number of thermal steps per site, we find again little size dependence. In Fig. 3.2 we show the stationary distributions of the stress-thresholds, internal stress and local plastic strengths for our $N = 64$ sample.

### 3.1.2 Aging at vanishing temperature

We now turn to the other limit, namely aging at very low temperature, $T \to 0$. In the framework of activated behavior, the activity at low temperature is restricted to overcoming the lowest barriers. Moreover, in the limit of vanishing temperature, the lowest barrier becomes dominant. We define an extremal aging step as follows: recall that for each site $(i, j)$ its plastic strength in the positive and negative directions are given as $x^+_{ij} = \sigma^+_{ij} - \sigma_{ij}$ and $x^-_{ij} = \sigma_{ij} + \sigma^-_{ij}$, respectively. We identify the site and direction with the lowest plastic strength and let it experience a local slip so that stresses are redistributed, and new stress thresholds are assigned to the yielded site. As in the case of the "thermal" procedure with randomly selected sites, a stability check is performed after each slip. If one or more sites get unstable, they are updated in turn and with the most unstable sites updated first, as explained before. The procedure is iterated until the avalanche triggered by the initial extremal step terminates. Then, the next site and direction of the lowest plastic strength is identified and allowed to slip.

The present "aging" procedure is thus similar to the "thermal" procedure, differing only in the choice of the initial site to be slipped: in the case of "aging" an extremal site is selected for slip, i.e. the cell and direction with least plastic strength, while in the thermal case the selection of site and direction is random. This difference drastically alters the dynamics, since it induces a systematic statistical bias. When a site yields, it acquires a new pair of thresholds. The latter are drawn from a prescribed distribution. However, in the framework of the aging procedure, this takes place at an extremal site, which is characterized by a very low plastic strength (either in the positive or in the negative direction). We thus get a typical exhaustion phenomenon: low thresholds get replaced by "normal" ones. This systematic bias induces a drift in the threshold distributions and thus a systematic hardening.

Starting from an initial state corresponding to the inherent state obtained from a "high temperature liquid", as described in the previous section, we thus "age" the system by slipping a number of least stable sites. As shown in Fig. 3.3(a), we observe a logarithmic growth of the mean thresholds $\overline{\sigma^+}$ with the number of aging steps. Again, the dependence of this evolution on system size becomes negligible

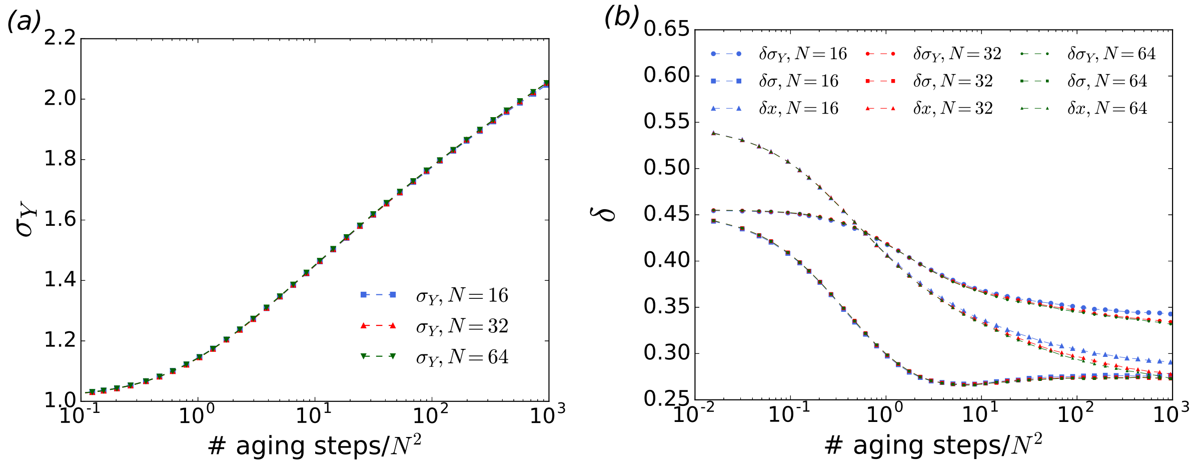

Fig. 3.3 Glass preparation - low temperature aging: (a) evolution of the mean stress-threshold $\overline{\sigma^+}$ with the number of aging steps per site and for system sizes $N = 16, 32$, and 64. (b) Evolution of the standard deviation of local stress $\delta\sigma$, thresholds $\delta\sigma^{\pm}$ and plastic strength $\delta x$ with the number of aging steps per site for system sizes $N = 16, 32$, and 64.

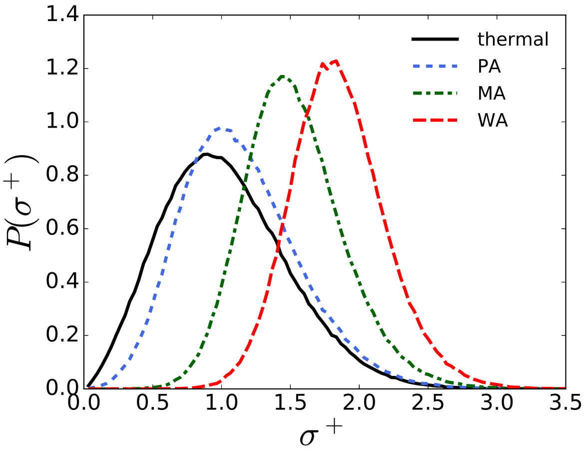

Fig. 3.4 Glass preparation - low temperature aging: Distributions of the stress-thresholds for an $N = 64$ sample, that has not been aged at all (thermal), or aged with an average number of 0.8 (PA), 15 (MA), and 150 (WA) aging steps per site, corresponding to a poorly-, moderately- and well-aged glasses, respectively.

when we consider the average number of aging steps per site, instead of the total number of steps. We find that after about $10^3$ aging steps per site, the mean threshold doubles in value.

Figure 3.3(b) shows, at different system sizes, the evolution of the standard deviation of the stress-threshold, internal stress and plastic strength. When plotted against the average number of thermal steps per site, we find again little size dependence. The standard deviation of thresholds shows a slow decrease (about 20% over $10^3$ aging steps per site). Together with the doubling of the mean thresholds over the same range of $10^3$ steps, this corresponds to a significant narrowing of the threshold distributions upon aging.

Interestingly, after a fast decrease in the early stage of the aging protocol (less than one aging step per site) the standard deviation of internal stress remains almost constant upon aging. In recent studies on the dependence of plastic behavior of amorphous solids on glass preparation [86, 107], the width of the stress fluctuation distribution has been used as a proxy for the level of stability of the amorphous solids while keeping constant (actually uniform) the value of the plastic threshold. We get here a different situation: an increase of the mean threshold and stability of the stress fluctuations upon aging. A way to reconcile these contrasting observations is to consider the fluctuations of the local plastic strength $x^{\pm} = \sigma^{\pm} \mp \sigma$ and to note that in the case of uniform thresholds the standard deviation of plastic strength equals that of internal stress $\delta x^{\pm} = \delta\sigma$. Upon aging, we indeed observe a continuous decrease of $\delta x^{\pm}$ which gets halved after about $10^3$ aging steps per site.

In Fig. 3.4 we display distributions of the stress thresholds $\sigma^+$ for our $N = 64$ samples, which were either not aged at all (thermal), or aged at $0.8, 15$, and 150 aging steps per site, for $N = 64$. These aging levels have been indicated by the appropriately colored circles on the graph showing the evolution of mean stress-thresholds with aging in panel (a). Henceforth we will refer to these levels of aging as poorly-aged (PA), moderately-aged (MA), and well-aged (WA).

The effect of our aging procedure is dramatic: it opens a growing gap in the distribution of stress-thresholds $\sigma^+$. In spirit, we recover here a phenomenology which is close to that of ultrastable glasses obtained via swap Monte-Carlo methods [15]. The opening of a gap will induce a perfect elastic behavior over a finite range of strains which contrasts with the quasi-elastic behavior (short elastic branches punctuated by plastic events) typically observed in less equilibrated glasses.

## 3.2 Annealed versus Quenched disorder for shear driving protocols

In the case of a monotonic loading, every time a cell experiences a plastic deformation, its threshold is renewed. Independently of the particular method chosen to draw random thresholds, the quenched character of the disorder is automatically obtained since a unique value of the threshold $\sigma^{\pm}_{ij,\ell}$ is assigned to each triplet $(i,j,\varepsilon^{pl}_{ij})$. The possibility of back and forth motions requires more care in the definition of the threshold disorder. When performing cyclic shear tests, we use a quenched disorder. In practice, we resort to a counter-based random number generator (see. Ref. [109] for a pedagogical introduction) to assign efficiently a unique pair of random thresholds to each triplet without having to store the full sequence in memory. *Bidirectionality* – Since cyclic loading (in addition to a simple monotonic loading) is studied in this thesis, two local thresholds are defined instead of only one for each cell: one threshold $\sigma^+_{ij}$ in the forward direction and another one $\sigma^-_{ij}$ in the backward direction. To summarise, all the shear driving protocols in our mesoscale simulations always use the same quenched local landscape which was first introduced towards the end of the Chapter 2.

## 3.3 Monotonic Loading: Dependence on thermal history

Depending on glass preparation, stress-strain curves show either a monotonic behavior up to a plateau or exhibit a *stress peak* followed by a *softening branch* that slowly approaches the *stress plateau* at a *steady-state stress* $\Sigma_{ss}$. The existence of a stress peak is usually associated with shear-banding behavior.

In the previous section, we proposed a glass preparation protocol for our mesoscopic model which mimics aging at vanishing temperature. While tuning an aging duration is very different from tuning a quench rate from the liquid state, both methods allow us to transit continuously from a soft/poorly equilibrated glass to a hard/well equilibrated glass. Our protocol actually allows us to obtain in this way very different glassy states. In Fig. 3.5, we show stress-strain curves corresponding to a poorly-aged, a medium-aged, and well-aged glass, aged at an average of $0.8, 15$, 150 number of steps per site. The system size is $N = 32$ and the curves were obtained by averaging over 500 realizations. While the poorly-aged glass does not exhibit a stress peak, such a peak emerges and becomes more pronounced as the samples are aged more. Thus by tuning the duration of aging we are able to transit from a poorly-aged to a well-aged glass. We checked that all curves do converge to the same stress plateau for large enough shear strains. More details on the size dependence of these stress-strain curves are discussed later in the text.

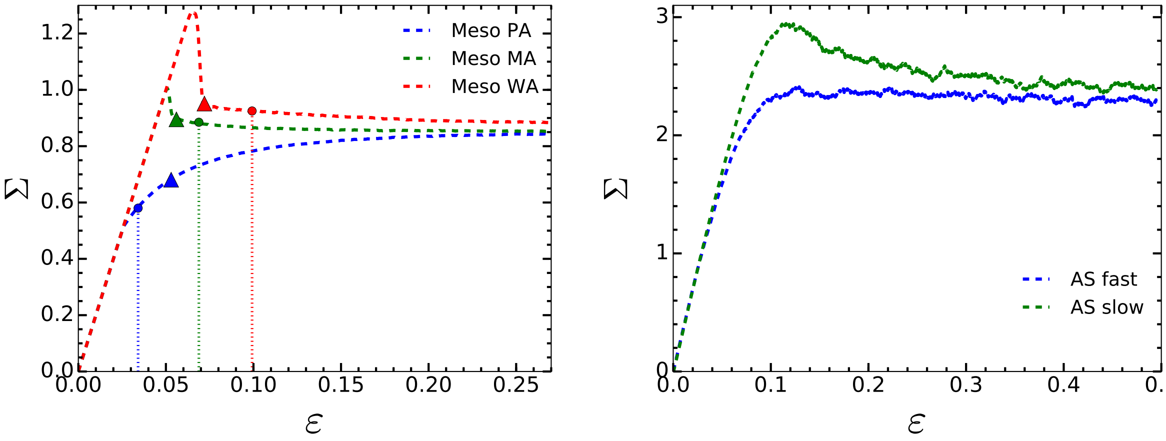

Fig. 3.5 Stress-strain curves upon monotonic loading: (Left) Stress-strain curves obtained for a mesoscopic glasses of size $N = 32$, aged at an average number of 0.8 (poorly-aged PA), 15 (moderately-aged MA) and 150 (well-aged WA) aging steps per site. The moderately- and well-aged glasses show a stress peak followed by a softening branch which crosses over into a stress plateau. The triangles mark the strain amplitudes where the probability to find cyclic response under symmetric oscillatory shear is still larger than 2% (refer to Section 3.4 for details). The dotted vertical lines terminating with small circles mark the range of strains sampled by the transition graphs discussed in Chapter 5. (Right) The corresponding curves obtained from simulations of 2d atomistic glasses that were quenched from a high temperature liquid state at a fast and slow rate. All data from atomistic simulations used in this thesis were provided by Ido Regev.

*Comparison with atomistic simulations* – Atomistic simulations were performed on a two-dimensional binary system with $N = 1024$ particles of two sizes, where half the particles are 1.4 times larger than the other half. We used a two-body radially-symmetric interaction introduced in Ref. [68] and used in Ref. [103], employing the same units of temperature and time discussed there. The initial sample is prepared by first simulating the system at a high temperature in a liquid state, and then quenching the liquid to zero temperature. We used two different preparation protocols to obtain soft and hard glasses. To obtain a soft glass, starting from $T = 1$ we equilibrated the system for $t = 20$ simulation time units and then reduced the temperature to $T = 0.1$ and equilibrated for another $t = 50$. To obtain a hard glass, starting from $T = 1$ we cooled the system to $T = 0.1$ in steps of $\Delta T = 0.025$, where at each step the system was equilibrated for $t = 10$. Once an initial solid sample was prepared, it was sheared quasistastically using a standard AQS protocol: at each strain step, the system is sheared using the Lees-Edwards boundary conditions [65] such that the total strain increases by $10^{-4}$. Immediately after strain is applied, the energy is minimized using the FIRE minimization algorithm [19]. In Fig. 3.5 (b), we show for reference two stress-strain curves obtained by atomistic simulations under athermal quasi-static shear for a slow and fast quench, respectively. The slow quench curve shows a distinct stress peak while apart from fluctuations, the fast quench curve is almost monotonic. Due to computational time limitations, it is difficult to obtain strongly contrasting quenches and consequently stress-strain curves when using molecular dynamics for the glass preparation. The recently developed swap Monte-Carlo methods give access to a wider range of glass preparation although they are more restrictive with respect to the nature of the model glasses [15].

Let us emphasize that it has not been attempted here to adjust the parameters of the elasto-plastic model to quantitatively reproduce the stress-strain curve obtained by atomistic simulations. Rather, our goal is to compare generic features, such as the brittle to ductile transition under monotonic loading, and how the behavior upon cyclic loading depends on the soft/hard nature of a glass. Recent analyses of coarse-graining atomistic simulation to be used to feed mesoscopic elasto-plastic models with realistic parameters can be found in Ref. [40].

*Effect of annealing and system size* – Fig. 3.6 shows the dependence of stress under monotonic strain loading on system size and aging. Different colors correspond to different system sizes, as indicated in the legend, while the line shapes correspond to the different degrees of aging. The curves have been obtained at various extent of aging and for systems of size $N = 16(4000),\ 32(1600),\ 64(750)$, where the numbers in parenthesis indicate the number of realizations used to obtain our results. While the poorly-aged samples (PA with 0.8 aging steps per site) show no discernible size-dependence, with increasing amount of aging a rather weak system size dependence emerges, particularly near the stress peak, as shown in the inset.

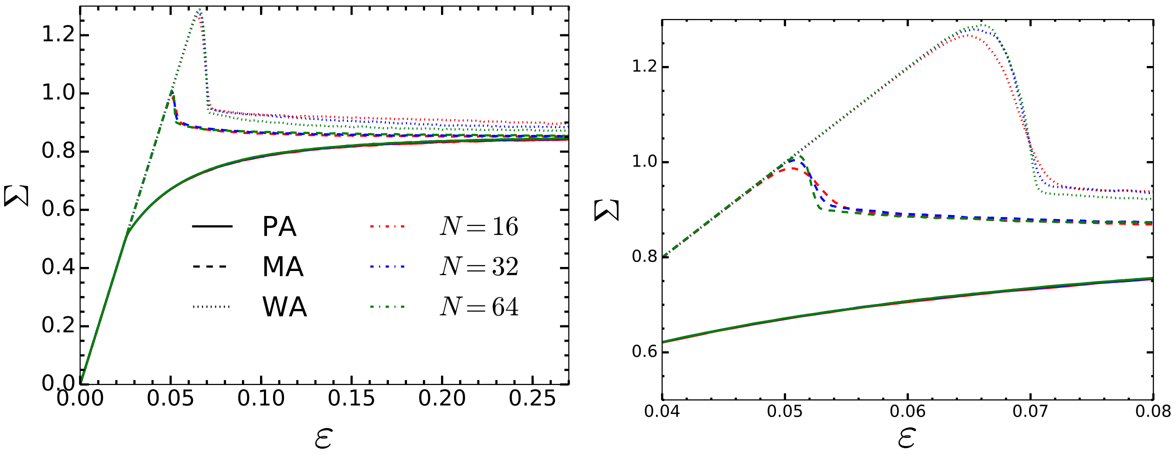

Fig. 3.6 (Left) Stress-strain curves upon monotonic loading for various system sizes and thermal histories. (Right) A blow-up of the region near the stress peak. The ultra-aged (UA) glass is not shown to improve visibility.

## 3.4 Amorphous solids under cyclic shear: An elastoplastic approach

### 3.4.1 Introduction

GI Taylor famously demonstrated the time reversibility of simple shear flows at low Reynolds number [122]. He placed a drop of dye in a viscous fluid contained between two concentric cylinders (also known as circular Couette flow) and rotated the inner cylinder many times. The drop disappears but interestingly is almost perfectly reconstructed when the rotation is reversed. Inspired by this experiment, Pine et. al. [96] used the same Couette flow configuration but also added colloidal particles in the viscous fluid. They then used this setup to impose a slow periodic shear on the dilute suspension of colloidal particles as a prototype to study the transition from reversible to irreversible motion in many-body systems. The authors observed that there is a critical shear amplitude below which the steady state behaviour displays reversible motion such that the stroboscopic particle positions remain unchanged. Above this shear amplitude, particles in the steady state respond irreversibly and show diffusion such that their mean squared displacement increases linearly with time. Corte et. al. took this study a step further with random initial states, using simulations and experiments, to determine the time required to settle in reversible or irreversible steady state as a function of strain amplitude. They observed a power law singularity at a critical strain amplitude that separated reversible from the irreversible response in steady state with exponents consistent with that belonging to the Directed Percolation (DP) university class [31].

The above studies were focused on dilute systems which, like systems with short range interactions, were imagined to find reversible steady states rather easily [? ] as particle contacts are infrequent. A very non trivial question would be extending this problem to the strongly interacting case. Amorphous solids thus become a perfect candidate for probing this question as particle contacts are abundant and long range strain fields are present. In fact many studies have focused on studying the response of periodically sheared amorphous solids [42–44, 52, 54, 58, 60, 80, 103, 104]. It is natural to expect that the reversible motion in solids would occur at small strain amplitudes such that the response is completely elastic.

However, periodic shearing of amorphous solids display reversible behaviour at strains for which uniform shear would display significant plasticity. Plasticity is thought to be an irreversible process but the emergence of a reversible phase well within the plastic regime thus seems to suggest otherwise.

As an example demonstrating the reversible phase, we show in Figure 3.7 from reference [104], the particle trajectories of athermal quasistatic periodically sheared amorphous solid in 2-dimensions. The reversible motion is evident in the fact that particles change their (mechanical) equilibrium positions but repeat the same trajectories such that, when viewed stroboscopically, their positions remain unchanged. Such reversible states have been termed as limit cycles. A limit cycle has an associated period which is the number of cycles required for the system to return to its initial configuration. In the figure, a period two limit cycle is shown such that the particles revisit the same position every two cycles of driving.

These limit cycles have become a valuable tool to probe the yielding transition in cyclically sheared amorphous solids. Poorly annealed glasses subject to cyclic shear at small strain amplitudes settle in limit cycles after short transients. As the strain amplitude increases the transient time increases. At yielding, the transient time to limit cycles diverges. Atomistic simulations and experiments show that there is a power law divergence in the transient time to limit cycles as a function of strain amplitude close to yielding. The associated exponent was measured to be 2.66, quite different from the universality class of dilute systems (the same exponent was measured to be 1.33) where collective effects are absent.

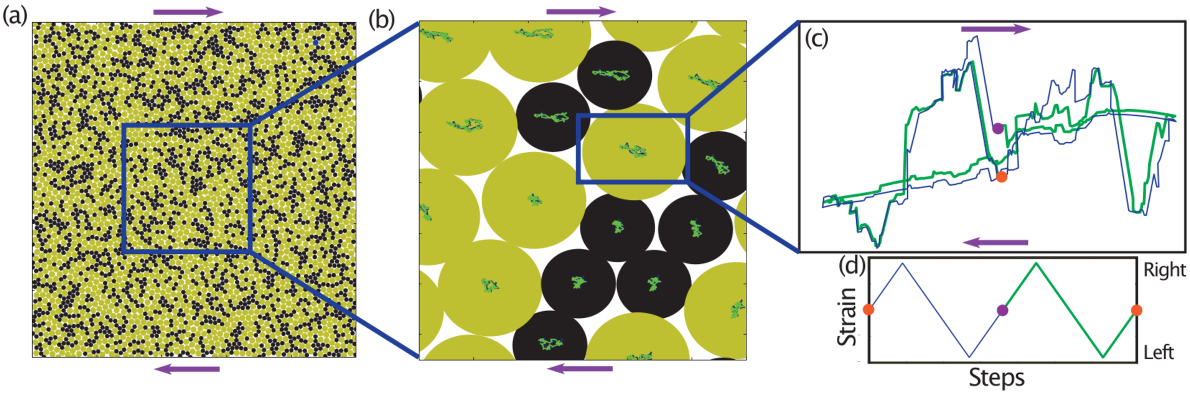

Fig. 3.7 Particle trajectories in an amorphous solid following a multi-periodic limit-cycle. (a) A system of 4096 particles subject to periodic shear. (b) A blow-up showing individual particles and the trajectories performed by their centers marked in blue and green, where blue represents the first cycle and green represents the second cycle. (c) A blow-up showing the trajectory of a single particle. During the first cycle the particle performs the blue trajectory, followed by the green trajectory during the second cycle. (d) The strain as a function of simulation steps (quasistatic equivalent of time) in the cycle. Figure taken from ref. Regev et. al. [104]

In parallel, many studies have focused on understanding the nature of yielding in sheared amorphous solids using uniform shear protocol. Poorly annealed amorphous solids yield in a smooth ductile manner while well-annealed samples yield with a sharp stress drop with appearance of a thin liquid shear band. While studies tend to distinguish between these two types of yielding a debate is still open: poorly annealed samples can also show stress overshoot. Finite size effects apart, understanding yielding through transients, as is the case in uniform shear protocol, may not suffice to settle the discussion[73]. Since cyclic shear protocols offer the possibility of studying the yielding transition using stationary states, they become an important counterpart in assisting such studies.

In the previous chapter we showed that our model recovers the effect of preparation on the plastic behaviour upon monotonic loading; in particular the transition between brittle and ductile responses as discussed above. The main aim of this chapter is to study the response of cyclically sheared amorphous solids using the our elastoplastic model. We will uncover the effects of system size and degree of annealing of the glass sample to understand the nature of yielding in cyclically sheared amorphous solids. More precisely, we consider the irreversibility transition, and in particular the response to cyclic shear of our poorly-aged (PA) and moderately-aged (MA) mesoscopic glasses whose preparation was described in section 3.1. The well-aged (WA) mesoscopic glasses yield a response to cyclic shear that is qualitatively similar to that of the (MA) glasses and will therefore not be considered in this section.

### 3.4.2 Irreversibility transition

When subjected to cyclic shear loading, amorphous solids tend to either evolve into periodic response or reach a diffusive regime, depending on the value of the amplitude $\epsilon_{\mathrm{amp}}$ of the loading cycles. This transition presents typical features of a critical transition. In particular, power-law divergence of the number $\tau$ of loading cycles to reach the periodic response below the transition, as well as the power law dependence of the diffusivity above the transition have been observed both for atomistic and mesoscopic models [16, 42, 66, 90, 98, 103, 104, 129]. The features of the irreversibility transition depend on glass preparation [16–18, 129]. Fig. 3.8 shows the response of an $N = 32$ sample of a poorly-aged mesoscopic glass to cyclic shear at strain amplitude below, panel (a), and above, panel (b), of the irreversibility transition. In the former case a cyclic response was obtained after $\tau = 158$ cycles, while for the latter cyclic response was still absent after $10^4$ driving cycles. The main plots show the evolution of stress and strain over the last 30 cycles, each of which have been color-coded in increasing shades of red, as indicated by the legend in (a). The lower insets show a detail from the main plot, while the upper insets show the evolution of the difference of stresses at the beginning of two consecutive driving cycles. Below the irreversibility transition, panel (a), this stress difference eventually vanishes (after $\tau = 158$ while above the transition in panel (b) it keeps showing finite fluctuations at least until $\tau = 10^4$. In the following, we show results for the size dependence of the irreversibility transition in our PA and MA mesoscopic glasses. Specifically, we consider systems of size $N = 16(7500),\ 32(3000),\ 64(400)$, where the numbers in parenthesis indicate the number of realizations used to obtain our results.

We first focus on the poorly-aged (PA) systems. Figure 3.9 shows the mean *success-rate* $p_{\mathrm{succ}}$, *i.e.* the fraction of PA systems (circles) within our ensemble of realizations that reach a limit cycle when subject to a given number $\tau_{\mathrm{max}}$ of *symmetric* loading cycles at amplitude $\epsilon_{\mathrm{amp}}$: $0 \rightarrow \epsilon_{\mathrm{amp}} \rightarrow 0 \rightarrow -\epsilon_{\mathrm{amp}} \rightarrow 0$. The different colors correspond to the system sizes, as indicated in the legend of the figure. For system sizes $N = 16$, 32, and 64 we used a cut-off of $\tau_{\max} = 10^4$ driving cycles, so that if cyclic response had not been established at that point we considered the run to be unsuccessful. A clear transition can be observed between a low amplitude regime with convergence to a limit cycle and a high amplitude regime with no limit cycle. The transition between these two regimes gets increasingly sharper with system size. A clear size dependence is also observed in the location of the transition which tends to occur at lower strain amplitudes for larger systems. The size effect exhibited by our poorly-aged glasses is all the more striking as it turns out to be completely absent in the response to monotonic loading, and only weakly present in the case of our moderately- and well-aged glasses, (as shown in Fig. 3.6).

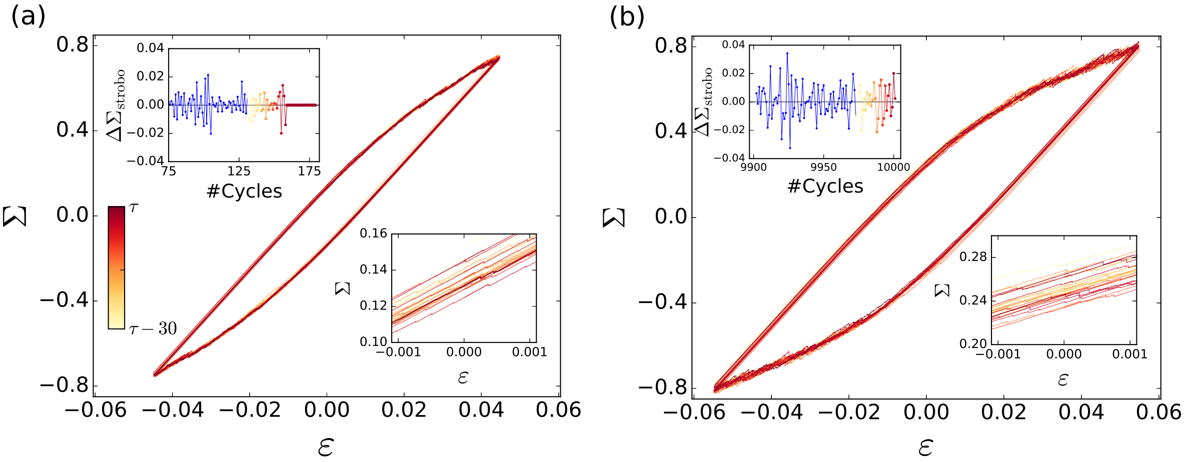

Fig. 3.8 Response of the $N = 32$ poorly-aged glass to cyclic shear at a strain amplitude below, (a) and above (b) the irreversibility transitions by $\Delta\varepsilon = 5 \times 10^{-3}$. The main panels show the evolution of the stress-strain curve over the last 30 cycles with each subsequent cycle colored in a darker shade of red, as indicated in the legend. The insets to the lower right show a detail of this evolution. The insets in the upper left show the stroboscopic stress difference, obtained by taking the difference in stress at the beginning of two consecutive cycles, using the same coloring for the last 30 cycles. In (a) cyclic response is attained after a transient of $\tau = 158$ cycles, while in (b) such a response is still not obtained after $10^4$ cycles.

For each size $N$, we estimate the strain $\epsilon_{\mathrm{irr}}(N)$ at which the irreversibility transition occurs, as the loading amplitude such that 50% of the realizations reach a limit cycle, i.e. $p_{\mathrm{succ}} = 1/2$, as indicated by the pink horizontal line in Fig. 3.9. The inset of Fig. 3.9 shows the size and ageing dependence of $\epsilon_{\mathrm{irr}}(N)$ for $N = 16, 32$, and 64, for the PA, MA and WA glasses. We see that for a given degree of ageing, $\epsilon_{\mathrm{irr}}(N)$ decreases with increasing system size. Moreover, a dependence of $\epsilon_{\mathrm{irr}}$ on aging at fixed system size is clearly visible, in particular for the larger sizes $N = 32$ and 64. At these sizes the MA glasses have slightly larger $\epsilon_{\mathrm{irr}}$ then the PA ones, while the WA glasses have overall larger values of $\epsilon_{\mathrm{irr}}$ for all system sizes considered. The behavior of $\epsilon_{\mathrm{irr}}$ with aging is consistent with atomistic simulations of cyclically sheared amorphous solids which show that the strain marking the onset of the irreversibility transition is largely independent of aging for sufficiently poorly-aged samples, but that it starts to increase as the samples are better aged[16, 129].

We turn next to the response of our moderately-aged (MA) glasses to cyclic shear. The diamond symbols in Figure 3.9 show the fraction $p_{\mathrm{succ}}$ of MA glasses in our ensembles of realizations that reach a limit cycle when subject to cyclic loading of amplitude $\epsilon_{\mathrm{amp}}$. Similarly to the poorly-aged samples, as the system size is increased, the irreversibility transition exhibits an increasingly sharper decline of the success-rate from one to zero. However for a given system size, the rapid fall-off of the success rate in the MA glasses occurs at consistently larger strain values than for the PA glasses, which is in agreement with the behavior of $\epsilon_{\mathrm{irr}}$ discussed above.

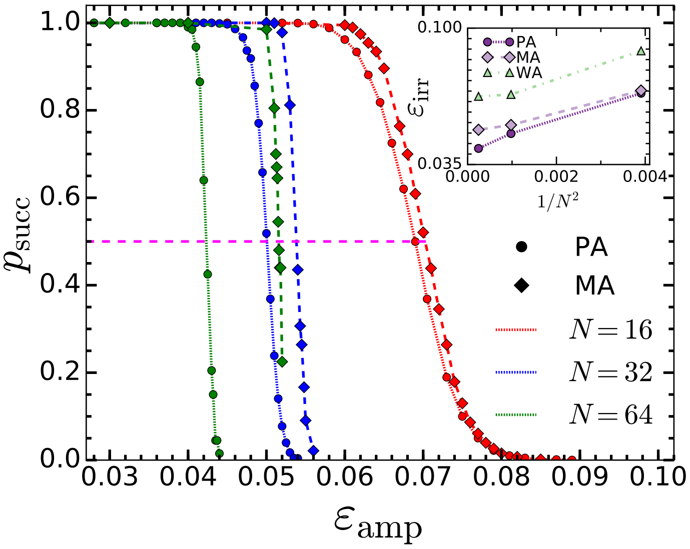

Fig. 3.9 Success rate $p_{\mathrm{succ}}$ of the convergence to a limit cycle under cyclic shearing at amplitude $\epsilon_{\mathrm{amp}}$. Shown are results for ensembles of poorly-aged (circles) and moderately-aged (diamond) glasses with system sizes $N = 16$ (red), 32 (blue), and 64 (green). Intersections with the dashed horizontal line indicate strain amplitudes where the probability of finding a limit-cycle is $1/2$. Inset: The plot of strain amplitudes $\epsilon_{\mathrm{irr}}$ at which $p_{\mathrm{succ}} = 1/2$ against $1/N^2$ for the poorly-, moderately-, and well-aged glasses, PA, MA and WA.

### 3.4.3 Transient regime and limit cycles

Another feature of the irreversibility transition is the divergence of the duration of the transient regime: atomistic simulations show that the number of loading cycles needed to reach the limit cycles diverges as a power-law according to $\tau(\epsilon_{\mathrm{amp}}) \propto |\epsilon_{\mathrm{irr}} - \epsilon_{\mathrm{amp}}|^{-\alpha}$, as shown in Refs. [53, 60, 103, 104].

In Fig. 3.10a, we plot $\tau(\epsilon_{\mathrm{amp}})$ against $|\varepsilon_{\mathrm{irr}}(N) - \epsilon_{\mathrm{amp}}|$ for our poorly-aged glasses and different system sizes $N$. Here $\varepsilon_{\mathrm{irr}}(N)$ is the loading amplitude at which half of the realizations reach limit cycle, as defined previously. Once again, a significant size effect is observed: for a given $|\epsilon_{\mathrm{irr}}(N) - \epsilon_{\mathrm{amp}}|$, the larger the system size, the shorter the transient regime. An indicative power-law behavior of exponent

$\alpha = 2.8$ is plotted as a dashed line. We see that the results obtained for $N = 16, 32$, and 64 are reasonably consistent with this trend over roughly one decade for the larger samples. Note that the value $\alpha = 2.8$ is close to the estimate of $\alpha \approx 2.7$, recently reported in Ref. [60], as well as $\alpha \approx 2.6$, which was obtained using atomistic simulations by Regev et al. [103, 104]. It is also close to the value $\alpha \approx 2.66$ obtained by Corté et al. [31] for a simplified model of interacting particles under flow. The saturation observed for large values of $\tau(\epsilon_{\text{amp}})$ naturally stems from the hard limit associated with the finite number of loading cycles $\tau_{\max} = 10^4$ that we used in our numerical simulations for $N = 16, 32$, and $N = 64$.

In Fig. 3.10b, we also plot the period of the limit cycle $T(\epsilon_{\text{amp}})$ against $|\epsilon_{\text{irr}}(N) - \epsilon_{\text{amp}}|$ for our poorly-aged glasses and different system sizes $N$. As already observed in Ref [60], we see that the limit cycles get more and more complex, with an increasing period when the amplitude $\epsilon_{\text{amp}}$ of the cyclic loading approaches the irreversibility transition $\epsilon_{\text{irr}}$. For illustrative purpose we show that the fast increase of the period is consistent with a power law behavior $T(\epsilon_{\text{amp}}) \propto |\epsilon_{\text{irr}}(N) - \epsilon_{\text{amp}}|^{-\beta}$ with $\beta = 1.5$ plotted as a dashed line in Fig. 3.10b.

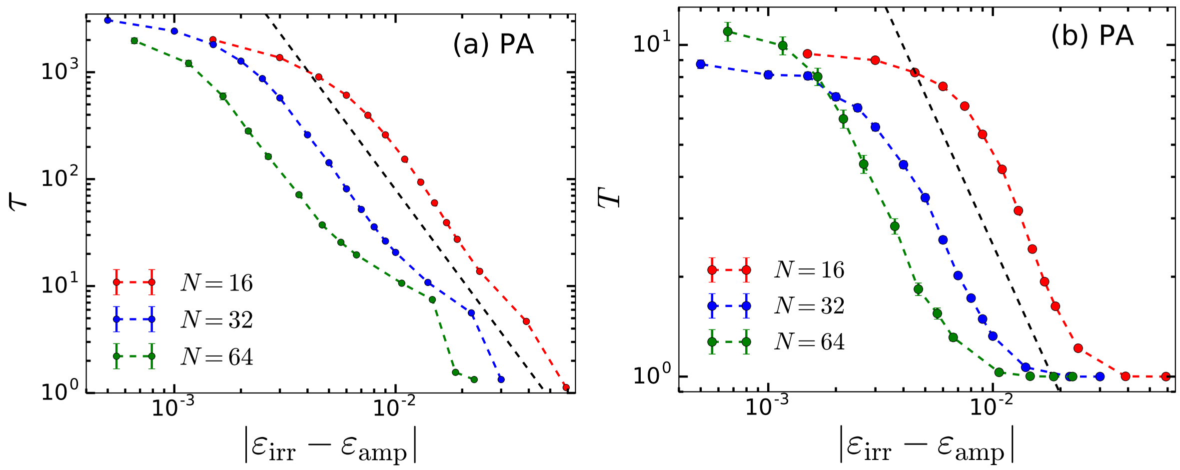

Fig. 3.10 Convergence to limit cycles of poorly-aged (PA) glasses: (a) Duration $\tau$ of transients *vs.* relative cycle amplitude $|\epsilon_{\text{irr}} - \epsilon_{\text{amp}}|$, where $\epsilon_{\text{irr}}$ is the system size dependent strain amplitude where the success-rate $p_{\text{succ}}$ of cyclic response is 1/2, *cf.* Fig. 3.9. The dashed line is a power-law with exponent 2.8 and serves as a guide to the eye. (b) The period $T$ of the cyclic response in units of the number of driving cycles for the poorly-aged samples at different system sizes. The dashed line is a power-law with exponent 1.5 and serves as a guide to the eye.

In Fig. 3.11, we show the same observables $\tau(\epsilon_{\text{amp}})$ and $T(\epsilon_{\text{amp}})$ close to the irreversibility transition, now for the moderately-aged glasses. For small systems sizes ($N = 16, 32$), we again observe a diverging trend in the transient duration and the limit cycles period. It appears actually that the larger the system size, the narrower the range of amplitudes over which this diverging behaviour holds. Another behaviour gradually becomes dominant: for large system sizes, a limit cycle is reached after just a few loading cycles, and the response is mainly elastic. Moreover, as can be seen for the $N = 64$ glass in Figs. 3.9 and 3.11 the transition to irreversibility is rather abrupt and discontinuous. The system either reaches a $T = 1$ cyclic response rather quickly or not. These findings are consistent with results reported in the literature,

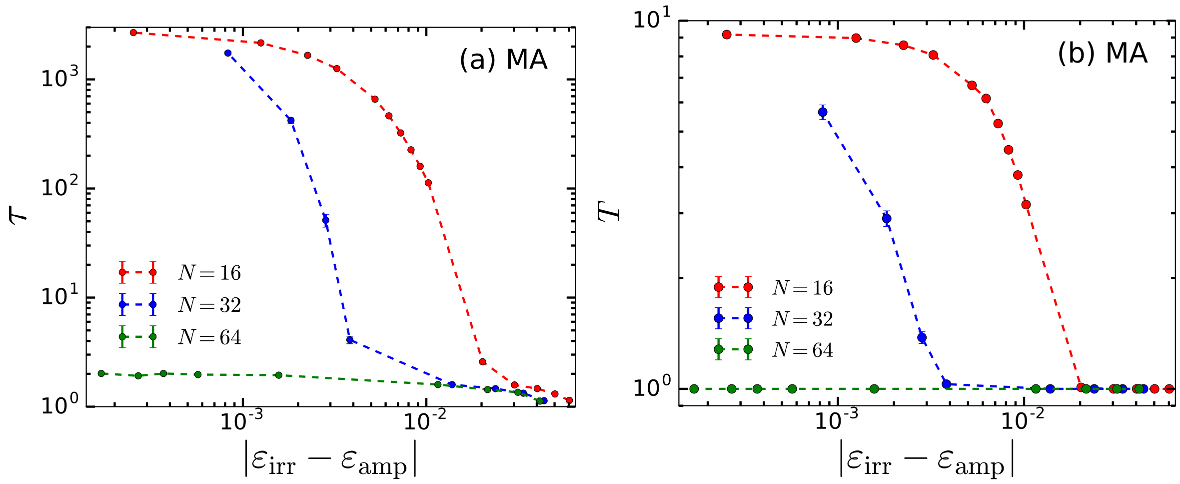

Fig. 3.11 Convergence to limit cycles of moderately-aged (MA) glasses: (a) Duration $\tau$ of transients *vs.* relative cycle amplitude $|\epsilon_{\rm irr} - \epsilon_{\rm amp}|$, where $\epsilon_{\rm irr}$ is the system size dependent strain amplitude where the success-rate $p_{\rm succ}$ of cyclic response is $1/2$, *cf.* Fig. 3.9 (inset). (b) The period $T$ of the cyclic response in units of the number of driving cycles for the moderately-aged samples at different system sizes.

*e.g.* work by Bhaumik[16] *et al.* where the authors consider simulations of a 3d amorphous solid subject to cyclic shear. In their paper's supplement shows the evolution of the transient for a well-aged sample by monitoring the average potential energy per particle. Depending on the shear amplitude, the transient is either very short or a cyclic response is not attained at all.

### 3.4.4 Finite-size effects and the irreversibility transition

As our cyclic shear simulations show, at strain amplitudes close to but below the irreversibility transition, cyclic response may eventually be attained, but after a long transient. In particular, for the better-aged MA and WA samples we find that with increasing system size the transition to irreversibility becomes abrupt, meaning that we either reach cyclic response after a few driving cycles (typically 1 or 2 cycles) or not at all, implying a rather sharp and possibly discontinuous transition from reversibility to irreversibility. Our simulations indicate that this transition becomes smoother when the system size is fixed and the samples are less aged or when we reduce the system size at fixed aging steps per site. Thus, for example, for system sizes $N = 16$ and $N = 32$, the moderately-aged samples are able to attain limit-cycles (*cf.* Fig. 3.11(a)), and even at strain amplitudes that are well beyond the location of the stress peak under uniform shear, which is thought of as marking the onset of yielding. To demonstrate this, we have used red triangles to mark on the monotonic loading curves of Fig. 3.5 (Left) the strain amplitudes beyond which the probability of finding a cycle is less than 2%. For the MA and WA samples they are located beyond the stress peak.

These observations are consistent with findings in a recent work on periodically sheared 3*d* atomistic glass formers [1]. There it was found that small samples that were moderately- or well-aged exhibit cyclic response at amplitudes well beyond the value of the strain at the stress peak. As the size of the samples increases, a sharp irreversibility transition at the stress peak is recovered. We should note however, that in Ref. [1] such behavior was found to be the case only for totally *asymmetric* shear protocols of the form $0 \to \epsilon_{\text{amp}} \to 0 \to \epsilon_{\text{amp}} \cdots$

Summarizing all of these findings: (i) we think that for the better-aged samples, the cycles reached after relatively long transients and at amplitudes beyond the stress-peak, meaning that the cyclic driving must have passed through it at least once, are an artefact of the system's finite size. (ii) Related to this, we also find that as the samples get increasingly better aged, finite-size effects are not necessarily characterized by long transients. A case in point is the response to cyclic shear for the $N = 32$ UA (ultra-aged samples obtained using 4000 aging steps per site in the glass preparation protocol). Here it turns out that a cyclic response after only a few cycles is reached even at strain amplitudes as large as 0.4, which is well beyond the location of the stress peak. A better understanding of such finite size effects, particularly in the ultra-stable glasses is clearly desirable and the subject of future work.

## 3.5 Summary

In this chapter, we proposed a simple and yet physically motivating glass preparation protocol at the mesoscale level. The first part of the protocol generates samples that evolve towards and eventually settle in thermalised states with distributions of all local quantities reaching a stationary distribution independent of the system size. The second part then takes these thermalised states to tune the degree of annealing of the sample. The effect of such an annealing procedure, for example, can be seen as a systematic increase in the mean of the local stress thresholds with an amount depending on the degree of annealing provided. Another aspect reflecting the well annealed nature is seen through the variance of the same quantity which decreases with increasing amount of annealing. The effect of system size again remained negligible. The contrasting nature of the states obtained using the two methods is due to the difference in avalanche deciding step. In the thermalisation part of the protocol, the avalanche deciding plastic event is chosen at random in space (and in direction) which under the assumption that the evolution of plastic activity occurs at high temperatures. While in the aging protocol, the samples are annealed assuming the limit of vanishing temperature in which the avalanche deciding plastic event is controlled by the least unstable site (also in direction) in the system.

To validate our glass preparation protocol, we then performed unidirectional or uniform shear tests on the samples. We observed that samples which are poorly aged, under the effect of external strain, transition from an initially elastic state in a smooth ductile manner into a plastic flowing state. As the degree of annealing is increased, we see that the stress-strain response near the transition develops a stress overshoot followed by a macroscopic stress drop before settling in a plastic flowing state. The size of the macroscopic stress drop close to yielding increased as the degree of annealing of the sample was increased. We checked and found that independent of degree of annealing and system size, the stress-strain response in the plastic flowing state all converged to the same steady-state at large values of strain. While we do not see any system size effects for poorly annealed samples, well annealed samples near yielding do show a weak dependence on system size. The macroscopic stress drop near yielding are observed to drop slightly more sharply for larger system sizes.

Finally, using our elastoplastic model, we studied the response of cyclically sheared amorphous systems at different degrees of annealing and system size to understand the nature of the irreversibility transition. At driving amplitudes below the irreversibility transition, limit cycles are found. These limit cycles disappear for driving amplitude above the irreversibility transition. The transition between the two regimes depends significantly on system size independent of degree of annealing of the sample. However, for better annealed samples the limit cycles are obtained through short transients or not obtainable at all, implying a sharp transition between the two regimes and possibly discontinuous. For poorly-aged glasses, the transient time to limit cycles grows like a power law as the irreversibility transition is approached. The corresponding exponents are in good agreement with atomic scale simulations. Our model also captures multi-periodic limit cycles, whose period increases as the irreversibility transition is approached. The approach to the irreversibility transition is affected significantly by the system size which intrestingly remain absent (or present weakly for well-aged systems) under uniform shear tests.

# Chapter 4

# Memory effects

## 4.1 Introduction

Many disordered systems under periodic driving ranging from non-Brownian dilute suspensions, dense amorphous solids to charge density wave conductors show memory effects [59].

In the non-Brownian dilute suspensions [57, 93] case for example, periodically driving (or training) in strain at a certain amplitude $\gamma_{train}$ below a critical value $\gamma_c$ helps find the system a reversible steady state. Further cyclic driving the steady state leaves the system stroboscopically unchanged in particle positions. When such a steady state is subjected to cycles of increasing amplitude of shear strain $\gamma_{read}$ sweeping past $\gamma_{train}$, stroboscopic measurement of particle displacements for example, shows a dramatic increase from zero when $\gamma_{read} \geq \gamma_{train}$, revealing the memory of training amplitude. In the same studies it was also shown that when the driving amplitude changed from one cycle to the next during the training phase, the system retained memory of multiple amplitudes. However, memory of multiple amplitudes could survive only before the steady state was reached. Earlier to the studies on non-Brownian dilute suspensions, similar memory effects were discovered in charge density wave conductors despite being a completely unrelated system [30].

Memory effects are also observed in experiments and particle scale simulations on amorphous solids [59]. However, some crucial differences exist as compared to the dilute suspensions case.

In dilute suspensions, particle-particle contacts vanish in the steady state and the system cannot permit collective effects. Particle motion trace the same forward and backward trajectory. In the case of amorphous solids however, contacts are abundant and endure shear cycles including during the steady state. The abundance of contacts imply that shear cycles on steady states could be holding a dynamic length scale supporting collective effects [105].

Another crucial difference lies in the fact that multiple memories in amorphous solids are persistent. This means that, unlike dilute suspensions, the steady state can encode multiple memories [43]. However, there is a constraint on the ordering of amplitudes during the training phase. Each applied training amplitude must be smaller than the preceding one, a trait reminiscent of disordered solids obeying return point memory. It should be pointed out that memory in dilute suspensions do not pose any restriction on the order in which the training amplitudes should be applied [59].

In this chapter, we show that our mesoscale elastoplastic model (EPM) for amorphous solids can capture single memories of training and present results that cover the effects of driving past the irreversibility transition. Our model uses Eshelby interactions for stress kicks post local yield events and thus guarantee to break return point memory (RPM). Despite this, we find that an ordering of training amplitude consistent with RPM produces memory of multiple amplitudes of training. Such a result is in agreement with observations in particle scale simulations on amorphous solids where a near perfect RPM behaviour was observed at least till below the yielding strain [78]. We show that the direction of training can also be revealed through suitable read-out measurements on the trained steady state. We show that such a memory of shear direction can be encoded from the first shear cycle onwards and persist even past the irreversibility transition. We present results on the distribution of various local quantities of the EPM as an independent tool to reveal and understand the memory of training. We also demonstrate that our EPM can recover multiple amplitudes of training and proceed to understand the role of prior training using cyclic driving on the possibility of encoding further memories of training amplitude.

## 4.2 Training and readout protocol

In this chapter, we show that our elastoplastic model can capture single and multiple memories of training amplitude. The initial state of the glass sample is generated using thermalisation and aging protocols introduced in Chapter 3. Such an initial state is then subjected to a training protocol that involves shear driving the sample resulting in a trained state. A read-out protocol on the trained state is then performed to probe the memory of training and direction. Below we describe the training and read-out protocols for the single and multiple memory case separately.

### 4.2.1 Single memory

In the single memory case, the training protocol constitutes of shear driving an initial state at constant strain amplitude for a maximum of $10^4$ cycles. A training cycle at a strain amplitude $\gamma_1$ is of the following form in strain: $0 \to \gamma_1 \to -\gamma_1 \to 0$. Such a training cycle is applied one after the other to form a training sequence represented in strain amplitude as: $\gamma_1\gamma_1\gamma_1..$ . Each entry in this sequence represents one training cycle at amplitude $\gamma_1$. The state obtained at the end of training, called a *trained state*, could either belong to a limit cycle or not depending on the amplitude. The training phase continues until the sheared sample finds a state belonging to a limit cycle at which point the training terminates or continues to a maximum of $10^4$ cycles ending in a trained state in case no limit cycles are found. The maximum number of cycles performed to obtain a trained state equals $10^4$ cycles. Unless otherwise stated, results on single memories will always use such a training protocol.

A trained state is then subjected to a read-out protocol to reveal the memory of training. We employ two types of read-out protocol. A parallel read protocol, which has been employed in particle scale simulations and remain inaccessible to experiments. And a sequential read out protocol that can be used in experiments. These are described below and shown schematically in figure4.1:

(a) Parallel read: Identical copies of the trained sample are made. Each copy is then subjected to a single shear cycle with a different strain amplitude at the end of which the state of the system is recorded. The recorded state is compared with the trained state. Strain amplitudes range from 0 to 0.17, sweeping past and well above the training amplitude. For comparison, as noted from Chapter 3, $\gamma_{irr}$ for system sizes $N = 16$ and $N = 32$ are 0.069 and 0.0499, respectively.

(b) Sequential read: The trained sample is subjected to a series of cycles with increasing amplitude. At the end of every cycle the state of the system is recorded and compared to the trained state. Strain amplitudes range from 0 to 0.17, sweeping past and well above the training amplitude. The increase in strain amplitude per cycle is 0.001 and 0.0001 for system sizes $N = 16$ and $N = 32$, respectively. Our results are insensitive to step size per cycle in the strain amplitude.

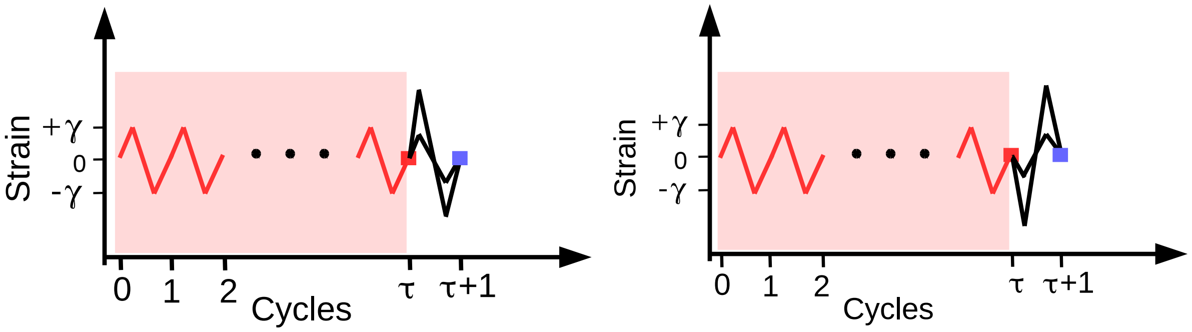

Fig. 4.1 Training and parallel read-out protocol: Training cycles (solid line in red) beginning from the undeformed state at zero strain at fixed amplitude $\gamma_{train}$ lead to a trained state (red square symbol). Read out phase begins with making multiple copies of the same trained state. Each copy is then subjected to a single cycle of strain (solid line in black) at different strain amplitude $\gamma_{read}$ ending in a read state (blue square symbol). Read state in blue symbol is compared to the trained state in red symbol to reveal memory of training. (Left) Read cycle is in phase with the last applied training cycle. Two different read cycles are shown with read amplitude $\gamma_{read}$ below and above the training amplitude $\gamma_{train}$ each leading to a different read state. (Right) Read cycle is out of phase with the last applied training cycle. Two different read cycles are shown with read amplitude $\gamma_{read}$ below and above the training amplitude $\gamma_{train}$ each leading to a different read state.

As mentioned in the Introduction, our EPM can also reveal the direction of training. The initial undeformed state can be trained using a driving sequence of amplitude $\gamma_1$ either like $0 \rightarrow \gamma_1 \rightarrow -\gamma_1 \rightarrow 0$ or $0 \rightarrow -\gamma_1 \rightarrow \gamma_1 \rightarrow 0$. The two separate types of training differ only in direction. One drives the initial state clockwise in the global stress-strain response while the other in the anti-clockwise direction. Results presented in this chapter always use a clockwise training protocol. To reveal the direction of training we consider read-out protocols as defined next.

(a) In-phase read-out protocol: The trained state is subject to a read-cycle in shear of the following form in strain: $0 \rightarrow \gamma_{read} \rightarrow -\gamma_{read} \rightarrow 0$. We note that, since a single training cycle in strain is of the form $0 \rightarrow \gamma_{train} \rightarrow -\gamma_{train} \rightarrow 0$, such a read protocol remains in-phase with the last applied cycle in the training phase.

(b) Out-phase read-out protocol: The trained state is subject to a read-cycle in shear of the following form in strain: $0 \rightarrow -\gamma_{read} \rightarrow \gamma_{read} \rightarrow 0$. Such a read protocol is clearly out of phase in the applied strain with respect to training cycles.

We will see in a later section that a comparison of the response of the trained state to the above two types of read-out protocol reveals the direction of shear imposed on the sample during the training phase.

For our purposes of study in this chapter, a read-out protocol will therefore have four possibilities: A parallel in-phase read-out (Figure 4.1 (Left)), a parallel out-phase readout (Figure 4.1 (Right)), a sequential in-phase readout (Figure 4.2 (Right)), and a sequential out-phase read-out(Figure 4.2 (Left)).

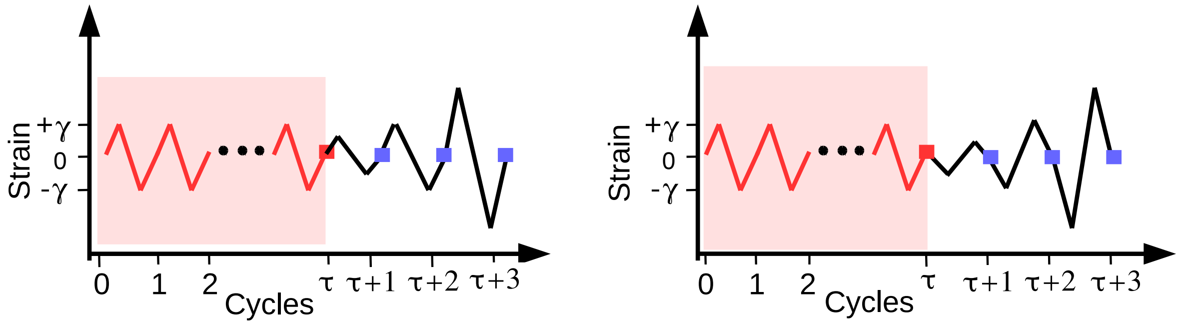

Fig. 4.2 Training and sequential read-out protocol: Training cycles (solid line in red) beginning from the undeformed state at zero strain at fixed amplitude $\gamma_{train}$ lead to a trained state (red square symbol). The read-out phase subjects the trained state to a sequence of read-cycles (solid line in black) with increasing amplitude. States are saved at the end of each cycle (blue square symbol) in the read sequence. Each read state in blue symbol is compared to the trained state in red symbol to reveal memory of training. (Left) Read cycle is in phase with the last applied training cycle. (Right) Read cycle is out of phase with the last applied training cycle.

To reveal the presence or absence of memory of training we use a function which measures how different a read-state (recorded at the end of the read-out phase) is from the trained state. We define the function next. Let $(i, j)$ represent the spatial coordinate of a particular cell in our mesoscopic model. The stroboscopic distance uses a field variable $E(i, j)$, which we call the event field, that measures the net local count of number of plastic events that a cell has suffered since the initial undeformed state as a result of external shear applied to the system. Since our scalar elastoplastic model is built on the assumption that local plastic events are reversible, a plastic event at $(i, j)$ in the forward direction means that $E(i, j)$ should be incremented by 1. If following this, a plastic event in the reverse direction occurs then the current value of $E(i, j)$ should be decreased by 1. $\Delta E(i, j)$ for such a cell is then zero. It is thus clear that the value of $E(i, j)$ is always an integer which can be negative, 0 , or positive for a cell $(i, j)$.

The initial undeformed state has an event field $E(i,j) = 0$ for all $(i,j)$ in the system. We use such an event field for the purpose of recovery of memory of training in our model.

Let $E(i,j)_{train}$ and $E(i,j)_{read}$ represent the event field corresponding to the trained state and the recorded state from the read-out phase, respectively. If $\zeta$ is the set of all the cells $(i,j)$ such that $E(i,j)_{train} - E(i,j)_{read} \neq 0$, then the stroboscopic distance is defined as follows:

$$1 - Overlap = \frac{|\zeta|}{N \times N}\,. \tag{4.1}$$

Here, $|\zeta|$ is the cardinality of the set $\zeta$ and system size equals $N \times N$. We will call $1 - Overlap$ as the *stroboscopic distance* for purpose of discussions in this chapter. To summarise, the stroboscopic distance is the fraction of cells of the trained sample whose local event field do not match the reference sample (or the recorded state) obtained during the readout phase. Obvious from the definition, the range of the stroboscopic distance is $[0,1]$. It is zero when the event field of the trained state and the recorded state from the read-out phase are identical. It is equal to 1 if no cell in the trained state matches the recorded state in the read-out phase.

### 4.2.2 Multiple memory

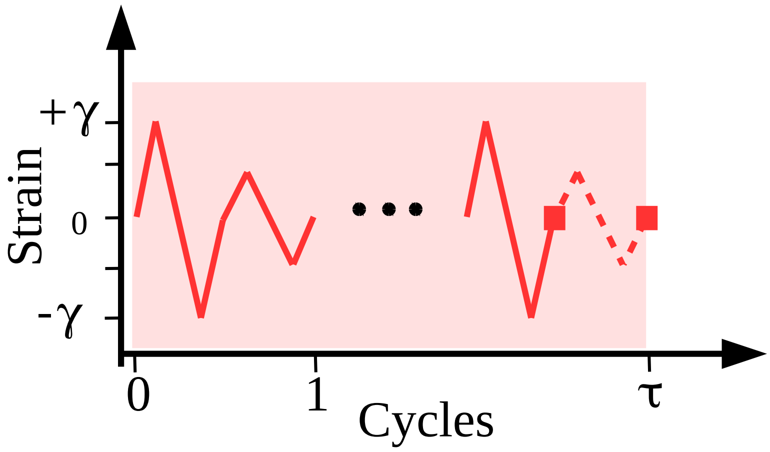

Fig. 4.3 Training protocol for multiple memories: Training cycles (line in red) beginning from the undeformed state at zero strain leading to a trained state (red square symbol). The first two training cycles are of the following form in strain: $0 \rightarrow \gamma_2 \rightarrow -\gamma_2 \rightarrow 0 \rightarrow \gamma_1 \rightarrow -\gamma_1 \rightarrow 0$. Note that the first applied training amplitude on the undeformed state is $\gamma_2$ ($> \gamma_1$). The training sequence in the amplitude representation is of the form: $\gamma_2\gamma_1\gamma_2\gamma_1\gamma_2\gamma_1..$ . The last applied strain amplitude in the training sequence can either be $\gamma_2$ (in solid red) or $\gamma_1$ (in dashed red) affecting the possibility of revealing multiple memories of training, that is, $\gamma_1$ and $\gamma_2$ during the read-out phase.

In the multiple memory case, we use two training amplitudes $\gamma_1$ and $\gamma_2$ for simplicity. A single training cycle at any given amplitude, $\gamma_2$ for example, is of the following form in strain: $0 \rightarrow \gamma_2 \rightarrow -\gamma_2 \rightarrow 0$. Assuming $\gamma_2 > \gamma_1$, the first applied training cycle on the undeformed initial state is always at strain amplitude $\gamma_2$. The training sequence can then be represented using the amplitudes in the following form: $\gamma_2\gamma_1\gamma_2\gamma_1\gamma_2\gamma_1..$ . Each entry in the sequence represents a single training cycle at the corresponding amplitude in the sequence. The first two training cycles on the undeformed state are also shown in Figure 4.3. The trained state could either result in a limit cycle or not depending on the amplitude of $\gamma_2$. As in the training protocol in the single memory case, the training terminates upon finding a limit cycle. The last applied training amplitude ending in a trained state could then either be $\gamma_2$ or $\gamma_1$. If no limit cycle is found the training terminates after $10^4$ cycles and the state obtained will be termed as a trained state. Unless otherwise stated, results on multiple memory will always be presented under the above stated conditions. The training protocol is also summarised using the Figure 4.3.

A trained state is then subjected to a read-out protocol to reveal memory of training amplitudes, that is, $\gamma_1$ and $\gamma_2$. The read-out protocols are exactly the one used in the single memory case. However, we present results from the parallel in-phase read-out protocol only. The same definition of stroboscopic distance is utilised.

## 4.3 Memory of training amplitude

As discussed in the Introduction, experiments [55, 77] and particle scale simulation [2, 43] have revealed that cyclically driven amorphous systems can encode memory of training amplitude. In these studies, a glass sample is driven at fixed amplitude $\gamma_1$ with a driving cycle of the following form: $0 \rightarrow \gamma_1 \rightarrow -\gamma_1 \rightarrow 0$. The driving continues for a certain number of cycles ending in a trained state. Such a trained state is then subjected to a read-out protocol, sequential in case of experiments for example, to reveal the memory of training amplitude. As an example, we use Figure 4.4 from the reference [55] that shows memory of single amplitude of training in experiments. In their experiments, the authors first trained their sample at a strain amplitude $\gamma_{train}$ to reach a steady-state such that stroboscopic difference of particle positions are zero. A sequential read-out is performed on the trained state to reveal memory of training amplitude. The training and read-out protocols are summarised in Figure 4.2 (Left). In Figure 4.4, we see a local minimum in the mean squared displacement of particles when plotted against $\gamma_{read}$. The local minimum occurs at $\gamma_{read} = \gamma_{train}$ reflecting a memory of training amplitude for each of the training amplitude listed in the legend.

Here we capture these results using our EPM. In agreement with these studies, our results show that the memory of training amplitude can be revealed for $\gamma_{train} < \gamma_{irr}$. However, our results also indicate that, for a measurement of memory based on the stroboscopic distance that we have defined, systems could recall the training amplitude even past the irreversibility transition $\gamma_{irr}$. The quality of memory at $\gamma_{read} = \gamma_{train}$ does degrade as the amplitude of training increases past the $\gamma_{irr}$.

### 4.3.1 Mean of the stroboscopic distance

We first discuss Figure 4.5 (Left). Here we recall that we are using a parallel in-phase read-out protocol. We consider four training amplitudes, two above and two below the irreversibility transition $\gamma_{irr}$. At

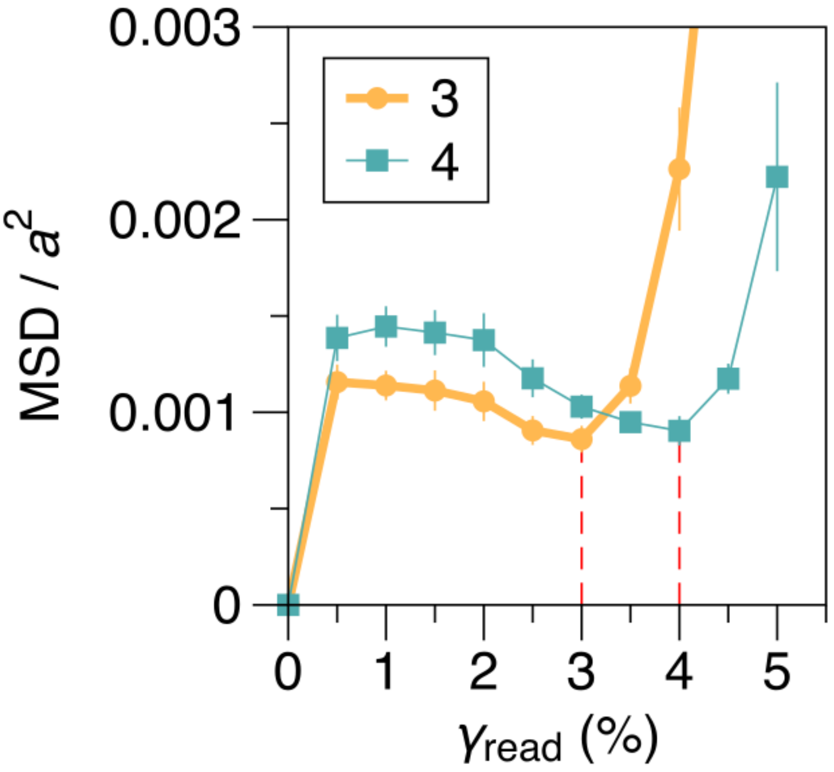

Fig. 4.4 Mean squared displacement over all the particles normalised with respect to typical distances between particle centers versus strain amplitude during read-out. Training amplitude is indicated in the legend. Training and read-out protocols are the same as in Figure 4.2 (Left). Figure adapted from reference [55].

the smallest training amplitude $\gamma_{train} =$ 0.03, we see that the stroboscopic distance drops to zero at $\gamma_{\rm read} = \gamma_{\rm train}$ reflecting a clear memory of training amplitude. At such a training amplitude all the samples find limit cycles and their period equals one. Since the read-out protocol shears trained states for single cycles only, period one samples must contribute to a zero value of the stroboscopic distance. At $\gamma_{train} =$ 0.05, which is still below $\gamma_{irr}$, we see a sharp local minimum at $\gamma_{\rm read} = \gamma_{\rm train}$ but the stroboscopic distance is not zero anymore. At such a training amplitude all the samples find limit cycles. However, the period of limit cycles for some samples are greater than 1. Such samples with multi-period limit cycles then contribute to a non-zero value of the stroboscopic distance at $\gamma_{\rm read} = \gamma_{\rm train}$. Inspite of this, a local minimum in the stroboscopic distance exists, implying that multi-periodicity in the trained states do not eliminate memory of training amplitude. At training amplitude $\gamma_{train} =$ 0.07, which is greater than $\gamma_{irr}$, nearly half of the trained states do not find limit cycles. The value of the overlap at $\gamma_{\rm read} = \gamma_{\rm train}$ is such that nearly 25% of the mesoscopic cells in the read state do not match the trained state and yet we see a clear memory of training amplitude through a local minimum at $\gamma_{\rm read} = \gamma_{\rm train}$. At $\gamma_{train} =$ 0.076, a sharp local maximum at $\gamma_{\rm read} = \gamma_{\rm train}$ does not exist anymore. At this training amplitude, only about 5% of the samples find limit cycles as estimated in our previous works [61].

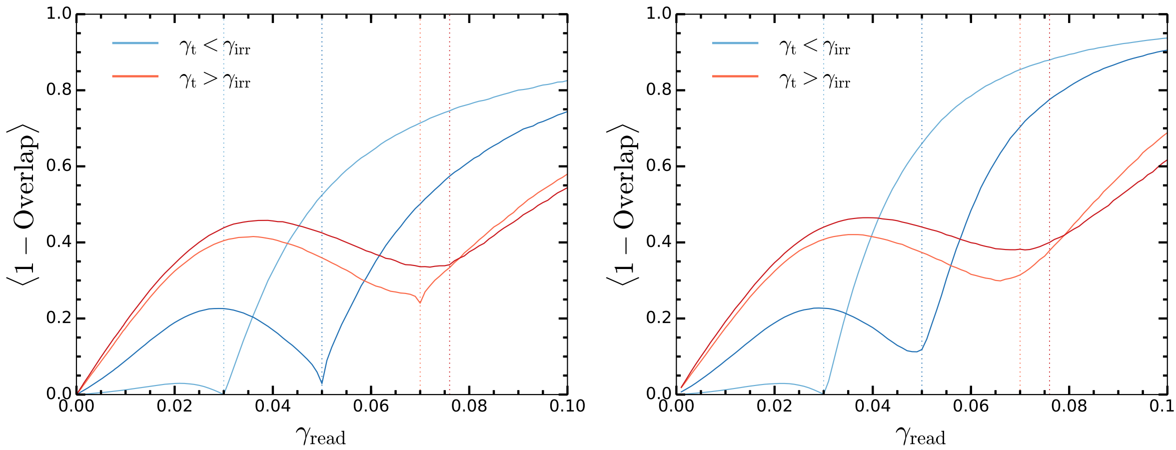

Fig. 4.5 Memory of training amplitude: stroboscopic distance versus $\gamma_{read}$ for (Left) Parallel read-out protocol and (Right) Sequential read-out protocol. Each curve in a given figure corresponds to a different training amplitude. Curves in shades of blue correspond to training amplitudes below the irreversibility transition while those in shades of red are above it. Dotted vertical lines on the $\gamma_{train}$-axis represent, in the same color, the corresponding value of the training amplitude. System size $= 16 \times 16$, poorly aged (PA) samples. Each readout curve has been obtained by averageing over 1000 realizations of the trained state.

Next, we discuss the sequential read protocol in Figure 4.5 (Right). Unlike the parallel read protocol which requires making multiple copies of the trained state, the sequential read-out protocol can be used in experiments [55]. In the figure, the stroboscopic distance shows memory of training amplitude by developing a local minimum which appears exactly when $\gamma_{\mathrm{read}} = \gamma_{\mathrm{train}}$. But unlike the parallel read protocol, as the training amplitude increases, this local minimum occurs at $\gamma_{\mathrm{read}} < \gamma_{\mathrm{train}}$. The value of the $\gamma_{\mathrm{read}}$ at which such a minimum occurs is well below the training amplitude corresponding to the irreversibility transition $\gamma_{irr}$. This implies that the memory of training amplitude cannot be perfectly revealed through a sequential readout protocol even below the irreversibilty transition.

The stroboscopic distance is non zero for $\gamma_{read} < \gamma_{train}$, but depending on the amplitude of training $\gamma_{train}$ the stroboscopic distance could either be zero at $\gamma_{read} = \gamma_{train}$ or assume a finite positive value. In the simpler case of parallel read-out, a non-zero value of the stroboscopic distance at $\gamma_{read} = \gamma_{train}$ can be due to the presence of multi-period limit cycles and/or due to the fact that a limit cycle was not found. In the case of sequential read-out, this can additionally also be due to the history dependent nature of the protocol. It should also be noted that a non-zero value of the stroboscopic distance for $\gamma_{read} < \gamma_{train}$ is expected when the global stress-strain response of the trained state under a shear cycle with amplitude $\gamma_{train}$ shows non-zero hysteresis.

A non-zero contribution to the stroboscopic distance at $\gamma_{read} = \gamma_{train}$ due to multi-period limit cycles underlines the effect of frustrated interactions through the Eshelby kernel present in our model. A non-interacting Preisach or a Random Field Ising Model for ferromagnets under external driving cannot admit multi-period limit cycles and therefore such contributions to the stroboscopic distance is

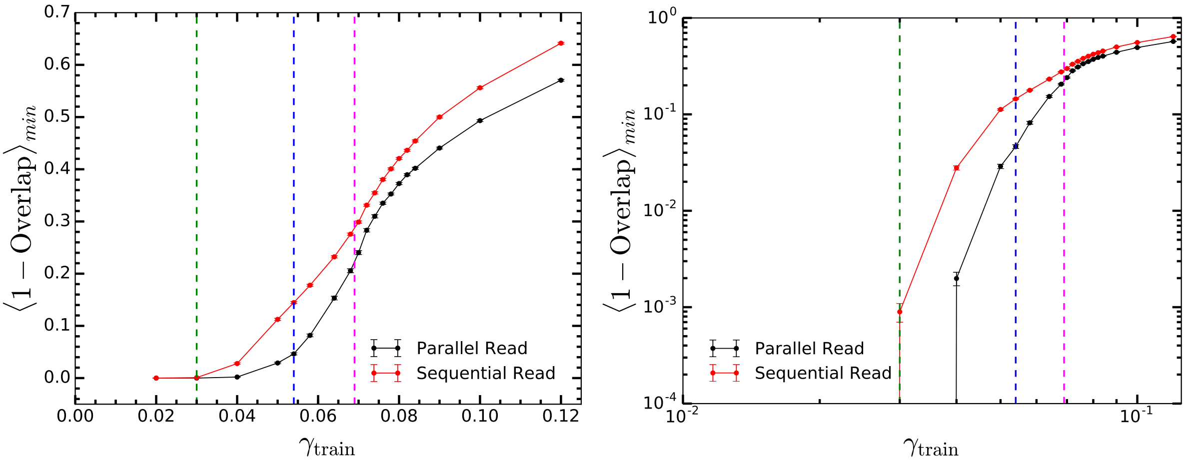

Fig. 4.6 Evolution of the value of the minimum of the stroboscopic distance (corresponding to the cusp in the vicinity of $\gamma_{train}$ as in Figure 4.5) versus training amplitude for parallel and sequential read-out protocols. (Left) On Lin-Lin scale (Right) On Log-Log scale. Dashed line in green represents the maximum training amplitude till which only period one limit cycles are found. Dashed line in blue represents the maximum training amplitude till which all the samples find limit cycles. Dashed line in magenta represents the irreversibility transition $\gamma_{irr}(= 0.06899)$ at which only 50% of the samples find limit cycles.

not possible in these kind of models [97, 113]. On the other hand, spin glass models [36] and mean-field hysteron based models [72] with interactions that can both enable or suppress local plastic rearrangements admit multi-period limit cycles in the steady-state. It would thus be interesting to probe the role of the spatial resolution of the Eshelby kernel on the memory of training and drawing comparisons with spin glass or especially mean-field hysteron based models where such spatial features in the interaction are absent but nevertheless admit multi-periodicity in the steady state while being driven quasistatically.

We now show a more quantitative comparison of the two types of read-out protocols that have been considered to reveal memory of training. We define a quantity $\langle 1 - Overlap \rangle_{\text{min}}$ which measures the value of the local minimum of $\langle 1 - Overlap \rangle$ that appears at $\gamma_{\text{read}} \leq \gamma_{\text{train}}$ for the respective read-out protocols in the Figures 4.5. At low values of $\gamma_{\text{read}}$, $\langle 1 - Overlap \rangle_{\text{min}}$ is obtained at $\gamma_{\text{read}} = \gamma_{\text{train}}$. When the training amplitude is increased further, $\langle 1 - Overlap \rangle_{\text{min}}$ is achieved at $\gamma_{\text{read}} < \gamma_{\text{train}}$. In the Figure 4.6 (Left), we see that the value of $\langle 1 - Overlap \rangle_{\text{min}}$ is lower for the parallel read-out than the sequential read-out protocol irrespective of the training amplitude. Therefore, the memory of training amplitude is revealed more precisely using a parallel read-out than a sequential protocol. At low training amplitudes we always find limit cycles. The dashed vertical line in green at $\gamma_{\text{train}} = 0.03$ represents the largest value of the training amplitude for which the trained state always finds limit cycles but of period one only. Since the parallel read-out protocol shears the trained state for one cycle only, we therefore expect, for training amplitudes less than or equal to 0.03, that $\langle 1 - Overlap \rangle_{\text{min}}$ is zero. This is confirmed in the Figure 4.6 (Right) where on the log-log scale we can see that a parallel read-out protocol shows a zero value of $\langle 1 - Overlap \rangle_{\text{min}}$ at least till $\gamma_{\text{train}} = 0.03$. The sequential read-out protocol at $\gamma_{\text{train}} = 0.03$

in the same figure, however, shows a non-zero value of $\langle 1 - Overlap \rangle_{\mathrm{min}}$ confirming our expectation that the non-zero contribution to the stroboscopic distance for the sequential read-out protocol can also additionally be due to the history dependent nature of the protocol.

We now take a closer look at the effect of multi-period limit cycles on memory of training amplitude using Figure 4.6. For $\gamma_{\mathrm{train}}$ between 0.03 and 0.054, marked by the region between the dashed vertical lines in green and blue, all the trained states find limit cycles but some of them have period greater than one. We observe that the difference in the value of $\langle 1 - Overlap \rangle_{\mathrm{min}}$ for sequential and parallel read-out protocol increases with $\gamma_{\mathrm{train}}$. In fact, the effect of multi-periodic limit cycles on memory of training amplitude is more drastic for the sequential read-out protocol. As an example, at the largest training amplitude in this range, that is, $\gamma_{\mathrm{train}} = 0.054$, the value of $\langle 1 - Overlap \rangle_{\mathrm{min}}$ for parallel read-out protocol is around 0.045 while the value for sequential read-out protocol is around 0.145. This is roughly a factor of three difference in the value of $\langle 1 - Overlap \rangle_{\mathrm{min}}$ even at a training amplitude where all the trained states find limit cycles. We also note from Figure 4.6 (Right) that the smallest $\gamma_{\mathrm{train}}$ for which $\langle 1 - Overlap \rangle_{\mathrm{min}}$ takes a non-zero value in the parallel read-out protocol is 0.04, at which we first begin to observe multi-period limit cycles.

For $\gamma_{\mathrm{train}} > 0.054$, the value of $\langle 1 - Overlap \rangle_{\mathrm{min}}$ will also be affected by trained states which could not find limit cycles. Interestingly, the effect of such trained states is to decrease the difference in the value of $\langle 1 - Overlap \rangle_{\mathrm{min}}$ between sequential and parallel read-out protocol. We observe such a behavior till $\gamma_{\mathrm{train}} \sim \gamma_{\mathrm{irr}}$. As $\gamma_{\mathrm{train}}$ is increased further from $\gamma_{\mathrm{irr}}$, we see a reversal of the trend where the difference of $\langle 1 - Overlap \rangle_{\mathrm{min}}$ between the two read-out protocol increases.

The value of $\gamma_{\mathrm{read}}$ at which $\langle 1 - Overlap \rangle_{\mathrm{min}}$ is found will be denoted by $\gamma_{\mathrm{read}}^{\mathrm{min}}$. To complement the observations of Figure 4.6, we plot $\gamma_{\mathrm{read}}^{\mathrm{min}}$ versus $\gamma_{\mathrm{train}}$ for the two read-out protocols. In Figure 4.7, we see that $\gamma_{\mathrm{read}}^{\mathrm{min}}$ is equal to $\gamma_{\mathrm{train}}$ till $\gamma_{\mathrm{train}} = 0.04$ implying perfect retrieval of memory of training amplitude through both the read-out protocols . For $\gamma_{\mathrm{train}} > 0.04$, $\gamma_{\mathrm{read}}^{\mathrm{min}} = \gamma_{\mathrm{train}}$ for the parallel read-out protocol for training amplitudes upto 0.075. However, for the sequential read-out protocol $\gamma_{\mathrm{read}}^{\mathrm{min}} < \gamma_{\mathrm{train}}$ for $\gamma_{\mathrm{train}} > 0.04$ implying that the memory of training amplitude can not be revealed perfectly well below the irreversibility transition through such a protocol. We also note that $\gamma_{\mathrm{read}}^{\mathrm{min}}$ for sequential read-out protocol is always less than the parallel read-out protocol for $\gamma_{\mathrm{train}} > 0.04$. Finally, irrespective of the read-out protocol we observe that $\gamma_{\mathrm{read}}^{\mathrm{min}} \leq \gamma_{\mathrm{train}}$.

### 4.3.2 Variance of the stroboscopic distance

Here we show that sample to sample fluctuations in the stroboscopic distance, quantified through the variance, can also encode memory of training amplitude. We emphasise that we are considering parallel read protocol for purpose of our discussion in this section. Results are obtained at system size equals $32 \times 32$ and number of realisations equals 800. At small to moderate amplitudes, in the parallel read-out protocol, the memory of training reveals itself as a local minimum in the variance at $\gamma_{read} = \gamma_{train}$. When the amplitude of training is increased further, the variance shows the memory of training at $\gamma_{read} = \gamma_{train}$

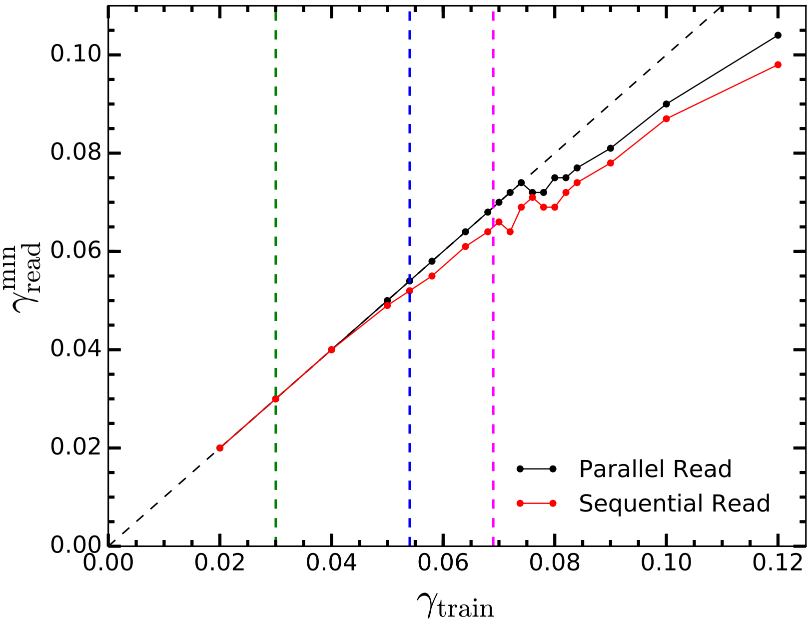

Fig. 4.7 $\gamma_{\mathrm{read}}^{\mathrm{min}}$, that is, $\gamma_{\mathrm{read}}$ corresponding to $\langle 1 - Overlap \rangle_{\mathrm{min}}$ versus $\gamma_{\mathrm{train}}$ for seqential and parallel read-out protocols. Vertical lines in green, blue, and magenta represent the same as in Figure 4.6. Black dashed line with slope one is a guide helping our comparison of the two read-out protocols. System size $= 16 \times 16$ for which $\gamma_{\mathrm{irr}} = 0.06899$.

as a local maximum instead. The change in the nature of local extrememum in the variance happens due to appearance of multi-period limit cycles in the trained state as $\gamma_{train}$ is increased.

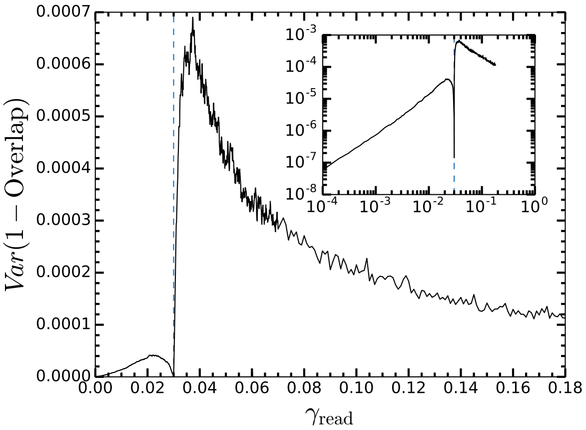

Fig. 4.8 Memory of training amplitude: Variance of stroboscopic distance versus $\gamma_{read}$ for parallel read-out protocol. Dotted vertical line represents the value of the training amplitude. System size $= 32 \times 32$, poorly aged (PA) samples. $\gamma_{train} = 0.03 < \gamma_{irr}$. Inset: Same figure as in the main panel on a Log-Log scale.

In Figure 4.8, we see a local minimum in the variance of the stroboscopic distance at $\gamma_{read} = \gamma_{train}$ reflecting memory of training amplitude. For $\gamma_{read} \leq \gamma_{train}$, increasing $\gamma_{read}$ first increases the variance in the stroboscopic distance which takes a local maximum and then starts decreasing towards the local minimum obtained at $\gamma_{read} = \gamma_{train}$. For $\gamma_{read} > \gamma_{train}$, we see a steep increase in the variance leading to another significantly larger maximum (global) beyond which it starts to decrease. The inset of the figure plots the same result on log-log scale showing a power law increase in variance for $\gamma_{read} < \gamma_{train}$ with an exponent roughly equal to 1.0 and a power-law decay for $\gamma_{read} > \gamma_{train}$ with the nearly the same exponent. The exponents of the two power laws do change with $\gamma_{train}$ but we do not elaborate on this aspect further. Since we are using a parallel read out protocol that shears the trained state for single cycle only, when the all the trained states find limit cycles and with period one only, we expect the variance of the stroboscopic distance to drop to zero when $\gamma_{read} = \gamma_{train}$. The inset does not show the variance dropping to zero at $\gamma_{read} = \gamma_{train}$ because some samples admit multi-period limit cycles.

We also see that the variance in the stroboscopic distance is much smaller for $\gamma_{read} < \gamma_{train}$ than when $\gamma_{read} > \gamma_{train}$. Such a behaviour is expected as the trained state at low $\gamma_{train}$ always finds limit cycles. As discussed in Chapter 5, limit cycles by definition always belong to a strongly connected component (SCC) of the t-graph. Since transitions within an SCC are reversible, we expect that the mesostates that they connect are not very different in their event fields. Put differently, the variance over the event field calculated over mesostates belonging to an SCC must be small. When $\gamma_{read}$ is increased beyond $\gamma_{train}$, we expect to leave the SCC that confines the limit cycle. The shear drive performed during the read-out phase could span multiple SCCs in this case. Event fields of mesostates belonging to different SCCs connected by plastic events could lead to very different event fields as the transitions are irreversible. Such irreversible transitions must be generating an increased variance over the event fields over mesostate trajectories spanning multiple SCCs. This could explain the contrasting values of variance for read amplitudes above and below $\gamma_{train}$. Finally, for $\gamma_{read} \gg \gamma_{train}$ we expect that the read state and the trained state do not match in the event fields at all and therefore the stroboscopic distance is 1 for each sample implying a zero value for the variance in this limit. An interesting feature that we don't understand yet is why does the variance decrease with increasing $\gamma_{read}$ at higher values.

### Effect of training amplitude

The aim of this section is to examine the effect on the memory of training amplitude shown in the variance of the stroboscopic distance versus $\gamma_{read}$ at different values of training amplitude sweeping across the irreversibility transition. We consider four different training amplitudes: $0.043, 0.048, 0.050$, and $0.057$. System size equals $32 \times 32$ and the irreversibility transition at this system size is at $\gamma_{irr} = 0.0499$. In Figure 4.9, we show the effect of these training amplitudes in the variance of the stroboscopic distance versus $\gamma_{read}$. The local maximum in the variance for $\gamma_{read} < \gamma_{train}$ is not present for any of the training amplitudes considered. We see that if $\gamma_{read} > \gamma_{train}$ and $\gamma_{read}$ is large then, irrespective of the training amplitude, variance decreases with increasing $\gamma_{read}$. When $\gamma_{read} < \gamma_{train}$ then at small $\gamma_{read}$ values, irrespective of the training amplitude, variance increases with increasing $\gamma_{read}$. The dependence of the variance close to $\gamma_{read} = \gamma_{train}$ on either sides can show different behaviors depending on the value of $\gamma_{train}$. Our choice of $\gamma_{train}$ in Figure 4.9 covers all possible behaviors.

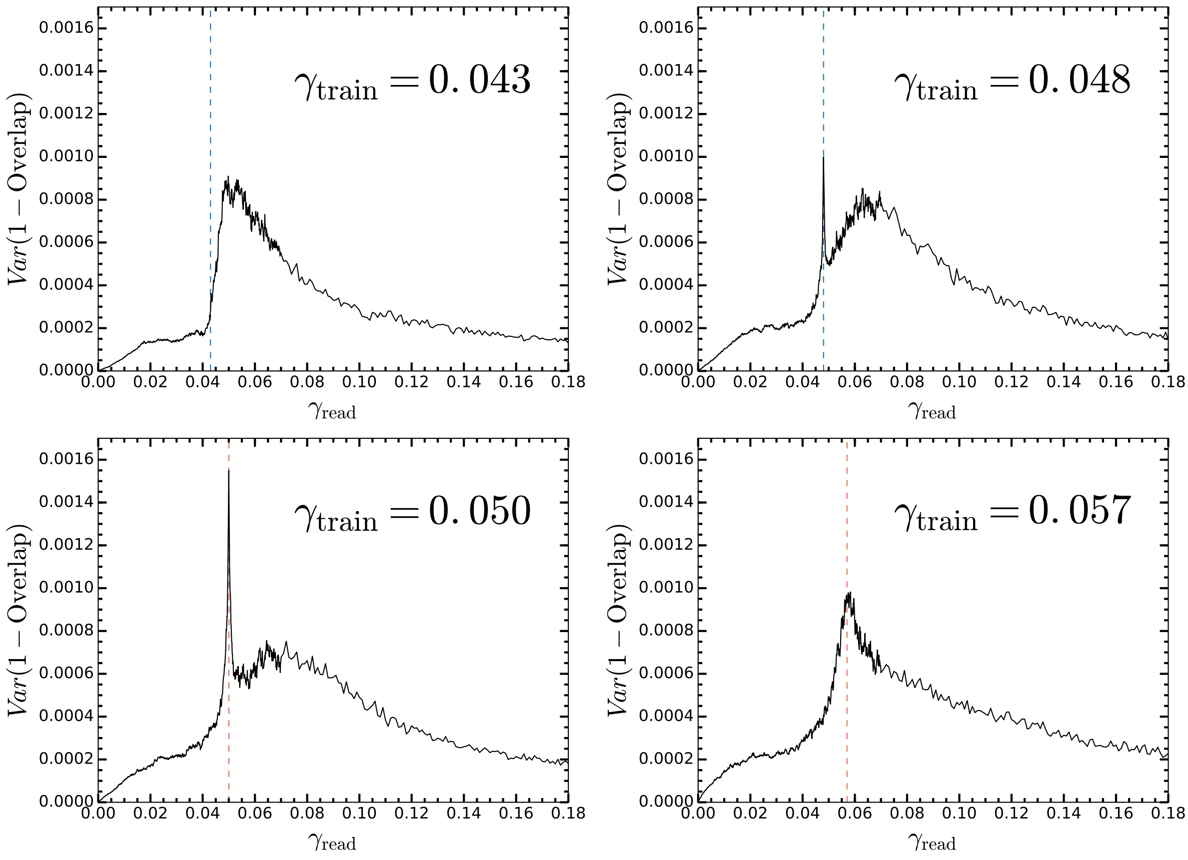

Fig. 4.9 Variance of the stroboscopic distance versus $\gamma_{read}$ for parallel read-out protocol at $\gamma_{train} = 0.043$ (Upper Left), 0.048 (Upper Right), 0.050 (Lower Left), and 0.057 (Lower Right). Dotted vertical lines represent the value of the training amplitude in the corresponding figures. System size $= 32\times32$, poorly aged (PA) samples. $\gamma_{irr} = 0.0499$.

We first focus on the evolution of the variance at $\gamma_{read} = \gamma_{train}$ as a function of increasing training amplitude across the four different figures in Figure 4.9. At $\gamma_{train} = 0.043$, we observe that the variance is non-zero and such that a memory of training amplitude is visibly difficult to ascertain as a local extremum. Considering the effect of $\gamma_{train}$ in the increasing sequence of $0.048, 0.050$, and 0.057, we see a non-monotonic change in the variance across the irreversibility transition. We see that the memory of training amplitude at such values of $\gamma_{train}$ appear as a local/global maximum which is contrastingly different from the behavior at low training amplitudes such as in Figure 4.8. We also note that such a global maximum persists at training amplitude 0.057 at which no trained state is able to find a limit cycle. Through Figure 4.9 (Lower-right), we also conclude that if $\gamma_{train}$ is well above the irreversibility transition such that no trained state finds limit cycle then the variance starts decreasing immediately upon exceeding $\gamma_{read} = \gamma_{train}$. This is in sharp contrast to training amplitudes well below the irreversibility transition, as in Figure 4.8, where the variance for $\gamma_{read}$ upon exceeding $\gamma_{train}$ first shows a sharp increase to a maximum before showing a decrease with $\gamma_{read}$.

Finally in figure 4.10, we show the maximum of variance of the stroboscopic distance calculated over $\gamma_{read}$ as a function of $\gamma_{train}$. We see a non-monotonic change in the maximum of variance which peaks at the irreversibility transition at $\gamma_{train} = \gamma_{irr}$. This also serves as an alternative characterisation of the irreversibility transition.

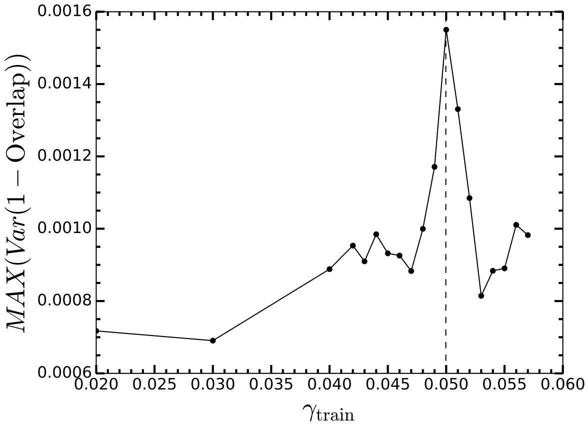

Fig. 4.10 Maximum of the variance of the stroboscopic distance calculated over $\gamma_{read}$ versus training amplitude $\gamma_{train}$. Dashed vertical line represents the irreversibility transition $\gamma_{irr} = 0.0499$.

To understand the change in the nature of variance at $\gamma_{read} = \gamma_{train}$, we plot the distribution of the stroboscopic distance at $\gamma_{read} = \gamma_{train}$ for different values of training amplitude $\gamma_{train}$. We see in the Figure 4.11 (Left) that at small $\gamma_{train}$ values, the stroboscopic distance is a Dirac delta distribution located at zero stroboscopic distance. This means that all the samples find limit cycles with period equals one, implying that the trained state match the corresponding read-out state perfectly during the read-out phase. As the training amplitude is increased, limit cycles with period greater than one also start to appear. The stroboscopic distance is zero for samples that find period one limit cycles and non-zero for samples with period greater than one. A distribution of the stroboscopic distance at these training amplitudes therefore start showing a bi-modal distribution.

As the training amplitude is increased further, the distance between the two sub-distributions start increasing as some of the samples are not able to find any limit cycles at all. Maximum variance in the stroboscopic distance is expected when the two sub-distributions are furthest apart but also similar in weight. This in our simulations happen at the irreversibility transition $\gamma_{train} = \gamma_{irr}$ where only half of the samples are able to find limit cycles. The bi-modal structure of the distribution vanishes completely when none of the samples are able to find limit cycles. The distribution shifts rightwards with increasing $\gamma_{train}$ thereafter.

To answer why the distribution becomes bi-modal, we select $\gamma_{train}$ values at which we clearly see a bi-modal distribution and do the following: Find the distribution of the stroboscopic distance over

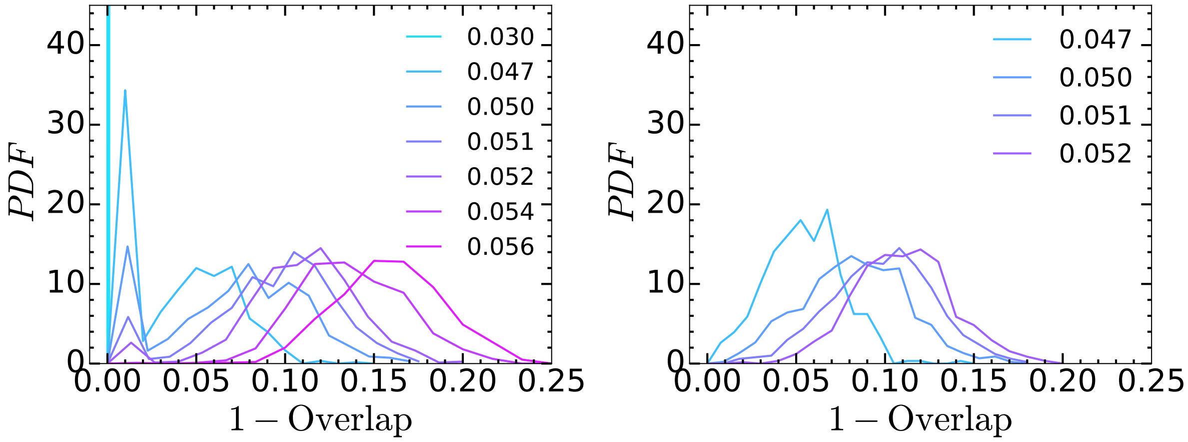

Fig. 4.11 Distribution of the stroboscopic distance at $\gamma_{read} = \gamma_{train}$ for parallel read-out protocol at $\gamma_{train}$ as listed in the legend. (Left) Distribution over all the samples (Right) Distribution over all the samples excluding those with period one limit cycles. System size $= 32\times32$, poorly aged (PA) samples. $\gamma_{irr} = 0.0499$.

samples that do not have period one limit cycles. We see in the Figure 4.11 (Right) that the bi-modal structure in the distribution vanishes. This means that the bi-modal structure in the distribution is due to samples holding period one limit cycles. The fraction of samples finding period one limit cycles decreases with increasing $\gamma_{train}$. As $\gamma_{train}$ is increased further period one limit cycles are not found at all and the bi-modal distribution of the stroboscopic distance becomes uni-modal thereafter. This also explains the non-monotonicity in the variance of the stroboscopic distance at $\gamma_{read} = \gamma_{train}$.

Finally, based on the above observations we speculate that the sharp local/global maximum in the variance of the stroboscopic distance at $\gamma_{read} = \gamma_{train}$ is due to period one limit cycles which do not contribute as much to the variance when $\gamma_{read} \neq \gamma_{train}$.

### Discussions

At low training amplitudes, the variance develops a local minimum and drops to zero at $\gamma_{read} = \gamma_{train}$. This is expected in the parallel read protocol as single shear cycles on the trained state are performed. A zero variance in the overlap implies only period one limit cycles in the trained state. As the training amplitude increases, multi-period limit cycles start to emerge. Different initial states, driven at fixed training amplitude, can lead to limit cycles with different periods. The emergence of multi-periodicity in the steady state together with sample to sample variability of the period of limit cycles causes the variance to become finite at the local minimum, that is, at $\gamma_{read} = \gamma_{train}$. Surprisingly, a local minimum at $\gamma_{read} = \gamma_{train}$ transitions into a sharp local maximum as the training amplitude approaches and increases past the irreversibility transition. Increasing the training amplitude further, the local maximum at $\gamma_{read} = \gamma_{train}$ still persists but becomes diffuse instead. To understand the observed behavior in the variance, we list down the factors affecting the value of the stroboscopic distance:

1. The nature of plastic transitions present in the shear cycle during the read-out phase. A plastic transition is reversible if it is inside an SCC and irreversible if it connects two different SCCs. If a read cycle on the trained state consists of reversible transitions only, then we expect the value of the stroboscopic distance to be small. On the other hand, if irreversible plastic transitions populate the read-cycle then we expect the same value to be high.

2. The success probability of finding limit cycles. This will particularly be more relevant for the value of the stroboscopic distance calculated for $\gamma_{read} < \gamma_{train}$. For a given $\gamma_{read}$ and $\gamma_{train}$, samples that do not find limit cycles will contribute differently to the stroboscopic distance than those which don't.

3. A single shear cycle at a read amplitude $\gamma_{read} = \gamma_{train}$ (as is the case in our parallel read protocol) on a trained state with a multi-period limit cycle will lead to a read state different from the trained state. Such a sample would then contribute to a non-zero stroboscopic distance. If different samples end in trained states with limit cycles of different periods ($> 1$) then the value of the stroboscopic distance will also fluctuate from sample to sample thus giving a non-zero variance. Such sample to sample fluctuations in the stroboscopic distance can also exist among samples with the same period provided the period of the limit cycle is greater than 1. If all the samples, on the other hand, end in period one limit cycle then a single read cycle at a read amplitude $\gamma_{read} = \gamma_{train}$ will give a read state that is identical to the trained state. The value of the stroboscopic distance will be the same (and equal to zero) for all the samples and therefore the variance will be zero.

4. Depending on the training amplitude, various possibility on the ratios of reversible to irreversible transitions can exist while performing a full read cycle on the trained state. Their relative population can further be decomposed based on the two possible shear direction within a read cycle. A change in these ratios will affect the read state relative to the trained state and hence change the value of the stroboscopic distance. This is distinct from the item listed above in 3 because it accounts for the effect of trained states that do not find limit cycles at all and thus irreversible transitions can be part of read cycles at $\gamma_{read} \leq \gamma_{train}$.

5. For the case when $\gamma_{read} < \gamma_{train}$, an additional factor affecting the value of the stroboscopic distance are plastic transitions that violate RPM. RPM violating transitions can be irreversible. We therefore expect that when RPM violations are absent the value of the stroboscopic distance could be lower.

### 4.3.3 Distributions of the trained state

Revealing memory of training amplitude requires performing a read-out protocol that involves shear driving the trained state. We now ask if the trained state alone holds features of the training amplitude? For this purpose, we look at the distributions of the local distance to stress thresholds in the forward and reverse slip direction. We also compare the distributions of the trained state with the initial undeformed

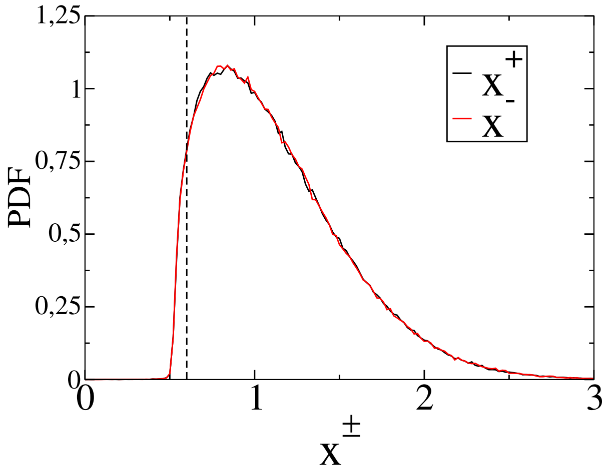

Fig. 4.12 PDF of local distance to stress threshold in the forward $x^{+}$ and reverse $x^{-}$ slip direction for the undeformed initial state. Dotted vertical line corresponds to a value equal to $2\mu\gamma_{train}$ on the horizontal axis which is useful for comparisons drawn in the text and Figure4.14. System size $=$ 32×32, poorly aged (PA) samples.

state to contrast the effect of mechanical training on the sample. We highlight again at this point that the initial undeformed state is generated using the thermal and aging glass preparation protocol as discussed in Chapter 3.

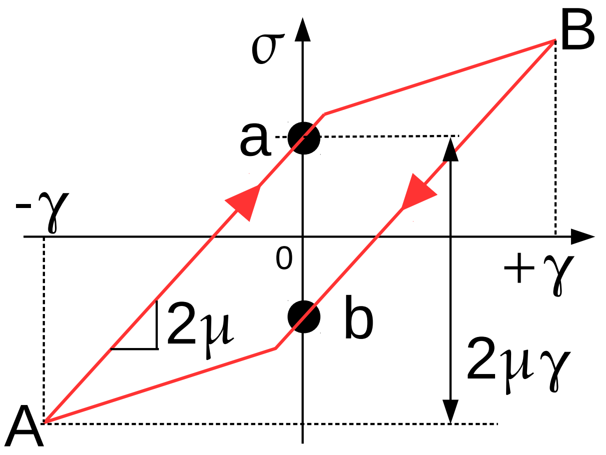

Fig. 4.13 Schematic of a typical stress-strain hysteresis curve obtained after cycling a trained state ‘a’ for a single shear cycle at an amplitude $\gamma = \gamma_{train}$. Response during a half cycle, $A \rightarrow a$ for example, consists of an almost perfect elastic response (no plastic events) with a corresponding increase in stress $\sigma$ that is equal to $2\mu\gamma$ indicating memory of training amplitude $\gamma_{train}$.

We recall from Chapter 2 that the local plastic strengths for the mesoscopic cell $(i,j)$ in the positive and negative directions are defined as $x^{+}_{ij} = \sigma^{+}_{ij} - \sigma_{ij}$ and $x^{-}_{ij} = \sigma_{ij} + \sigma^{-}_{ij}$, respectively. These measure the amount of local stress required to trigger a plastic event in the respective directions. Here, $\sigma^{+}_{ij}$ and

$\sigma^-_{ij}$ are the local stress thresholds in the two directions and $\sigma_{ij}$ is the local internal stress at cell $(i,j)$ associated to interactions with other cells. In the following, we will drop the subscripts in $x^+_{ij}$ or $x^-_{ij}$ for our discussions.

Before we discuss results, we show an example hysteresis curve in Figure 4.13. Such a hysteresis loop is obtained from a training protocol for single memories at fixed training amplitude $\gamma$. The training protocol ends in a trained state as marked by $a$ in the figure on the hysteresis loop. The response to a shear cycle in strain of the form $0 \rightarrow \gamma \rightarrow -\gamma \rightarrow 0$ on such a trained state is shown in Figure 4.13 during which the sample takes the route $a \rightarrow B \rightarrow A \rightarrow a$. We will generate distributions of $x^+$ and $x^-$ at points marked as $a$ and $b$ to check if memory of the training amplitude exists. We also emphasise through this figure that the response to strain during $-\gamma \rightarrow 0$ and $\gamma \rightarrow 0$ is largely elastic with a shear modulus roughly of the initial undeformed state and equals $2\mu$. This is also depicted in $A \rightarrow a$ and $B \rightarrow b$ part of the hysteresis loop. In fact, Figures 3.8 in Chapter 3 already hint such an elastic response with a corresponding change in global stress that equals $2\mu\gamma$. We note again that $\gamma$ is the amplitude of training that generated the trained state $a$.

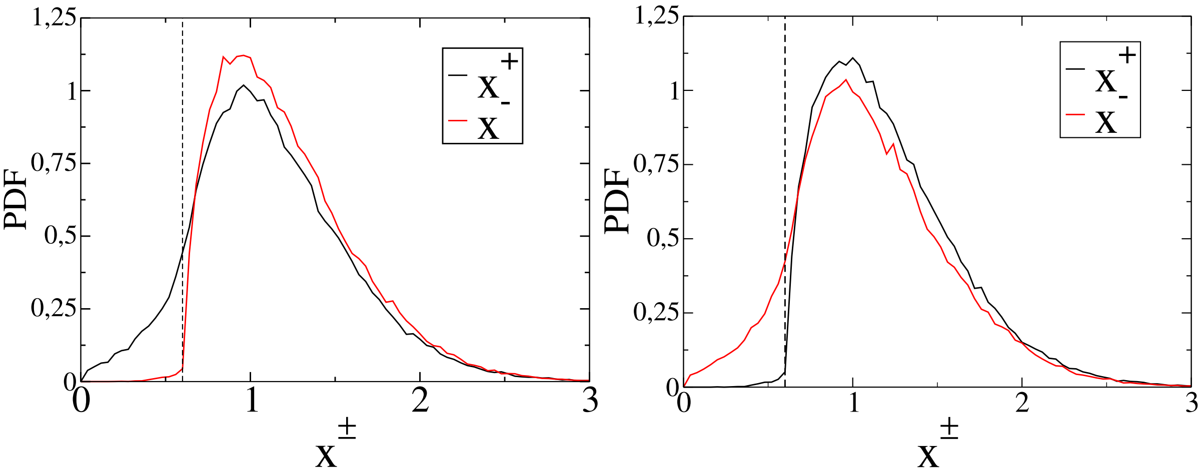

Fig. 4.14 PDF of local distance to stress threshold in the forward $x^+$ and reverse $x^-$ slip direction for (Left) The trained state 'a' and (Right) State 'b'. States 'a' and 'b' are marked on the schematically shown hysteresis curve in figure 4.13. Dotted vertical line corresponds to a value equal to $2\mu\gamma_{train}$ on the horizontal axis. System size $=$ $32 \times 32$, poorly aged (PA) samples. $\gamma_{train} = 0.03 < \gamma_{irr}$.

In Figure 4.12, we see that the distributions of $x^+$ and $x^-$ are identical for the initial undeformed state. Such an observation is expected as the glass preparation protocol treats the two available local slip directions for a cell equally. The shear modulus of the undeformed state for small deformations would thus be identical if sheared in the forward or reverse direction. We now show the effect of training and look at the distributions of $x^+$ and $x^-$ in the trained state, such as $a$ marked in the Figure 4.13. The distributions of $x^+$ and $x^-$ sampled at $a$ are presented in the Figure 4.14 (Left). In contrast to the distributions of the initial state, we see that the distributions of $x^+$ and $x^-$ are not identical in the trained state. The training protocol applied on the initial undeformed state has created an asymmetry in the distributions with respect to forward and reverse shear directions. In the same figure, the distribution of $x^-$ shows a sharp kink at $2\mu\gamma_{train}$ revealing the memory of training. This also raises the question whether such asymetries in the distribution of the trained state are a necessary prequisite for memory of training amplitude in amorphous solids?

We now sample the distributions of $x^+$ and $x^-$ on state $b$ marked in the Figure 4.13. In the Figure 4.14 (Right), we see that the distributions are still asymmetric with respect to forward and reverse shear direction but the roles of $x^+$ and $x^-$ are reversed. The memory of training amplitude persists even in this state but now appears as a kink in the distribution of $x^+$ at $2\mu\gamma_{train}$.

Finally, from the Figure 4.14 (Right) for example, we note that the trained state has much higher probability of finding small value of $x^+$ than $x^-$. This means that a uniform shear on such a trained state would reveal a much softer response in the forwad shear direction than the reverse shear direction. This reflects a Bauschinger effect, a phenomena that has been studied well for amorphous solids under uniform shear using particle scale simulations [91] where it reveals a memory of shear direction.

## 4.4 Memory of shear direction

Given the trained state only and in absence of any other information, can we tell the direction in which the sample was driven to the trained state? The answer is yes, which we explain in this section. We also consider the two read-out protocols, parallel and sequential, to test the robustness of such a memory.

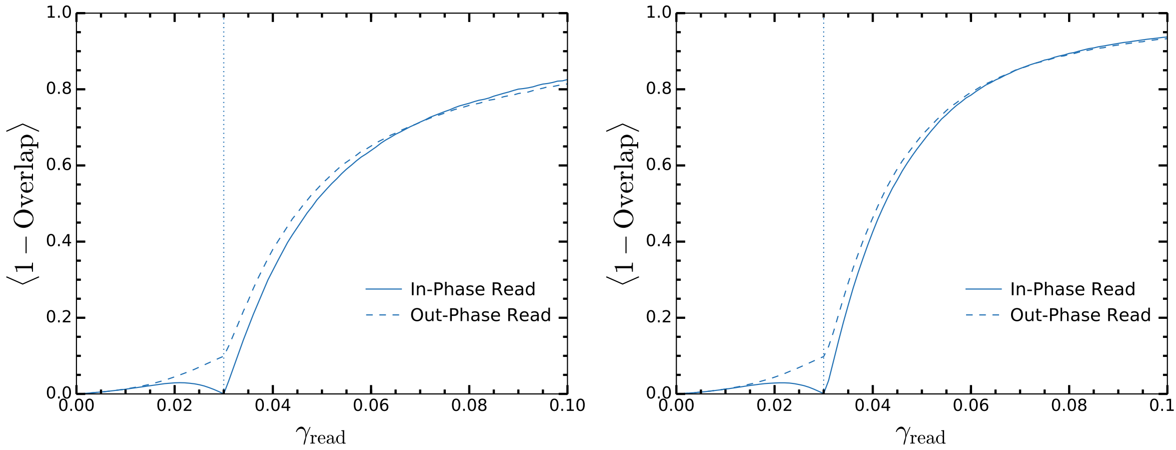

Fig. 4.15 Memory of direction: stroboscopic distance versus $\gamma_{read}$ for (Left) Parallel read-out protocol and (Right) Sequential read-out protocol. Solid curve represents the response to in-phase read-out while the dashed curve is the response to an out-phase read-out. Dotted vertical line on the $\gamma_{train}$-axis represent the value of the training amplitude which equals 0.03. System size = 16 × 16, poorly aged (PA) samples. $\gamma_{train} < \gamma_{irr} = 0.07$.

We consider three different training amplitudes $\gamma_{train} = 0.03,\ 0.05,\ 0.076$ and present results for each. We consider a system size of 16 × 16 for which the irreversibility transition is $\gamma_{irr} = 0.07$. We recall that the undeformed state is subjected to a training and read-out protocol as demonstrated in Section 4.2.1 for single memories.

We first describe results for $\gamma_{train} = 0.03$. In the Figure 4.15 (Left), we use a parallel read-out protocol to reveal the memory of shear direction. An in-phase read-out protocol displays a non-monotonic response in stroboscopic distance for $\gamma_{read} < \gamma_{train}$, exhibiting a local maximum before showing a sharp local minimum and dropping to zero at $\gamma_{read} = \gamma_{train}$. For $\gamma_{read} > \gamma_{train}$, the stroboscopic distance increases monotonically. An out of phase read-out protocol reveals a different response. In the same figure we see that, for $\gamma_{read} < \gamma_{train}$, the stroboscopic distance now shows a monotonically increasing response. A memory of training amplitude exists but appears as a kink at a finite value in the stroboscopic distance at $\gamma_{read} = \gamma_{train}$. For $\gamma_{read} > \gamma_{train}$, the stroboscopic distance increases monotonically. We thus conclude that although both in-phase and out-phase read-out protocol reveal memory of training amplitude, they do so in contrastingly different ways. This difference in response thus serves as a tool to determine the memory of shear direction in which the sample was trained during the training phase. As a test of robustness of the memory of shear direction, we now present the response of the trained state to a sequential read-out protocol. We see a similar response in the Figure 4.15 (Right).

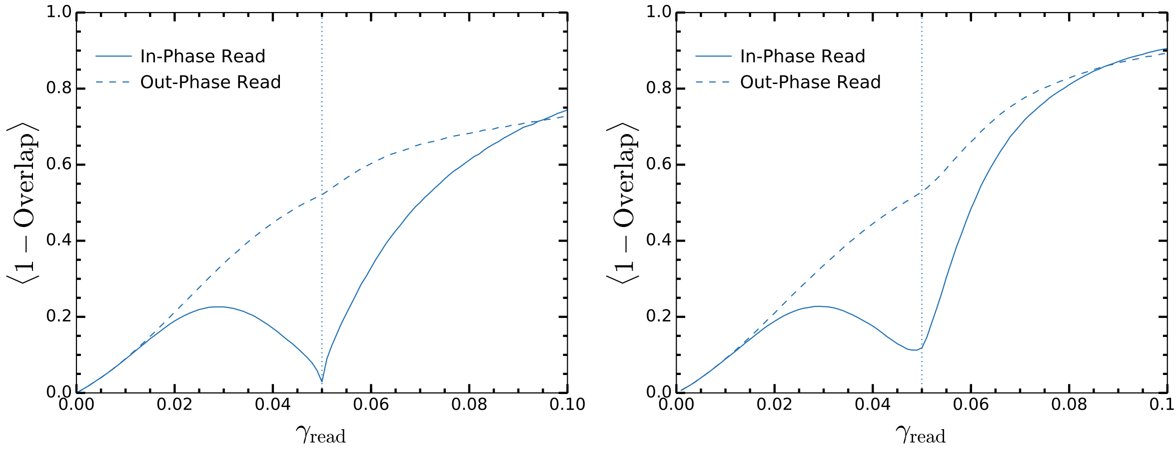

Fig. 4.16 Memory of direction: stroboscopic distance versus $\gamma_{read}$ for (Left) Parallel read-out protocol and (Right) Sequential read-out protocol. Solid curve represents the response to in-phase read-out while the dashed curve is the response to an out-phase read-out. Dotted vertical line on the $\gamma_{train}$-axis represent the value of the training amplitude which equals 0.05. System size = $16 \times 16$, poorly aged (PA) samples. $\gamma_{train} < \gamma_{irr} = 0.07$.

We now test the effect of increasing $\gamma_{train}$ on our observations. For this purpose we set $\gamma_{train} = 0.05$ in the training phase. Figure 4.16 (Left) and (Right) show stroboscopic distance versus $\gamma_{read}$ for parallel and sequential read-out protocol, respectively. We again see that the response to an in-phase read-out is different from an out-phase read-out protocol implying that the trained state has a memory of the direction of shear. However, the memory of training amplitude in the out-phase read-out protocol seen through a kink in the stroboscopic distance at $\gamma_{read} = \gamma_{train}$ becomes visibily less distinct. We stress again at this point that the memory of shear direction is revealed solely based on how the trained state responds to a read-out operation which precludes any prior information about the history of deformation during the training phase.

We also show for comparison the same curves for $\gamma_{train} > \gamma_{irr}$. In Figure 4.17, we see that the memory of direction can be revealed even above the irreversibility transition. The memory of training amplitude present as a kink in the stroboscopic distance in the out-phase read-out at $\gamma_{read} = \gamma_{train}$ is now completely absent.

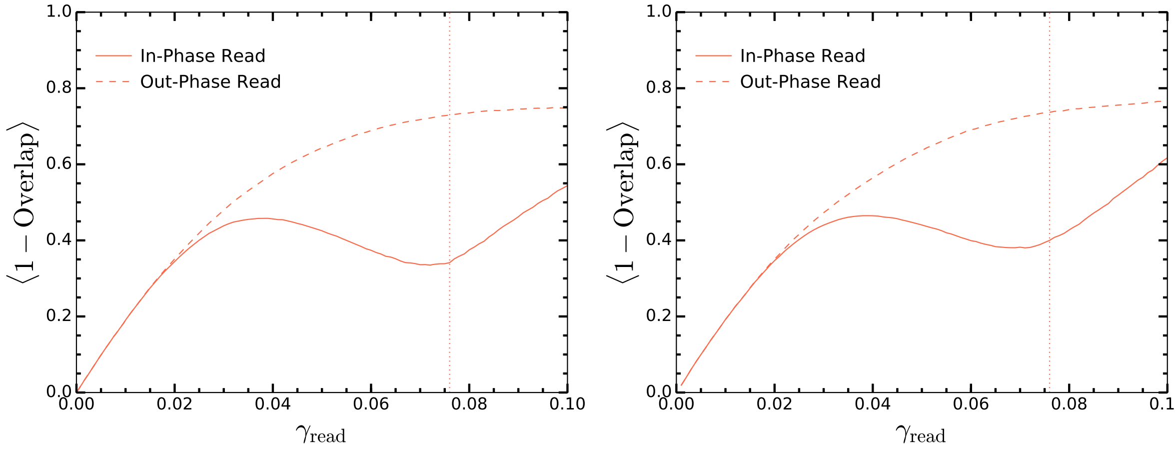

Fig. 4.17 Memory of direction: stroboscopic distance versus $\gamma_{read}$ for (Left) Parallel read-out protocol and (Right) Sequential read-out protocol. Solid curve represents the response to in-phase read-out while the dashed curve is the response to an out-phase read-out. Dotted vertical line on the $\gamma_{train}$-axis represent the value of the training amplitude which equals 0.076. System size $=$ $16 \times 16$, poorly aged (PA) samples. $\gamma_{train} > \gamma_{irr} = 0.07$.

To summarise, a read-out operation on a trained state reveals contrastingly different response depending on whether the read-out begun in-phase or out-phase with the training cycle. This difference in response during read-out helps determine the direction in which the sample was trained during the training phase. We see that this memory of shear direction can persist well past the irreversibility transition irrespective of the read-out protocol.

## 4.5 Comparison with the Preisach Model

In this section, we compare the memory of training amplitude in our elasto-plastic model against a non-interacting Preisach Model[97]. Before we proceed, we remind that the training and readout protocols correspond to those shown in Figure 4.1. For our study, we first set up the following definitions: Consider the set of *active* sites, i.e. cells that yield at least once over the full period of a limit cycle. Let us call this the set **T**. Also, consider the set of active sites during a read-out cycle and call it the set **R**.

We show that for any read-out amplitude and regardless of whether the read-out is in phase or out-of phase, as long as the read-out amplitudes is less than the training amplitude, the following holds:

$$\mathbf{R} \text{ is a subset of } \mathbf{T} \tag{4.2}$$

In order to show that equation 4.2 holds true in our EPM, we define a quantity $\Delta = |\mathbf{R} \setminus \mathbf{T}|$ which measures the number of elements that belong to $\mathbf{R}$ but not $\mathbf{T}$. Thus, $\Delta$ measures the number of cells which are active during the read-out cycle which were not active in the limit cycle. In the Figure 4.18, we show $\Delta$ divided by system size $N^2$, as we vary read-out amplitude and read-out protocol (in-phase vs. out-phase). This fraction is identically or at least very close to zero for $\gamma_{read} < \gamma_{train}$. That is, for $\gamma_{read} < \gamma_{train}$ in the figure, we see that $\Delta = 0$ for both the readout protocols. This implies that an in-phase readout cycle may make a different collection of cells active than an out-phase readout cycle but they both must be a subset of those cells that are active in the limit cycle. The figure also shows that both readout protocols reveal memory of training amplitude but the dependence of memory upon direction has been lost.

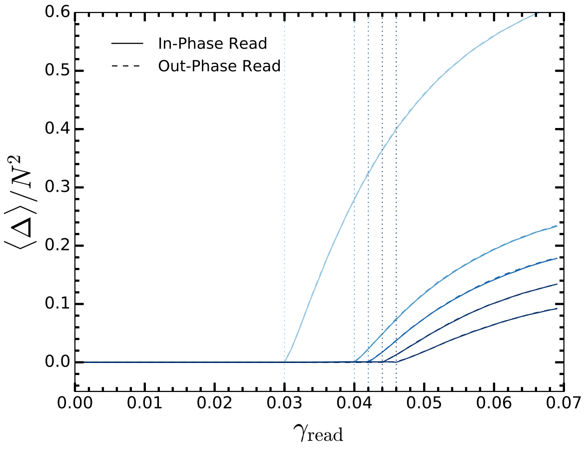

Fig. 4.18 $\Delta/(N^2)$ as a function $\gamma_{read}$ for parallel in-phase and parallel out-phase readout protocols. Angular brackets represent average over independent realisations. Dotted vertical lines represent the corresponding value of the training amplitude $\gamma_{train}$. System size $=$ 32×32, poorly aged (PA) samples.

We note that, in the case of the Preisach model equation 4.2 is necessarily true by virtue of the no-passing property. In the EPM model, because of the Eshelby kernel governing the interactions among the cells, we do not have the no-passing property so equation 4.2 need not hold. Indeed, we have observed violations of equation 4.2 in our elastoplastic model and can occur due to RPM violating transitions[78]. However, these violations are rare such that $\Delta$ is identically or at least very close to zero for $\gamma_{read} < \gamma_{train}$. As an example, consider a limit cycle obtained at $\gamma_{train} = 0.04$ at system size $=$ 32×32. A readout cycle for $\gamma_{read} < \gamma_{train}$ can make as many as $\sim 700$ cells active. Among these set of cells, we do not observe more than one cell which was not active in the limit cycle.

We therefore conclude that, despite the availability of multiple elastic branches in our quenched local landscape for a cell and Eshelby interactions among different cells, the limit cycles obtained in our EPM share a property in common with the Preisach model. It thus *appears* that what is really the memory is the selection of the set **T**. The read-out protocols are just different ways of probing this set **T** and – not surprisingly – some protocols are more useful than others.

## 4.6 Evolution of memory of training

A sample in our EPM under cyclic driving, upon locking into a limit cycle, ceases to evolve stroboscopically. We observe this both in the global stress-strain response when the hysteresis curve closes perfectly but also in the local field variables, for example, the local plastic strain field. Such a trained state can therefore not be trained further to increase the imprint of memory of training. A natural question arises: How does the system, starting from the initial state, acquire memory of training as it eveolves towards a limit cycle? The same question can also be asked for samples that are unable to find limit cycles when the driving amplitude is large.

We answer these questions using our EPM. For a given cycling amplitude $\gamma_{train}$, we subject an initial state for a fixed number of training cycles $\tau_{train}$. $\tau_{train}$ ranges 1 to 500 in our simulations. Average stroboscopic distance is obtained for different values of $\gamma_{read}$ by averaging over trained states at fixed $\gamma_{train}$ and $\tau_{train}$.

### 4.6.1 Learning the training amplitude

We set the training amplitude $\gamma_{train} = 0.05$ at a system size $32 \times 32$. We drive the initial undeformed state for a fixed number of driving cycles $\tau_{train}$ followed by a parallel read-out protocol on the trained state to evaluate the memory of training amplitude. By changing the value $\tau_{train}$, number of driving cycles since the undeformed initial state, we compare the evolution of memory of training amplitude.

In Figure 4.19 (Left), we see that the stroboscopic distance versus $\gamma_{read}$ at $\tau_{train} = 1$ does not indicate a memory of the training amplitude. However at $\tau_{train} = 10$, we see that the response becomes clearly non-monotonic in the interval $\gamma_{read} < \gamma_{train}$ with a local minimum in the stroboscopic distance appearing in the same interval close to $\gamma_{read} = \gamma_{train}$. As $\tau_{train}$ increases, we see that the local minimum shifts and at $\tau_{train} = 100$ establishes a sharp local minimum at $\gamma_{read} = \gamma_{train}$ indicating a clear memory of the training amplitude. The average number of training cycles required to reach a limit cycle, also called as steady state in the figure, at $\gamma_{train} = 0.05$ is 3640. This implies that a memory of training amplitude can thus be encoded in the sample well before reaching the steady state. For $\tau_{train} > 100$, we see that the local minimum in the stroboscopic distance stays at $\gamma_{read} = \gamma_{train}$ but displays a slow decay towards the steady state value with increasing $\tau_{train}$. Finally, we note that the local maximum of the stroboscopic distance, including the response upto it, in the interval $\gamma_{read} < \gamma_{train}$ remains almost unchanged for $\tau_{train} > 10$.

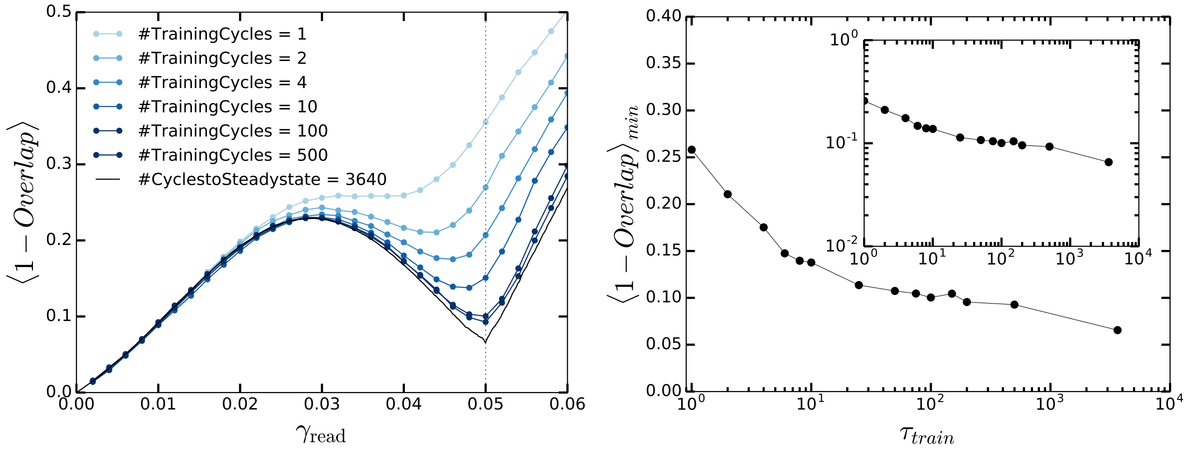

Fig. 4.19 (Left) Evolution of (single) memory of training: stroboscopic distance versus $\gamma_{read}$ for different number of training cycles for a fixed value of $\gamma_{train}$. Read-out curve showing memory of training amplitude in the steady-state is shown in black for comparison. Dotted vertical lines on the $\gamma_{train}$-axis represents the value of the training amplitude. (Right) Evolution of the value of the local minimum of the stroboscopic distance versus number of training cycles on a Lin-Log scale. Inset: Same curve as in the main panel shown on a Log-Log scale. System size = 32×32, poorly aged (PA) samples.

In Figure 4.19 (Right), we plot the value of the local minimum in the stroboscopic distance versus $\tau_{train}$. In the main panel we show the response on a lin-log scale while the inset shows the same response on a log-log scale. Through this figure we want to highlight the slow evolution in the value of the local minimum with increasing and higher values of $\tau_{train}$.

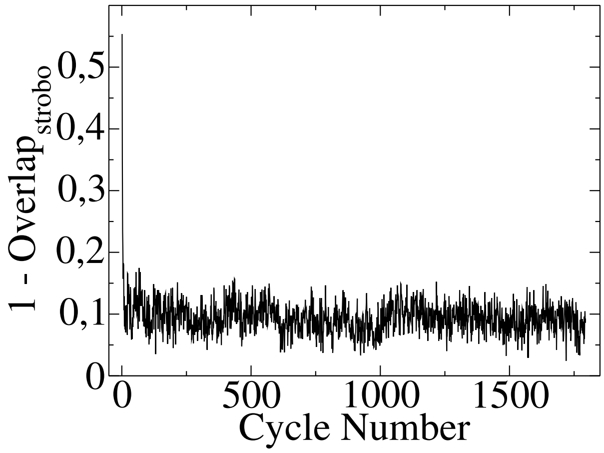

Fig. 4.20 Cycle to cycle stroboscopic distance versus cycle number for a particular realisation under cyclic driving at $\gamma_{train} = 0.05 \sim \gamma_{irr}$ before finding a limit cycle. System size = 32×32, poorly aged (PA) samples.

Next, we want to contrast the evolution of memory behavior against spatial plastic activity with driving cycles prior to finding a limit cycle. For this purpose, we define a quantity called cycle-to-cycle stroboscopic distance. Let $E(i,j)_{k+1}$ and $E(i,j)_k$ represent the event fields measured at the end of $k+1_{th}$ and $k_{th}$ driving cycles respectively. If $\zeta$ is the set of all the cells $(i,j)$ such that $E(i,j)_{k+1} - E(i,j)_k \neq 0$, then we define the *cycle-to-cycle stroboscopic distance* as:

$$1 - Overlap_{strobo} = \frac{|\zeta|}{N \times N} . \tag{4.3}$$

Here, $|\zeta|$ is the cardinality of the set $\zeta$ and system size equals $N \times N$. The value of the function will become zero (or periodic for multi-period) with driving cycles once a limit cycle is found.

We now show the cycle-to-cycle count of plastic activity with number of driving cycles for a single realisation driven at the same cycling amplitude, $\gamma_{train} = 0.05$, during the training phase but before settling in a limit cycle. In the Figure 4.20, we see that $1 - Overlap_{strobo}$ during the first driving cycle is as high as 0.55 meaning that 55% of the $N \times N$ cells were active. This value quickly settles in a statistical steady state after first $\sim 10$ driving cycles. For driving cycles above 10, the evolution of spatial plastic activity with driving cycles seems like a random process whose statistical properties don't change with time and not indicating that the system is evolving towards a limit cycle. Such a behavior is in sharp contrast with the evolution of memory as shown in figure 4.19 which shows a slow decay towards the steady state value and gradual build-up of memory of training.

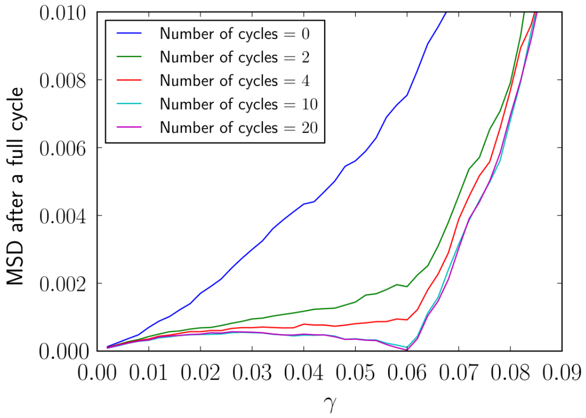

Fig. 4.21 Evolution of (single) memory of training: Mean squared displacement (MSD) versus $\gamma_{read}$ for different number of training cycles for a fixed value of $\gamma_{train} = 0.06$ below an appropriately defined irreversibility transition. Figure taken from reference [43]. MSD was calculated between the trained state and read state configurations obtained from a parallel read-out protocol as schematically demonstrated in Figure 4.1.

We point out that the question of evolution of memory of training amplitude has been probed in particle scale simulations of dense amorphous solids [43]. The authors used a training and read-out protocol same as schematically demonstrated in Figure 4.1. The training amplitude was set to $\gamma_{train} = 0.06$ which is below the amplitude corresponding to an irreversibility transition. For the purpose of revealing the memory of training amplitude, the authors computed the mean squared displacement (MSD) between trained state and read state at different values of read amplitudes $\gamma_{read}$. In Figure 4.21, we see that as the number of training cycle increases, a local minimum in the measured MSD emerges at $\gamma_{read} = \gamma_{train}$ for number of training cycles 10 and above. This reflects a memory of training amplitude. In this case, and when $\gamma_{read} < \gamma_{train}$, we also observe a non-monotonic response in the measured MSD.

### 4.6.2 Learning the direction of shear

As pointed out before, the training phase on the initial state can shear cycle at a given amplitude in two possible directions starting from zero strain. Our EPM predicts that the steady state holds memory of this direction of shear which can be revealed by performing read-out operations. We now show that the first shear cycle alone on the initial state is sufficient to encode memory of shear direction. We keep $\gamma_{train} = 0.05$ just as in section 4.6.1. In Figure 4.22 (Left), we plot the evolution of the stroboscopic distance versus $\gamma_{read}$ for a parallel out-phase read-out protocol at different values $\tau_{train}$. We see that the stroboscopic distance shows a weak dependence on $\tau_{train}$. To confirm that the memory of shear direction is established from the first training cycle onwards, we define a quantity called $\delta\langle\, 1 - Overlap\rangle_{\gamma_{read}=\gamma_{train}}$ as:

$$\delta\langle\, 1 - Overlap\rangle_{\gamma_{read}=\gamma_{train}} = \Big(\langle\, 1 - Overlap\rangle_{out\ phase} - \langle\, 1 - Overlap\rangle_{in\ phase}\Big)\Bigg|_{\gamma_{read}=\gamma_{train}} . \tag{4.4}$$

Here, $\delta\langle\, 1 - Overlap\rangle_{\gamma_{read}=\gamma_{train}}$ is the difference of the average stroboscopic distance of the out-phase and in-phase read-out protocol evaluated at $\gamma_{read} = \gamma_{train}$. In Figure 4.22 (Right), we show $\delta\langle\, 1 - Overlap\rangle_{\gamma_{read}=\gamma_{train}}$ versus $\tau_{train}$. We observe that the value of this function is non-zero from the first shear cycle onwards. This means that a single shear cycle on the initial undeformed state is sufficient to encode the memory of shear direction which can be read by evaluating the response under an in-phase or out-phase read-out protocol.

### 4.6.3 Memory under asymmetric shear and return point memory

In this section, we will study memory of training under asymmetric shear and use it to establish whether our model of sheared amorphous solids displays return point memory. The training and read-out protocol has been described in figure 4.23. The initial undeformed sample is first trained asymmetrically such that a single cycle in shear of amplitude $\gamma_{train}$ is of the following

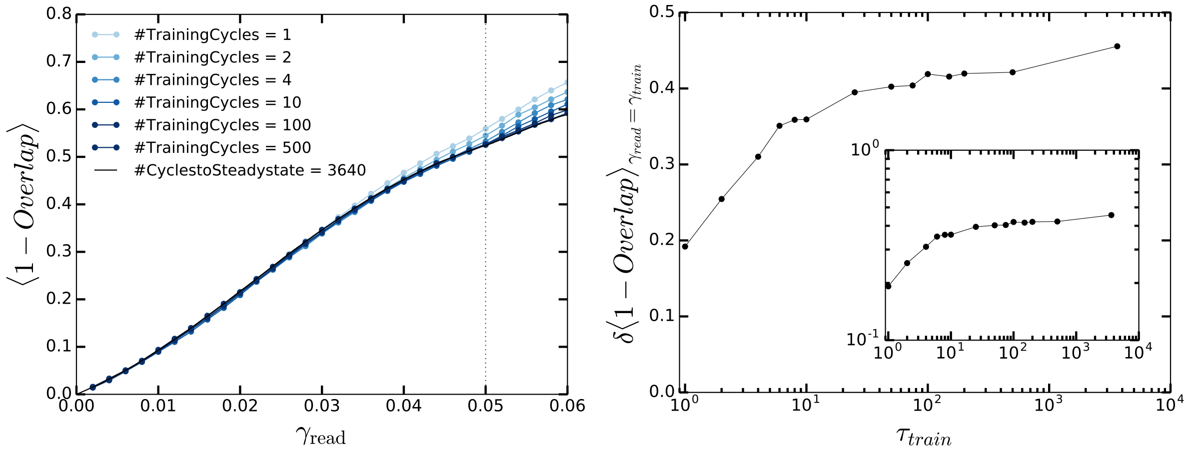

Fig. 4.22 (Left) Evolution of (single) memory of training: stroboscopic distance versus $\gamma_{read}$ for different number of training cycles for a fixed value of $\gamma_{train}$ for out-phase read-out. Dotted vertical line on the $\gamma_{train}$-axis represents the value of the training amplitude. System size $= 32 \times 32$, poorly aged (PA) samples. (Right) On a Lin-Log scale: Difference of the average stroboscopic distance between the out-phase and in-phase read-out protocol evaluated at $\gamma_{read} = \gamma_{train}$ versus $\tau_{train}$. Inset: Same plot as in the main panel showed on Log-Log scale.

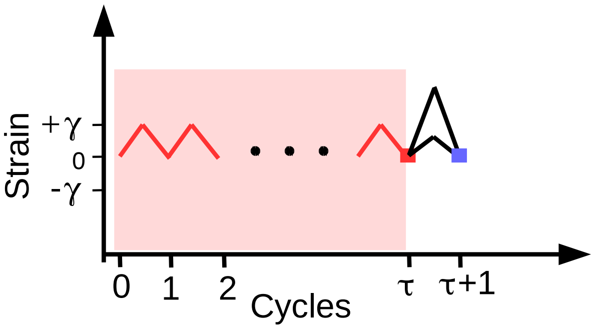

Fig. 4.23 Training and read-out protocol under asymmetric shear: The training phase constitutes of individual cycles of the following form in strain $0 \rightarrow \gamma_{train} \rightarrow 0$. The training phase drives the system to a trained state belonging to a limit cycle. The trained state is marked as red square symbol. The read-out phase consists of making multiple copies of the trained state and then each copy is sheared at different amplitude with asymmetric shear cycles of the form $0 \rightarrow \gamma_{read} \rightarrow 0$ ending in a read state shown in blue square symbol. Read-states and trained states are compared using the same definition of stroboscopic distance as in equation 4.1.

form in strain: $0 \rightarrow \gamma_{train} \rightarrow 0$. The maximum training amplitude considered for studies in this section is $\gamma_{train} = 0.06$ at a system size $16 \times 16$. The choice of training amplitude ensures that the probability of finding limit cycles is one and only period one limit cycles exist in the trained state. This helps our study to make comparisons on return point memory. The read protocol makes multiple copies of the trained state and which are then sheared at different read amplitudes $\gamma_{read}$ sweeping across the training amplitude to test a memory of the training amplitude. A shear cycle during the read-out phase is also asymmetric and such that a single read cycle at amplitude $\gamma_{read}$ is of the following form in strain: $0 \to \gamma_{read} \to 0$. All results in this section have been obtained by averaging over 400 independent realizations. The values of training amplitude $\gamma_{train}$ considered are such that $\gamma_{train} < \gamma_{irr}$, where $\gamma_{irr}$ was quantified and discussed in Chapter 3.

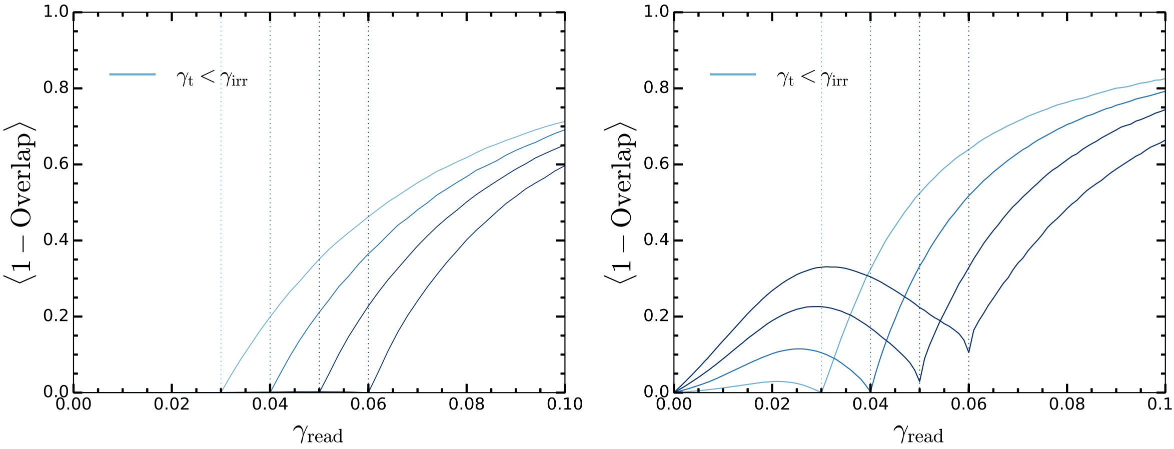

Fig. 4.24 Memory of training amplitude under (Left) Asymmetric training and read-out and for comparison; (Right) Symmetric training and read-out for the same values of training amplitude. Dashed vertical lines correspond to $\gamma_{read} = \gamma_{train}$. System size equals $16 \times 16$.

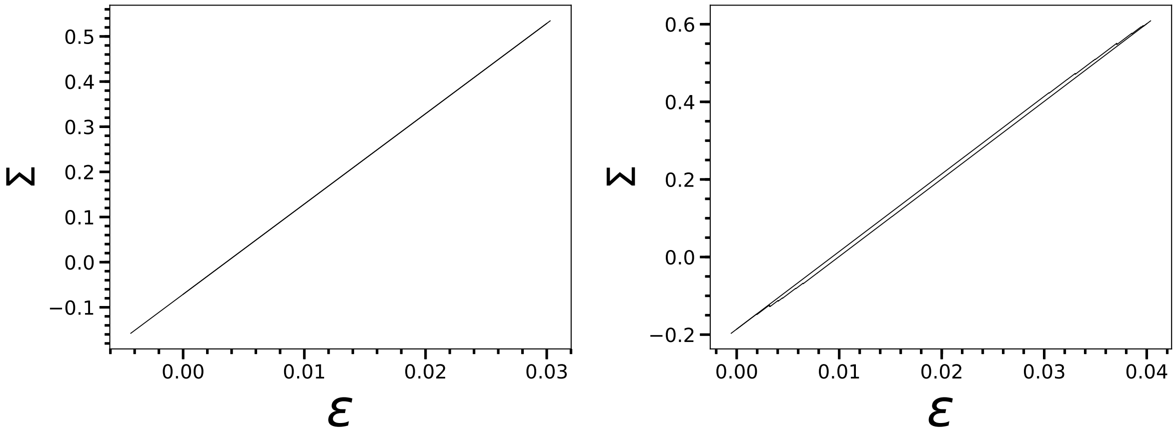

Fig. 4.25 A typical limit cycle under a shear cycle $0 \to \gamma_{train} \to 0$ for (Left) $\gamma_{train} = 0.03$ and (Right) $\gamma_{train} = 0.04$

The training protocol helps the system settle in a trained state belonging to a limit cycle under asymmetric shear. A read-out protocol on the trained state as discussed above becomes a test on return point memory. For a given training amplitude $\gamma_1$ and any $\gamma_{read} \leq \gamma_1$, if the read-state and trained-state are not identical then this implies a violation of return point memory.

In figure 4.24 (Left), we show the memory of training amplitude for the training and read-out protocol demonstrated in figure 4.23. We see that the stroboscopic distance remains seemingly zero for $\gamma_{read} \leq \gamma_{train}$ beyond which it rises rapidly and monotonically. This seems to suggest that sheared amorphous solids obey return point memory. To contrast this observation against results from previous sections, for the same values of $\gamma_{train}$ under a training and read-out that use symmetric shear cycles only, we show in figure 4.24 (Right), the response is completely different. We point out that such a contrasting response in memory under symmetric and asymmetric response is due to the fact that the range in strain over which limit cycles are found under asymmetric shear is larger than their symmetric shear counterpart so that an irreversibility transition is delayed. For example, for system size $16 \times 16$, at driving amplitude $\gamma_{train} = 0.0699$ the system is at irreversibility transition under symmetric shear while it finds limit cycles with probability one with almost all periods eqaul to one under asymmetric shear till this amplitude.

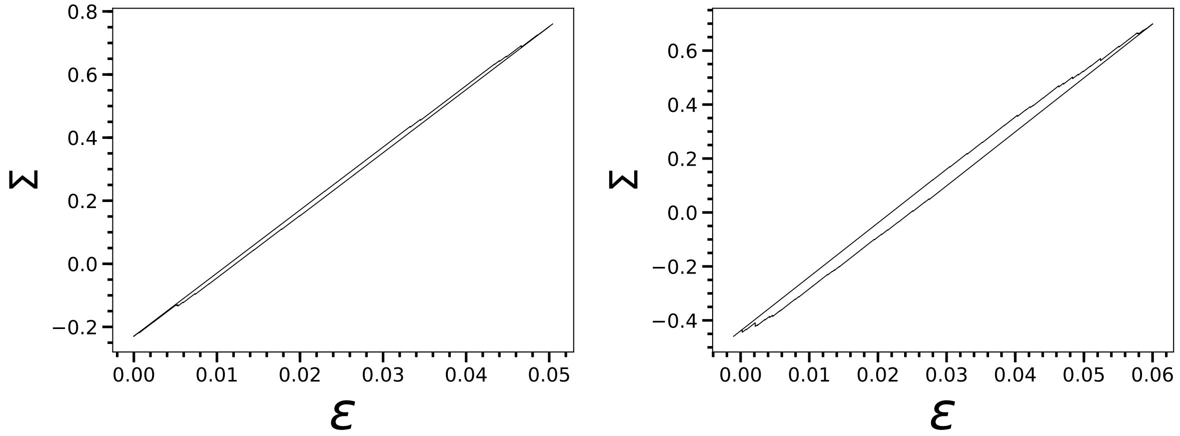

Fig. 4.26 A typical limit cycle under a shear cycle $0 \rightarrow \gamma_{train} \rightarrow 0$ for (Left) $\gamma_{train} = 0.05$ and (Right) $\gamma_{train} = 0.06$

Figure 4.24 (Left) suggests that the stroboscopic distance is zero for $\gamma_{read} \leq \gamma_{train}$. We will now confirm that such a behavior indeed arises even when the limit cycles are hysteretic composed of plastic events. Figure 4.25 (Left) and (Right) show limit cycles obtained at $\gamma_{train} = 0.03$ and $0.04$, respectively. Figure 4.26 (Left) and (Right) show limit cycles obtained at $\gamma_{train} = 0.05$ and $0.06$, respectively. We have checked that the general behavior of limit cycles at these amplitudes is hysteretic and therefore observation of the stroboscopic distance falling to zero for $\gamma_{read} \leq \gamma_{train}$ is a non-trivial behaviour suggesting RPM.

As a further test, we show figure 4.24 (Left) plotted on a Log-Lin scale in figure 4.27. We see that the stroboscopic distance is not perfectly zero for $\gamma_{read} \leq \gamma_{train}$ as would have been required by a strict RPM. Also, the maximum of the stroboscopic distance over $\gamma_{read} \leq \gamma_{train}$ seems to increase slowly with $\gamma_{train}$. Nevertheless, for the values of $\gamma_{train}$ considered, we see clearly hysteretic behaviour in the limit cycles and yet a value of the stroboscopic distance that

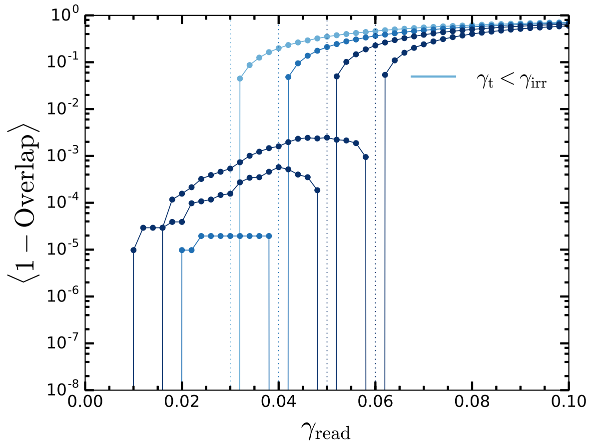

Fig. 4.27 Data same as in figure 4.24 (Left) such that y-axis is on a logarithmic scale, and a linear scale on the x-axis. Data points at $\gamma_{read} = \gamma_{train}$ drop to zero on Log y-scale. The immediate neighbors of such data points are finite and their difference on the $\gamma_{read}$-axis is not very fine. This is why the data may seem diconnected around $\gamma_{read} = \gamma_{train}$.

is nearly zero suggesting that the RPM is held by the system, if not perfectly. This means that soft-spots which are active within such a limit cycle could show correlated behavior underlining effectively cooperative interactions even though the interaction kernel used in our model is of the Eshelby type. This remains to be checked.

## 4.7 Multiple memories

This section is inspired by the question if driven disordered systems, and glassy amorphous systems in particular, could be trained such that memory be added without erasing another.

Before we proceed further on our discussion of multiple memories it is useful to remind the reader of the concept of return point memory (RPM) which was introduced in Chapter 1. It will help us understand the consequences of our results against systems guaranteed to hold RPM which are at odds with amorphous solids.

Disordered systems, with many interacting degrees of freedom, can be trained through external driving to encode memories of multiple training amplitude [59]. Examples include systems ranging from ferromagnets [10, 97, 113], spin ice [35, 45], to high temperature superconductors [89]. Interactions between individual elements of these systems are cooperative meaning that a local state change encourages other elements to change their state in the same direction. A simple example is the well-studied Random Field Ising Model (RFIM) for ferromagnets in which the the individual spin sites could either take a +1 or -1 state. The mmodel uses cooperative interactions meaning that a spin flip to +1 state encourages others to do so. Systems with such kind of interactions were proven to hold return point memory [113] (RPM). RPM allows a system to remember a nested series of turning points in the externally applied driving field thus permitting the storage of multiple amplitudes of training [59]. The nesting of turning points in the external field implies that there is a constraint on the order in which these turning points can be arranged. Storage of multiple amplitudes thus demand that such a constraint on the ordering of turning points be satisfied.

Experiments [55, 77] and particle scale simulations of amorphous solids [1], with interactions known to violate RPM, have shown that an RPM obeying ordering of turning points on driving shear strain can still generate a trained state holding memories of multiple amplitudes of training. As an example, we show Figure 4.28 from reference [1] showing memories of multiple amplitudes of training obtained from particle scale simulations for a model amorphous solid. The training phase in their simulations is the same as in Figure 4.3. They used a parallel read-out protocol same as discussed in Section 4.2.2 with the only difference that they use mean squared displacement (MSD) of the particles instead of using event fields to uncover the memory of training amplitude. We note that, although it is possible to derive an MSD based on coarse-grained quantities in our elasto-plastic model, we restrict our measurements on memory using event fields only. Figure 4.28 shows that their particle scale model encodes memories of two amplitudes $\gamma_2 = 0.06$ and $\gamma_1 = 0.04$ in the trained state which is revealed after performing the read-out phase. The memory of training amplitude is reflected through the MSD at $\gamma_{read} = \gamma_{train}$ for the smaller training amplitude of 0.04 which drops to zero while a sharp kink is observed at the larger value of the training amplitude 0.06 at which the MSD is not zero but finite. Two large but different number of training cycles were considered to highlight the fact that steady state can encode multiple memories and hence conclude that multiple memories in amorphous solids are persistent. In this section we will first show that our EPM can capture such an effect.

To demonstrate that our elasto-plastic model can display memories of multiple amplitudes of training, we consider two training amplitudes $\gamma_1$ and $\gamma_2$. Let these be such that $\gamma_2 > \gamma_1$. The training sequence is same as discussed in Section 4.2.2 and described in the figure 4.3. We recall that the training sequence in the amplitude form is the following: $\gamma_2\gamma_1\gamma_2\gamma_1\gamma_2\gamma_1..$ . For small to moderate values of $\gamma_2$, the training sequence results in a state belonging to a limit cycle. As $\gamma_2$ increases the probability of finding limit cycles decreases. We note again that, though multiple training amplitudes are present, a single cycle of shear at an amplitude $\gamma$ is still defined as: $0 \rightarrow \gamma \rightarrow -\gamma \rightarrow 0$.

Let us say that we have been given a pair of training amplitudes $\gamma_1$ and $\gamma_2$. We consider two types of averaging of the stroboscopic distance while plotting against $\gamma_{read}$. In the first case, we average over those trained states only for which the amplitude of the last applied cycle in the training sequence was $\gamma_1$. In the second case, the average is over those trained states for which the last applied cycle in the training sequence was $\gamma_2$. We plot the stroboscopic distance versus $\gamma_{read}$ separately for the two types of averaging. In the figure 4.29, we have considered

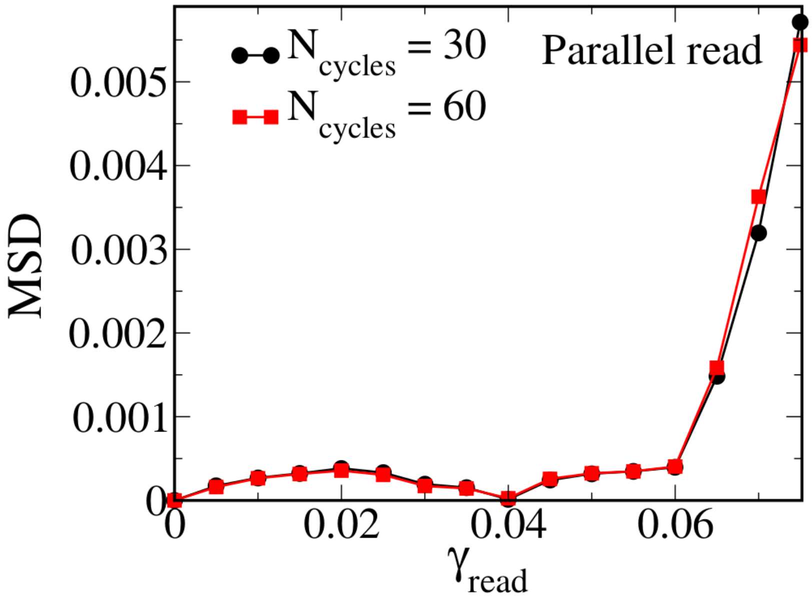

Fig. 4.28 Mean squared displacement of particles trained at multiple amplitudes versus strain amplitude during read-out in particle scale simulations. Training and read-out protocols are the same as in Figure 4.3. Training amplitudes are: $\gamma_2 = 0.06$ and $\gamma_1 = 0.04$. Legends indicate number of driving cycles performed to reach the trained state. Figure adapted from reference [1].

$\gamma_2 = 0.038$ and $\gamma_1 = 0.028$ and see striking differences between the conditional averages. We observe that an averaging that is performed over samples for which the last applied shear cycle is $\gamma_2$, the memory of the smaller training amplitude is absent. However, a memory of $\gamma_2$ is clearly present as a sharp local minimum which drops to zero at $\gamma_{read} = \gamma_2$. In fact, the response strikingly resembles curves obtained for training that uses single amplitudes only. Contrastingly, if the average is performed over those samples only for which the last applied training cycle had an amplitude $\gamma_1$, we observe memories of both the training amplitudes $\gamma_1$ and $\gamma_2$. The memory of $\gamma_1$ is revealed as a sharp local minimum dropping to zero at $\gamma_{read} = \gamma_1$ and the memory of $\gamma_2$ appears as a sharp kink at $\gamma_{read} = \gamma_2$. Solid and dashed vertical lines in black are plotted at $\gamma_{read} = \gamma_1$ and $\gamma_{read} = \gamma_2$, respectively. Such memories of multiple amplitudes of training have been observed in experiments recently [55, 56].

We now show that multi-period orbits do not impede memories of multiple training amplitudes, that is, $\gamma_1$ and $\gamma_2$. For this purpose, we consider $\gamma_2 = 0.05$ and $\gamma_1 = 0.04$. At these values of $\gamma_1$ and $\gamma_2$, all the samples find limit cycle but a fraction of them admit multi-period limit cycles. In the figure 4.30, we see that depending on the amplitude of the last applied training cycle we can either only have the memory of the larger amplitude $\gamma_2$ or both $\gamma_1$ and $\gamma_2$. However, we observe that the effect of multi-periodicity is to shift the value of the local

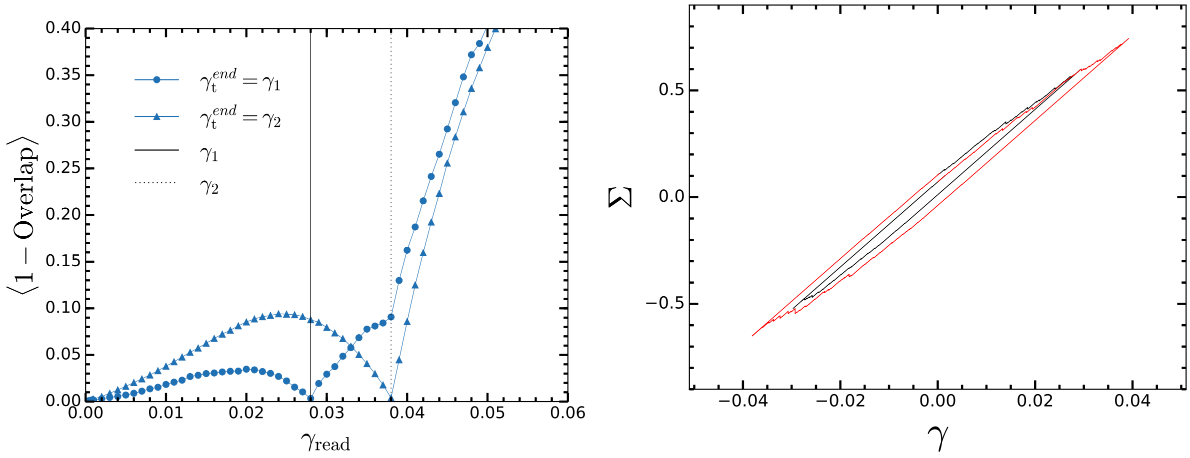

Fig. 4.29 Memory of multiple amplitudes: (Left) stroboscopic distance versus $\gamma_{read}$ for a parallel read-out protocol. Curve with ▲ symbol was obtained by averaging over trained states for which the last applied training amplitude was $\gamma_2$ ($< \gamma_1$). Curve with ● symbol was obtained by averaging over trained states for which the last applied training amplitude was $\gamma_1$. Solid and Dotted vertical lines on the $\gamma_{train}$-axis represent the training amplitudes $\gamma_1$ and $\gamma_2$ respectively. (Right) A limit cycle from a particular realization obtained under variable amplitude driving for the same pair of amplitudes $\gamma_1$ and $\gamma_2$ as in the left. System size = $16 \times 16$, poorly aged (PA) samples.

minimum in the stroboscopic distance at $\gamma_{read} = \gamma_1$ to higher value and similarly in the kink at $\gamma_{read} = \gamma_2$ without affecting the memories of training.

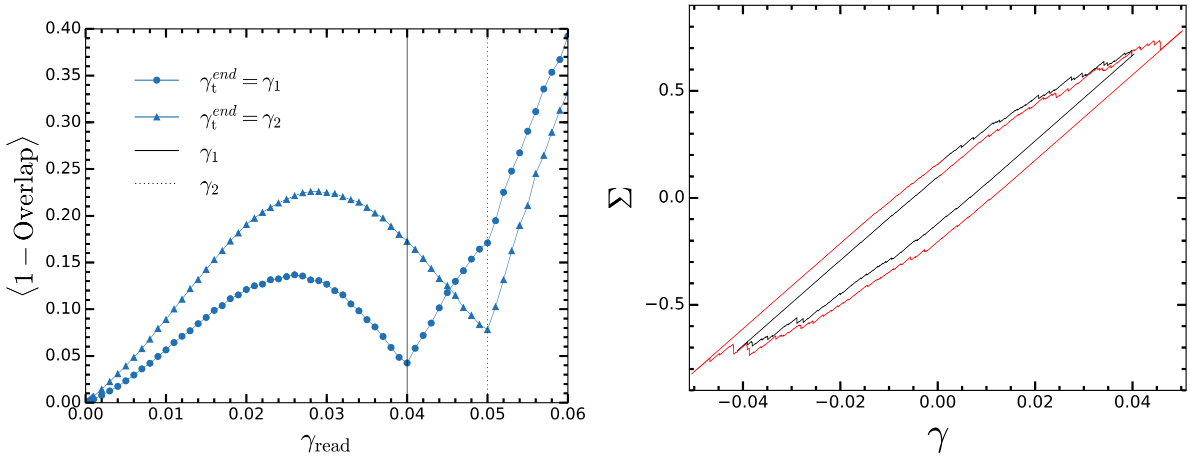

Fig. 4.30 Memory of multiple amplitudes: (Left) stroboscopic distance versus $\gamma_{read}$ for a parallel read-out protocol. Curve with ▲ symbol was obtained by averaging over trained states for which the last applied training amplitude was $\gamma_2$ ($< \gamma_1$). Curve with ● symbol was obtained by averaging over trained states for which the last applied training amplitude was $\gamma_1$. Solid and Dotted vertical lines on the $\gamma_{train}$-axis represent the training amplitudes $\gamma_1$ and $\gamma_2$ respectively. (Right) A limit cycle from a particular realization obtained under variable amplitude driving for the same pair of amplitudes $\gamma_1$ and $\gamma_2$ as in the left. System size = $16 \times 16$, poorly aged (PA) samples.

Finally, we present the effect of increasing the amplitude of training on storage of multiple memories. For $\gamma_{irr} > \gamma_2 > \gamma_1$, a read-out on the trained state preserves memories of both training amplitudes $\gamma_1$ and $\gamma_2$. We note here that $\gamma_{irr}$, as defined and discussed in Chapter 3, is the training amplitude which marks the irreversibility transition based on shear driving at single amplitude of training. To study the effect of increasing training amplitude for the case when multiple memories can be stored, we consider the following pairs of $(\gamma_1, \gamma_2)$ in the figure 4.31: (0.03,0.04), (0.04,0.05), (0.05,0.06), (0.06,0.07). We note that $\gamma_{irr} = 0.07$. In the figure 4.31, we see that for the training amplitude pair (0.03,0.04) the memory of smaller amplitude $\gamma_1$ shows in stroboscopic distance by dropping to zero while the memory of larger amplitude $\gamma_2$ appears as a kink at finite value at the respective values of the read amplitudes. As we increase the values of the amplitude pair, memory of both $\gamma_2$ and $\gamma_1$ is preserved but only shifts to higher values of the stroboscopic distance. For the amplitude pair (0.06,0.07) however, we observe that the memory of larger amplitude, expected as a kink at $\gamma_{read} = 0.07$, is absent while the memory of the smaller amplitude is still present.

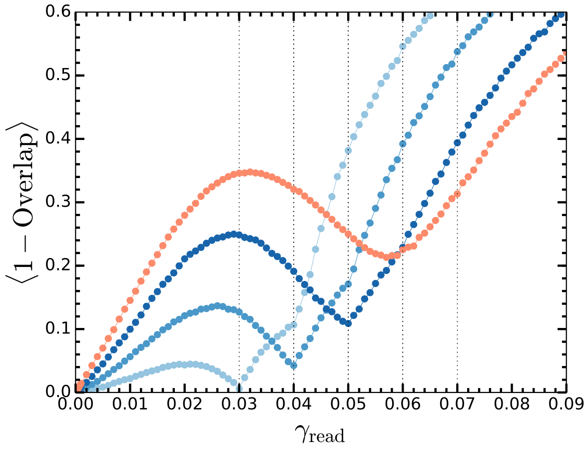

Fig. 4.31 Memory of multiple amplitudes: stroboscopic distance versus $\gamma_{read}$ under parallel read-out protocol for different pairs of training amplitudes $(\gamma_1, \gamma_2)$: (0.03,0.04), (0.04,0.05), (0.05,0.06), (0.06,0.07). System size = $16 \times 16$, poorly aged (PA) samples.

## Discussion

Our elastoplastic model shows that memories of multiple training amplitudes can be encoded provided an ordering is respected in the sequence of applied amplitude leading to a trained state. In figure 4.29, for a given value of $\gamma_{read}$, we see that the stroboscopic distance between the trained state and the read state can be significantly different when $\gamma_{read} < \gamma_1$. In particular, when memories of both $\gamma_1$ and $\gamma_2$ are present the stroboscopic distance between the trained state and the read state is significantly smaller than when only the memory of the larger amplitude $\gamma_2$

is present. This implies that the spatial plastic activity due to avalanches over a full read cycle is significantly less when the trained state is holding memories of multiple training amplitudes. This raises the question whether the set of active sites for the case when multiple memories are present are only a subset of active sites when only the memory of largest training amplitude survives. Presence of memories of multiple training amplitudes could then imply correlations among the active soft spots during read cycles on the trained state. Such correlations can highlight the possibility whether the nature of interactions among the active soft-spots inside a limit cycle could be ferromagnetic (or anti-ferromagnetic) alone.

### 4.7.1 Effect of mechanical annealing

Non-interacting [97] or systems with ferromagnetic interactions [10, 113] can be trained using single shear cycles to encode memory of the training amplitude. For these systems it has also been observed that the memory of training amplitude can be erased using single shear cycles if the amplitude is greater than the training amplitude while also establishing memory of the larger amplitude. For the case when the shear cycle has an amplitude smaller than the training amplitude, memories of both amplitudes can be recovered. Here we ask using our EPM if training at a single amplitude produces a trained state amenable to encoding memory using single shear cycles alone? This also help us understand memory formation in driven amorphous materials against non-interacting/ferromagnetically interacting systems. Training and read-out protocols are defined in the Figure 4.32.

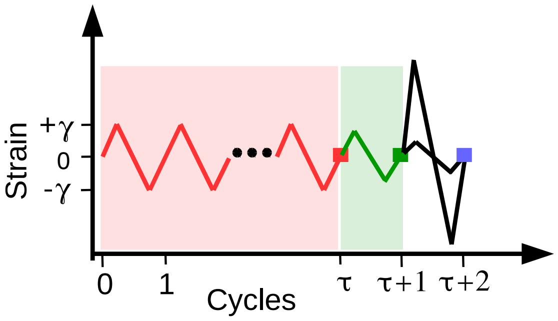

Fig. 4.32 Training, perturbing and reading memory of training: Training cycles (solid line in red) beginning from the undeformed state at zero strain at fixed amplitude $\gamma_{train}$ lead to a trained state (red square symbol). The trained state is then subjected to a single perturbation shear cycle (solid line in green) leading to a perturbed state (green square symbol). Read out phase begins with making multiple copies of the same perturbed state. Each copy is then subjected to a single cycle of strain (solid line in black) at different strain amplitude $\gamma_{read}$ ending in a read state (blue square symbol). Read state in blue symbol is compared to the perturbed state in green symbol to reveal the effect of perturbation on the trained state.

As demonstrated in Figure 4.32, the training phase consists of shear driving the initial undeformed state at a single training amplitude $\gamma_{train}$ for a maximum of $10^4$ cycles to reach a trained state. We then subject the trained state to a single cycle of shear at an amplitude $\gamma_{perturb}$ ending in a perturbed state. The perturbed state is then subjected to a parallel read-out protocol to evaluate if the perturbed state holds memory of $\gamma_{perturb}$. Additionally, the read-out protocol on the perturbed state also serves to determine if a single perturbation cycle can eliminate memory of $\gamma_{train}$. In our simulations the training amplitude $\gamma_{train}$ varies from 0.03 to 0.044, while the perturbation amplitude $\gamma_{perturb}$ is kept fixed at 0.04. This allows us to set up our study at perturbation amplitudes both below and above the training amplitude. In Figure 4.33, we first consider the case when $\gamma_{perturb} < \gamma_{train}$. These correspond to the training amplitudes $\gamma_{train} = 0.042$ and $\gamma_{train} = 0.044$ as also shown in the legend. At these values we see that a single perturbation cycle is sufficient to encode memory of $\gamma_{perturb}$ which appears as a sharp local minimum at $\gamma_{read} = \gamma_{perturb}$. We also note that the memory of training amplitude is retained in the perturbed state as seen as a kink in the stroboscopic distance at $\gamma_{read} = \gamma_{train}$. Next, we consider $\gamma_{perturb} > \gamma_{train}$ which correspond to the training amplitudes $\gamma_{train} = 0.030$ and $\gamma_{train} = 0.035$ shown in the legend of the figure. Interestingly, we observe the absence of a local minimum in the stroboscopic distance at $\gamma_{read} = \gamma_{train}$ implying that a single perturbation cycle has erased the memory of training amplitude $\gamma_{train}$. We also observe that the memory of perturbation amplitude $\gamma_{perturb}$ has not been established either, as the cusp (if any) in the stroboscopic distance appears at $\gamma_{read} < \gamma_{perturb}$. To summarise figure 4.33, when $\gamma_{perturb} < \gamma_{train}$, single shear cycles alone, of amplitude $\gamma_{perturb}$, acting on the trained state can encode memory of $\gamma_{perturb}$ while also retaining memory of $\gamma_{train}$. Contrastingly, when $\gamma_{perturb} > \gamma_{train}$ single cycles of shear perturbation erase memory of training amplitude $\gamma_{train}$ but also do not encode memory of $\gamma_{perturb}$.

### Discussion

We now make some final comparisons of our results in figure 4.33 against hysteron based non-interacting and interacting systems built to study memory in driven disordered systems. Non-interacting or systems with ferromagnetic interactions take at most one training cycle to find a limit cycle and it is probably therefore not surprising that the memory of training can be erased completely using single cycles of shear perturbation with amplitude greater than the training amplitude. Our EPM is built on interactions that are not purely ferromagnetic and can display long transients to limit cycles. Erasing memory of training amplitude with single shear cycle alone is therefore an interesting observation in figure 4.33. It has been shown that when $\gamma_{perturb} > \gamma_{train}$ (represented schematically in figure 4.32) in non-interacting/ferromagnetically interacting system, the memory of perturbation amplitude $\gamma_{perturb}$ is encoded immediately, that is, in single shear cycle alone which is also in contrast to what we observe in figure 4.33. Finally,

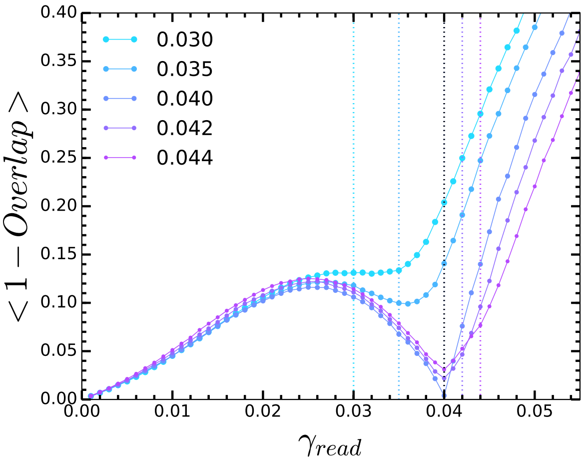

Fig. 4.33 Robustness of single memory of training amplitude: stroboscopic distance versus $\gamma_{read}$ for different values of training amplitude. Dotted vertical lines on the $\gamma_{read}$ - axis represent, in the same color, the corresponding value of the training amplitude $\gamma_{train}$ which are also marked in the legend. The black dashed line represents $\gamma_{perturb}$ on the $\gamma_{read}$ - axis. System size $=$ 32×32, poorly aged (PA) samples.

in contrast to our observations in figure 4.33, hysteron-based models [72] with mean-field interactions show that when $\gamma_{perturb} > \gamma_{train}$, memory of $\gamma_{perturb}$ can be encoded using single cycles alone. We therefore conclude that the nature of mean-field interactions as in reference [72] could also be overestimating the tendency of memory formation. Such differences with respect to our results could be due to the nature of interaction present in our Eshelby kernel.

We also observe that first shear cycle in the training phase, as in the figure 4.19 (Left), cannot encode the memory of training amplitude. Such a behavior is in sharp contrast to samples that have been trained to a steady state at a given training amplitude. Such a steady state, as observed in Figure 4.33, can encode memory of driving amplitude in single cycle of shear if the imposed amplitude is lower than the training amplitude. Our EPM thus also helps us conclude that an undeformed glass sample can have strikingly different affinity towards learning a given amplitude of shear cycle than a glass sample which has already been trained mechanically.

## 4.8 Conclusion

In this chapter, we have shown that our EPM can capture memory of training as observed in cyclically sheared amorphous systems in experiments and particle scale simulations. For the case when such solids are shear driven at a single amplitude to trained state, a read-out protocol on the trained state can reveal the value of the training amplitude. Our EPM captures such an effect succesfully. Using a range of training amplitudes, from small to large, we see that the memory of training can persist even past the irreversibility transition depending on the read-out protocol. The quality of memory, as measured in the sharpness of the average stroboscopic distance at $\gamma_{read} = \gamma_{train}$, does degrade however with increasing amplitude of training past the irreversibility transition. Our results also show that the memory of the training amplitude can also be revealed through sample to sample fluctuations in the stroboscopic distance during the read-out phase. We also showed that the trained state alone, in the absence of a read-out protocol, can reveal memory of training amplitude in the distributions of the distance to local stress thresholds. By looking at the evolution of memory of training amplitude with number of training cycles, we also concluded that the memory of the training amplitude can be encoded well before reaching the steady state. This means that one does not have to cycle an amorphous solid for a large number of driving cycles, especially in the vicinity of the irreversibility transition, to encode memory of training amplitude.

Our results also demonstrate that cyclically driven amorphous systems can encode the memory of direction of shear. A read-out under cyclic shear with increasing amplitude, sweeping past the training amplitude, reveals contrastingly different responses depending on the relative phase with the training sequence. This serves as a tool to decipher the direction in which a sample was trained. We also observe that such memories persist past the irreversibility transition irrespective of the read-out protocol used. We have also demonstrated that the memory of shear direction is encoded from the first cycle onwards.

Depending on the ordering of training amplitudes amorphous solids can remember multiple amplitudes of training. Our EPM also displays this effect. We show that a training sequence that encodes multiple memories can be manipulated to either erase or recover training amplitudes by altering the state on which a read-out cycle is performed. These alterations in our discussions are nothing but those that generate trained states that are one shear cycle apart. Erasure/recovery of training amplitudes based on single cycles of shear is a property shared by systems with ferromagnetic/no interactions. However, we observe such an effect even with interactions that are not purely ferromagnetic as encoded in the Eshelby stresses generated post local yield events. We wonder if such discrepancies arising from the long transients that system takes to settle into limit cycles. Such an observation is not dissimilar to a recent ring-down training protocol [56] in experiments that can help find an amorphous solid settle in a state such that single training cycles alone are sufficient to encode the memory of training. Finally, we showed that memories of multiple training amplitudes can be encoded even if the trained state belongs to multi-periodic limit cycles. We also studied the effect of increasing the amplitude of training for the multiple memory case.

We also studied the effect of prior training on further encoding of memories of training amplitude. We concluded that a sample that is trained to a steady state at an amplitude $\gamma_{train}$ can encode memory of shear cycles of amplitude less than $\gamma_{train}$ using single cycles only. Prior training under cycling thus makes a disordered glassy solid more amenable to storing memory of training amplitude. We also showed that single shear cycles on the trained state are unable to encode memory for amplitudes greater than $\gamma_{train}$. We also discussed these results in light of non-interacting/ferromagnetically interacting systems but also those which use mean-field interactions in hysteron based models for disordered materials.

# Chapter 5

# Characterization of the disorder landscape via transition graphs

In order to characterize better the disorder landscape underlying our mesoscopic model, we turn next to the transition graph ($t$-graph) representation of the dynamics under AQS shear [75]. As was shown recently [78, 101], such $t$-graphs can be extracted from atomistic simulations of sheared amorphous solids. Features of the AQS dynamics, such as yielding and return point memory, are thereby encoded in the topology of the $t$-graph [78, 79, 101]. Thus $t$-graphs provide useful information about the underlying disorder landscape. At the same time, the representation of AQS dynamics via $t$-graphs extracted from simulations provides a unified framework within which we can compare the dynamics of atomistic as well as mesoscopic models in a rather direct and comprehensive manner.

## 5.1 AQS transition graphs

To fix ideas, we consider first the sheared amorphous solid in an atomistic setting. Under AQS conditions, a given mechanically stable particle configuration can be sheared in the positive and negative direction until a mechanical instability occurs. Denoting by $\epsilon^{\pm}$ the critical values of the external shear strain at which the instability sets in, for shear strains between $\epsilon^{-}$ and $\epsilon^{+}$, the configuration of particles deforms smoothly and reversibly in response to the applied shear strain. These sets of mechanically stable particle configurations constitute an elastic branch of the system which we simply refer to as a *mesostate* [78]. We will use capital letters to label mesostates, and denote the critical strain values of a mesostate $A$ by $\epsilon^{\pm}[A]$. When $\epsilon = \epsilon^{+}[A]$ (or $\epsilon = \epsilon^{-}[A]$), a fast relaxation to a new mechanically stable particle configuration occurs. This particle configuration must necessarily be part of another mesostate, i.e. belong to a different elastic branch, say $B$. Thus the instability at $\epsilon = \epsilon^{+}[A]$ triggers a transition from mesostate $A$ to $B$. A similar transition occurs when $\epsilon = \epsilon^{-}[A]$. The transition between mesostates can therefore

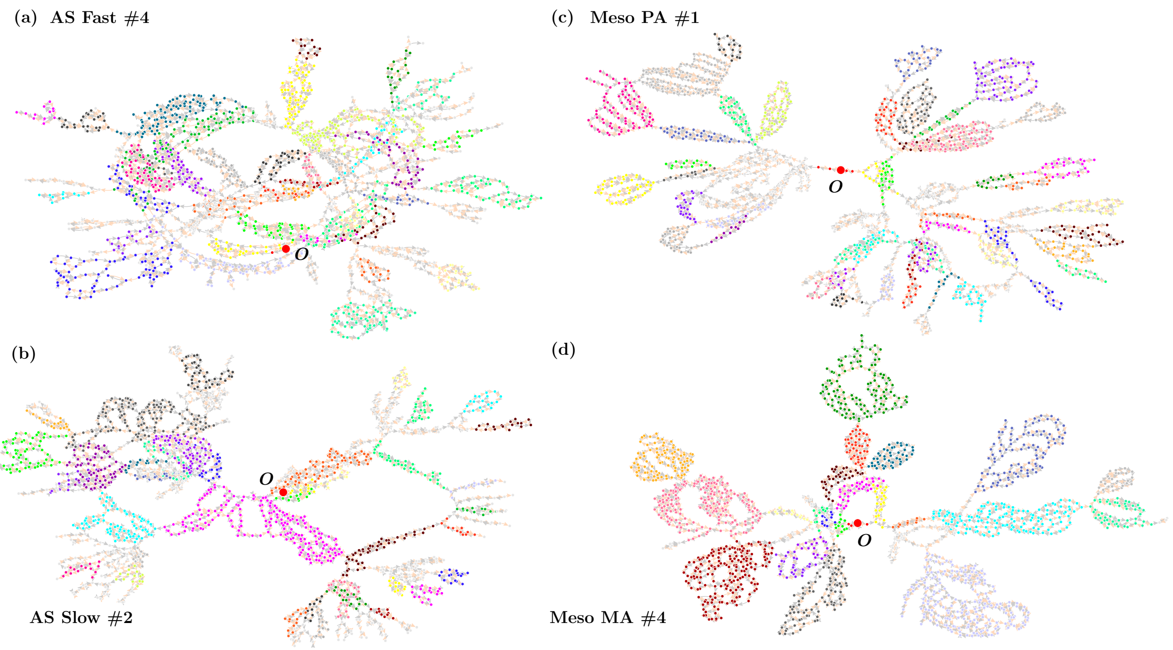

Fig. 5.1 Transition-graph representation of the AQS dynamics and thermal history – atomistic (AS) *vs* mesoscopic (Meso) models. Excerpts of transition graphs extracted from atomistic (a,b) and $N = 32$ mesoscopic glasses (c,d) with different thermal histories: (a,c) poorly-aged/fast quenched, (b,d) moderately aged/slow quenched. The color of each vertex indicates the strongly connected component (SCC) of the graph that it belongs to (refer to text for details) and the initial mesostate of the prepared glass has been marked with a larger red vertex labeled **O**. Vertices belonging to SCCs of size less than 10 have been colored in light gray.

be represented in terms of a directed graph, the AQS transition graph or simply $t$-graph. The vertices of the $t$-graph are the mesostates, while from each mesostate we have two outgoing transitions which constitute the directed edges of the graph. We shall denote the transitions when $\epsilon = \epsilon^{+}[A]$ or $\epsilon = \epsilon^{-}[A]$ as the **U**-, respectively, **D**-transition out of $A$. We will refer to the states that these transitions lead to as $\mathbf{U}A$ and $\mathbf{D}A$.

The $t$-graph along with the critical strains $\epsilon^{\pm}[A]$ associated with each mesostate forms a complete representation of the AQS dynamics under arbitrary shearing protocols [79]. Given an initial mesostate $A$ and a shear protocol, the sequence of mesostates visited can be read off by following the corresponding **U**- and **D**-edges, while checking each time whether the critical strains needed to trigger the transition have been exceeded or not. Note that since $\mathbf{U}A$ and $\mathbf{D}A$ are mesostates reached from $A$, their stability ranges must contain the strains $\epsilon^{\pm}[A]$ at which these transitions were triggered, i.e. we have the AQS conditions [79] :

$$\begin{aligned}\epsilon^-[\mathbf{D}A] < \epsilon^-[A] < \epsilon^+[\mathbf{D}A],\\ \epsilon^-[\mathbf{U}A] < \epsilon^+[A] < \epsilon^+[\mathbf{U}A].\end{aligned} \tag{5.1}$$

It follows that $\epsilon^+[A] < \epsilon^+[\mathbf{U}A] < \epsilon^+[\mathbf{U}^2 A] < \ldots$ and thus the upper critical strains are monotonously increasing with repeated **U**-transitions. An analogous result holds for the lower strain threshold under **D**-transitions. An immediate consequence of this observation is that the sub $t$-graphs, which are obtained by considering only transitions under **U** (or **D**), are necessarily acylic, i.e. they cannot contain any cycles. Thus any cyclic behavior must arise from an interplay of the **U**- and **D**-transitions.

## 5.2 Catalog acquisition and $t$-graphs from simulations

The numerical algorithm of extracting $t$-graphs from simulations of sheared amorphous solids has been described in detail in the supplementary material of Ref. [78]. Here we will sketch out the main idea. We start with an initial configuration that is part of a mesostate $O$ which we call the reference state. We assign to $O$ the generation number $g = 0$. Next, we execute the **U**- and **D**-mesostate transitions out of $O$, leading to the mesostates $\mathbf{U}O$ and $\mathbf{D}O$, and we assign these to generation $g = 1$. Everytime we reach a new mesostate, we compare it to the catalog of mesostates we have obtained so far to see whether it has been encountered before. If not, we add it to our catalog. By proceeding generation by generation, we acquire in this manner a catalog of mesostates: each mesostate $A$ is assigned an ID, its critical strains $\epsilon^{\pm}[A]$ and the IDs of the mesostates it transits into under a **U**- or **D**-transitions are determined. The $t$-graph is then assembled from such catalogs. In our mesoscopic models, each mesostate corresponds to a configuration of the local elastic branches associated with each of the cells. The event based nature of their simulations facilitates the identification of mesostates and their transitions.

We obtain catalogs from 10 realizations each of the $N = 32$ poorly-, moderately-, and well-aged glasses, as described in the previous section. Tables 5.1, 5.2, and 5.4 (in Section 5.7) detail various properties, such as the number of generations and mesostates contained in them. The ranges of strains that these catalogs sample are indicated in Fig. 3.5, showing how far these catalogs reach out in strain relative to the yield strain under monotonous loading. In addition, we produced 10 catalogs from samples of an ultra-stable glass aged by an average of $4.10^3$ steps per-site. For comparison purposes, we also extracted catalogs from our atomistic simulations, using a set of 8 soft and 30 moderately hard reference configurations, that were obtained via fast and slow quenches from a high-temperature liquid. The description of these atomistic catalogs is given in Section 5.7.

Fig. 5.1 shows sample $t$-graphs from each of the four sets of samples: fast quenched atomistic glass (AS Fast #4), slow quenched atomistic glass (AS Slow #2), poorly-aged mesoscopic glass (Meso PA #1), and the moderately-aged mesoscopic glass (Meso MA #4). The numbers after the # sign specify the particular realization of the glass, as listed in Tables 5.1, 5.2, 5.6, and 5.7. The placement of the vertices of the graph is arbitrary. The mesostate corresponding to the initially prepared glass, i.e. the reference state, is indicated by the large vertex in red and labeled $O$. Note the general tree-like structures in all four $t$-graphs which appear to be qualitatively similar, despite the different underlying model (atomistic *vs.* mesoscopic) and also the different degreee of glass preparation. The color of each vertex indicates the SCC that it belongs to, as we discuss in the next section.

A note of caution when comparing simulations of atomistic and mesoscopic models is in order. As we argue in Section 5.8, our atomistic simulations correspond to an elastoplastic model with size somewhere between $N = 5$ and 10. Thus our atomistic simulations involve systems of smaller size and possibly suffer more from finite-size effects. Moreover, the way the atomistic systems have been aged is different from the aging protocol used for our mesoscopic systems. All of these features make detailed comparisons difficult and we want to stress again, that our main aim in presenting our mesoscopic model is not to quantitatively reproduce the results of atomistic simulations. We will return to this point when comparing the SCC size distributions in section 5.4.

## 5.3 AQS graph topology and strongly connected components (SCCs)

We will probe the topology of the $t$-graphs more deeply by focusing on their SCCs to which any cyclic response must be confined [101], as we explain now. Two mesostates $A$ and $B$ are connected, if on the $t$-graph there is a directed path of **U**- and **D**-transitions that leads from $A$ to $B$. Physically, this implies that there is some shearing protocol that, when applied to $A$, gives rise to a deformation pathway terminating in $B$. We say that two mesostates $A$ and $B$ are *mutually reachable*, if there is a deformation pathway from $A$ to $B$ as well as one from $B$ to $A$. Mutual reachability is an equivalence relation (in particular, if the pairs $A, B$ and $B, C$ are mutually reachable, so must be the pair $A, C$). Therefore, the vertices of the $t$-graph can be partitioned into equivalence classes under mutual reachability and these classes form its SCCs [12]. Numerical details on how to extract SCCs from $t$-graphs have been provided in Ref. [101].

By construction, transitions between any two mesostates belonging to different SCCs are irreversible: there may be a deformation pathway from one to the other, but not back, since otherwise the pair of states would have been mutually reachable. Thus mutual reachability also partitions the set of transitions between mesostates into reversible ones, i.e. those connecting a

Table 5.1 Properties of the 10 catalogs obtained from poorly-aged (PA) glasses of the mesoscopic model with $N = 32$. The catalogs are labeled by their run number, as given in the first column, while $g_{\mathrm{comp}}$ identifies the generation upto which all outgoing mesostate transitions have been identified. The number of mesostates and SCCs found in the catalog are given by $N_0$ and $N_{\mathrm{SCC}}$, respectively. The last four columns provide statistics about limit-cycles under symmetric cyclic shear contained in the catalog: the number $n_{\mathrm{cycles}}$ of limit-cycles found, the number $N_{\mathrm{SCC}}^{\mathrm{supp}}$ of SCCs that support at least one limit-cycle, the size $s_{\mathrm{suppSCC}}^{\max}$ of the largest SCC supporting a limit-cycle, and the number $n_{\mathrm{cycles}}^{\mathrm{maxSCC}}$ of limit-cycles contained in the largest supporting SCC (refer to text for details). The last row is a cumulative total over the entries in the corresponding columns.

| Run | $g_{\mathrm{comp}}$ | $N_0$ | $N_{\mathrm{SCC}}$ | $n_{\mathrm{cycles}}$ | $N_{\mathrm{SCC}}^{\mathrm{supp}}$ | $s_{\mathrm{suppSCC}}^{\max}$ | $n_{\mathrm{cycles}}^{\mathrm{maxSCC}}$ |
|---|---|---|---|---|---|---|---|
| 1 | 35 | 26093 | 5817 | 21631 | 4598 | 91 | 97 |
| 2 | 35 | 59281 | 11084 | 44902 | 8579 | 175 | 84 |
| 3 | 35 | 28418 | 5963 | 23956 | 4261 | 128 | 116 |
| 4 | 35 | 131100 | 29478 | 123341 | 24215 | 106 | 104 |
| 5 | 35 | 48832 | 10374 | 52900 | 9474 | 73 | 67 |
| 6 | 35 | 89710 | 22955 | 101298 | 21130 | 132 | 116 |
| 7 | 35 | 46049 | 11498 | 36801 | 9301 | 139 | 124 |
| 8 | 35 | 145281 | 43409 | 133984 | 34033 | 104 | 67 |
| 9 | 35 | 52641 | 12854 | 56017 | 11595 | 148 | 124 |
| 10 | 35 | 49355 | 10155 | 47003 | 7377 | 115 | 153 |
| **ALL** | n/a | 676760 | 163587 | 641833 | 134563 | n/a | 1052 |

pair of mesostates within the same SCC, and irreversible ones, where the two mesostates must belong to different SCCs. Any periodic and hence reversible response to some shear protocol must therefore be confined to a single SCC. The SCCs are thus the “containers” of reversible behavior [101].

## 5.4 Comparison of the poorly- and moderately-aged catalogs

Tables 5.1 and 5.2 show the properties of the 10 catalogs with $N = 32$ which were obtained by taking the poorly- and moderately-aged mesoscopic glasses as reference states. The second column lists the number of generations $g_{\mathrm{comp}}$ up to which all outgoing mesostate transitions were identified. Thus $g_{\mathrm{comp}} = 39$ means that we have identified every mesostate that can be reached from the reference configuration by a sequence of 39 **U**− and **D**-transitions. Next, $N_0$ and $N_{\mathrm{SCC}}$ list the number of mesostates and SCCs contained in the catalog. The last row of each table provides the cumulative totals. We will discuss the results shown in the last four columns later in this section.

*SCC size distributions* – In Fig. 5.2 we compare the size distribution of the SCCs found in these catalogs. The blue boxes and black circles show the size distribution of SCCs extracted from all 10 catalogs of the $N = 32$ mesoscopic glasses. All curves are normalized but have been vertically offset for clarity. Observe that the size distributions are broad and that the moderately-aged catalogs contain larger SCCs. Nevertheless, power-law fits using the method of Clauset et al. [29] yield a comparable power-law exponent of about $2.3 \pm 0.3$ for both distributions[1]. For comparison purposes, we also show the SCC size distributions obtained from our atomistic simulations under slow and fast quench, labeled as AS slow (triangles) and AS fast (diamonds), corresponding to moderately- and poorly-aged glasses. These catalogs reveal similarly broad distributions, with the moderately-aged catalogs containing again larger SCCs, while the fitted power-law exponents $2.7 \pm 0.3$ are comparable.

Note the presence of a finite-size cut-off around SCC sizes of about 30 and 100 for the mesoscopic PA and MA catalogs, respectively. The SCC size distributions obtained from the atomistic simulations do not feature such a cut-off. In Section 5.8 we argue that the mesoscopic equivalent size $N$ corresponding to our atomstics simulations is somewhere between $N = 4$ and $N = 10$. Thus the atomistic samples are in effect smaller. Fig. 5.6 of Section 5.8 shows the corresponding SCC size distributions when we compare the atomistic simulations with the size distributions obtained from $N = 8$ mesoscopic catalogs. While still there, the finite-size cut-off appears to be less prominent in the distributions of the mesoscopic models, particularly for the MA samples. We think that the suppression of the cut-off is a finite-size effect. In fact, among the 8 AS fast catalogs there are considerable fluctuations in the size $s_{\max}$ of the largest SCC found in each of them. Ordered from smallest to largest, we find $s_{\max} = 106, 243, 244, 259, 379, 413, 458$, and 929. Among these, the smallest value $s_{\max} = 106$ is realized in catalog #4, whose transition graph is shown in Fig. 5.1, while the largest value $s_{\max} = 929$ is observed in catalog #2, whose transition graph is given in Fig. 1(b) of ref. [101]. In fact, we checked for AS fast that the data points for the largest SCC sizes in Fig. 5.2, are singletons corresponding to the largest SCCs found in the catalogs.

Note that while the $t$-graphs and SCC size distributions obtained from our mesoscopic and atomistic model are qualitatively similar, the dependence of these on the degree of aging is rather weak. In other words, the topology of the $t$-graphs alone does not appear to contain features that are directly linked to the different amount of aging these samples have been subjected to. As we will show next, the effect of aging on the samples reveals itself when we combine the topological features of the $t$-graphs with additional physical properties, such as the prevalence of cycles, the strain stability ranges and plastic strains associated with the mesostates and their SCCs.

*Prevalence of cycles* – We next turn to the population of cycles in our catalogs. We are again interested in cycles that can be traversed under a *symmetric* cyclic shear protocol:

---

[1] For the estimate of the exponent, we considered only SCCs with sizes $s_{\text{SCC}} \geq 4$, as in earlier work [101], where this choice was justified by the empirical observation that small SCCs containing mesostates that were added to the catalog at the last generations are more likely to increase in size, if the catalog is augmented by going to a higher number of generations.

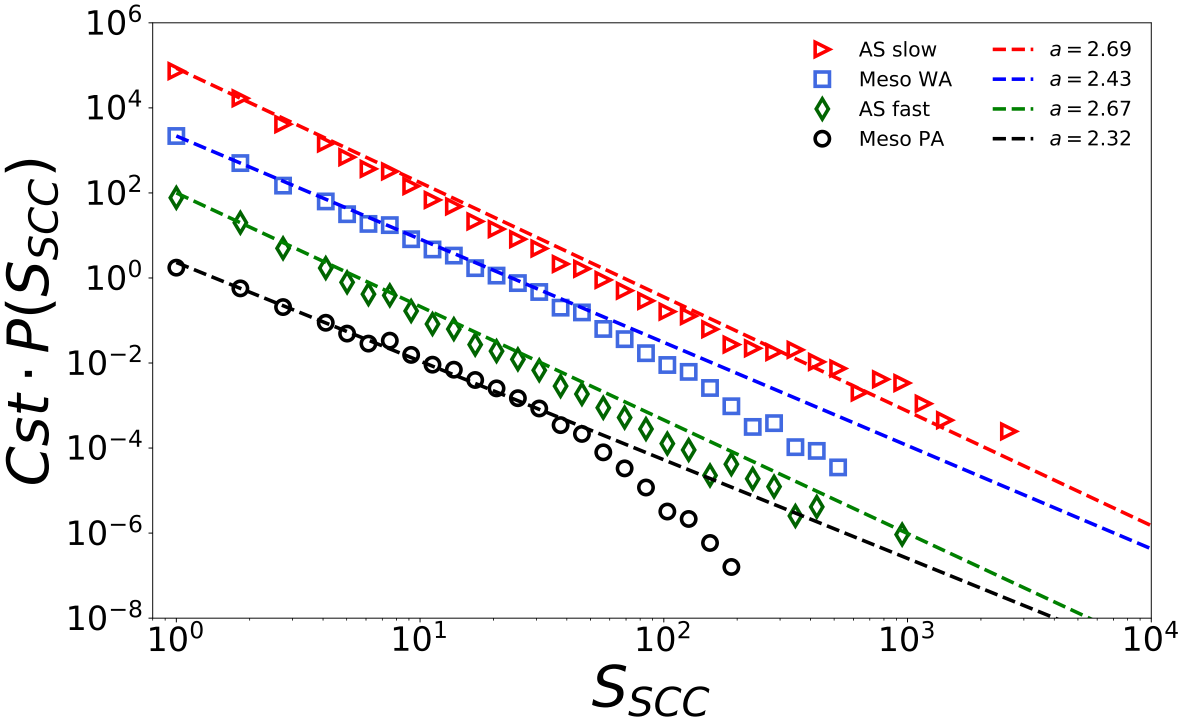

Fig. 5.2 Statistics of SCCs vs thermal history – Comparison of the SCC size distributions obtained from simulations of the atomistic (AS) and $N = 32$ mesoscopic models (Meso) and distinguished by the extent of aging they have been subjected to: moderately-aged, labeled as Meso MA and AS slow, and poorly-aged, labeled as Meso PA and AS fast, respectively. The dashed lines are power-law fits to the data, which were obtained using a common lower SCC size cut-off of $s_{\mathrm{SCC}} = 4$. Curves have been vertically offset for clarity.

Table 5.2 Properties of the 10 catalogs obtained from moderately-aged (MA) glasses of the $N = 32$ mesoscopic model. A brief summary of the quantities listed is given in the caption of Table 5.1, while further details are provided in the text.

| Run | $g_{\mathrm{comp}}$ | $N_0$ | $N_{\mathrm{SCC}}$ | $n_{\mathrm{cycles}}$ | $N_{\mathrm{SCC}}^{\mathrm{supp}}$ | $s_{\mathrm{suppSCC}}^{\mathrm{max}}$ | $n_{\mathrm{cycles}}^{\mathrm{maxSCC}}$ |
|---|---|---|---|---|---|---|---|
| 1 | 39 | 46059 | 8148 | 3510 | 857 | 269 | 7 |
| 2 | 39 | 36279 | 8164 | 1732 | 363 | 451 | 11 |
| 3 | 39 | 130733 | 33324 | 3933 | 1148 | 542 | 129 |
| 4 | 39 | 19344 | 4244 | 1659 | 490 | 207 | 3 |
| 5 | 39 | 147476 | 49335 | 989 | 437 | 133 | 2 |
| 6 | 39 | 64096 | 11678 | 1731 | 643 | 166 | 2 |
| 7 | 39 | 117680 | 30721 | 6189 | 1809 | 244 | 58 |
| 8 | 39 | 64693 | 12657 | 5317 | 1219 | 651 | 179 |
| 9 | 39 | 118964 | 33857 | 3067 | 1143 | 141 | 12 |
| 10 | 39 | 91758 | 26814 | 8516 | 2011 | 201 | 127 |
| **ALL** | n/a | 837082 | 218942 | 36643 | 10120 | n/a | 530 |

$0 \to \epsilon_{\mathrm{amp}} \to -\epsilon_{\mathrm{amp}} \to 0$ with some shear amplitude $\epsilon_{\mathrm{amp}}$. We consider every mesostate in our catalog that is stable at zero strain and apply this cyclic shear protocol, checking whether a cyclic response has set in or not. The column labeled $n_{\mathrm{cycles}}$ of Tables 5.1 and 5.2 lists the total number of distinct cycles found in our catalogs obtained from our moderately- and poorly-aged mesoscopic glasses. We find that the poorly-aged catalogs contain a significantly larger number of cycles, although the total number of mesostates in these catalogs is comparable (836082 and 676760 mesostates, respectively).

As we have noted before, the mesostates forming a cyclic response must all be confined to a single SCC, i.e. a cycle cannot traverse multiple SCCs. We therefore ask next how the cycles found in the catalogs are distributed across the available SCCs. In particular, we ask for the number of SCCs that support at least one symmetric cycle, which we define as $N_{\mathrm{SCC}}^{\mathrm{supp}}$ and list in Tables 5.1 and 5.2. For ease of comparison, we have put together in Table 5.3 the cumulative totals listed in the last lines of these tables along with the corresponding data from our atomistic simulations.

Starting with the mesoscopic glasses, there is again a stark contrast between catalogs obtained from poorly-aged (PA) and moderately-aged (MA) samples (first two rows of Table 5.3). In the MA glasses the symmetric cycles are contained in a relatively small fraction of SCCs (10120 out of a total of 218942 available ones), while for the poorly-aged catalogs a large fraction of SCCs supports at least one such cycle (134563 SCCs that support symmetric cycles out of a total of 163587). From Tables 5.1 and 5.2, we see that this is true also for the individual catalogs. It is thus apparent that in the moderately-aged catalogs a relatively small fraction of SCCs support most of the cycles found, while in the poorly-aged catalogs the opposite is

Table 5.3 Comparison of the cumulative totals of the number of mesostates $N_0$, SCCs $N_{\text{SCC}}$, and SCCs that support symmetric cycles $N_{\text{SCC}}^{\text{supp}}$. The top two rows show data for the poorly-aged (PA) and moderately-aged (MA) mesoscopic glasses. The bottom two rows compare these quantities for the fast and slow cooled atomistic glasses. Refer to text for further details and the Tables 5.6 and 5.7 in Section 5.7 for the sample-by-sample characterization of the atomistic catalogs.

| Catalogs | $N_0$ | $N_{\text{SCC}}$ | $N_{\text{SCC}}^{\text{supp}}$ |
|---|---|---|---|
| **Meso PA** | 676760 | 163587 | 134563 |
| **Meso MA** | 837082 | 218942 | 10120 |
| **AS Fast** | 459508 | 210864 | 10933 |
| **AS Slow** | 555332 | 244334 | 5863 |

the case and almost every SCC supports at least one cycle. A similar, albeit less pronounced behavior is seen also in our atomistic simulations, *cf.* the last two rows of Table 5.3. Note that the cumulative data for poorly-aged (moderately-aged) initial states have been sampled from 8 (30) catalogs (Tables 5.6 and 5.7 in Section 5.7), so that it is hard to compare the overall number of cycles. Nevertheless, we observe also in our atomistic simulations that the number of cycle supporting SCCs in the poorly-annealed catalogs appears to be disproportionally larger.

We finally consider the largest SCCs that support symmetric cycles, comparing their sizes $s_{\text{suppSCC}}^{\text{max}}$ and the number of cycles they contain $n_{\text{cycles}}^{\text{maxSCC}}$. These numbers are shown in the last column of Tables 5.1 and 5.2. Again, we find contrasting behavior. The largest cycle supporting SCCs found in the moderately-aged catalogs are generally larger than those in the poorly-aged ones, but despite of this, they contain fewer cycles.

## 5.5 The disorder landscape: SCCs and SCC exit strains

Our results for the prevalence of symmetric cycles can be summarized as follows: while the poorly-aged catalogs contain a large number of such cycles which are distributed across a large number of SCCs of various sizes, we find that the opposite is true for the catalogs obtained from the moderately-aged samples. For the latter, the number of symmetric cycles contained is far less and these cycles are confined to a small subset of available SCCs.

In order to understand better the difference of the disorder landscape arising from moderately-aged and poorly-aged samples, we coarse-grain the $t$-graph to the level of SCCs, since – as we have shown – any cyclic response must be confined to a single SCC. Every SCC has at least one outgoing **U**- and one outgoing **D**-transition. Let us denote the states from which these outgoing transitions originate as the **U**- and **D**-exits of the SCC. Suppose now that the SCC has only one **U**- and one **D**-exit and denote the threshold strains triggering these exiting transitions as $\mathcal{E}_{\text{SCC}}^{\pm}$. Consequently, given any mesostate $A$ belonging to that SCC and applying strains confined to

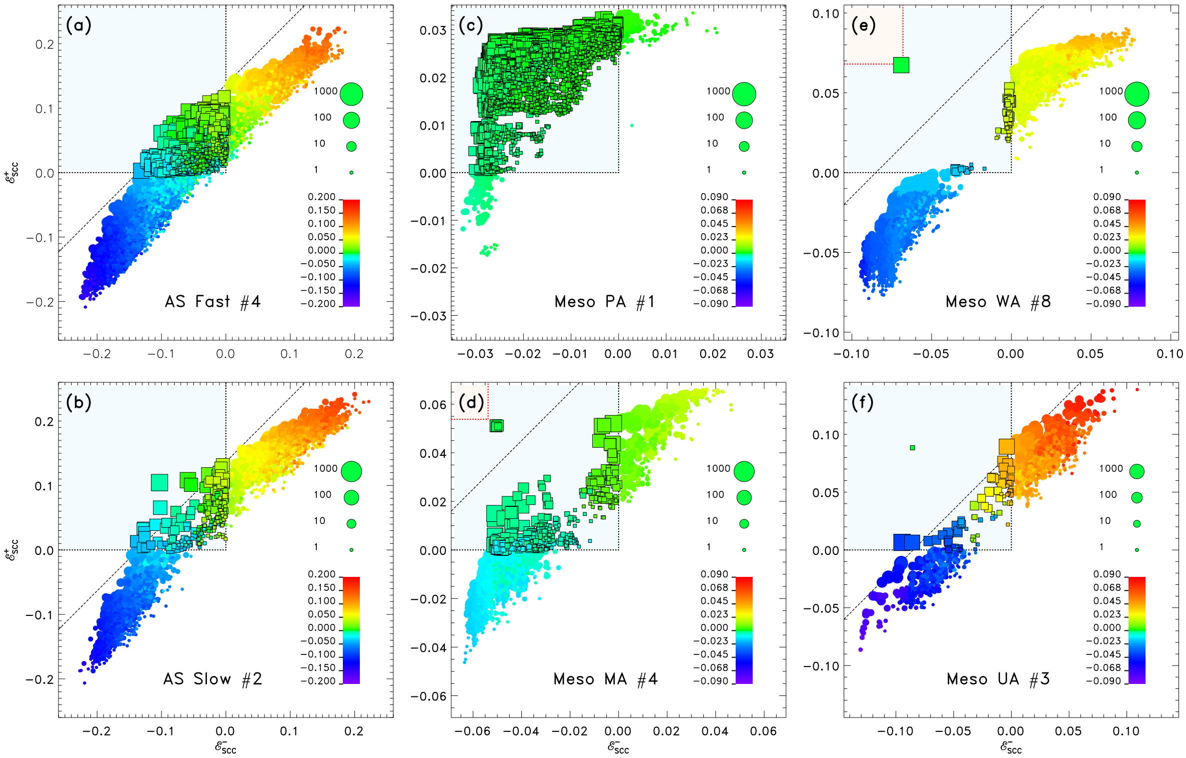

Fig. 5.3 The coarse-grained disorder-landscape, atomistic *vs.* mesoscopic models, and the effect of aging – The six panels show the scatter plots of the SCCs found in catalogs obtained from atomistic (first column) and our $N = 32$ mesoscopic simulations (second and third columns). Panels (e) and (f) depict the disorder landscape extracted from increasingly better-aged samples of the mesoscopic model. Each symbol represents an SCC, while the size and color correspond to the size of the SCC and the average plastic strain $\epsilon^{\rm pl}$ of the mesostates constituting that SCC. Each SCC has at least one **U**- and one **D**-transition that leads to another SCC, and we denote by $\mathcal{E}^{\pm}_{\rm SCC}$ the threshold strains to trigger these transitions. As explained in the text, taking the extremes of these exit strains, the corresponding interval $(\mathcal{E}^{-}_{\rm SCC}, \mathcal{E}^{+}_{\rm SCC})$ provides a range of strain values over which the system will be trapped in that SCC. These strains are used as coordinates for placing the SCC in the plot. Box-shaped symbols indicate that the SCC supports at least one cycle under symmetric cyclic shearing. The area shaded in red in panels (d) and (e) indicates where cycle supporting SCCs would have to be located if they were to contain cycles at strain amplitudes beyond the onset of the irreversibility transition, as obtained from the inset of Fig. 3.9. For panels (c) and (f) this region lies outside the plot window. The diagonal dashed lines corresponds to the average SSC strain range of Eq. 5.3, estimated as $\mathcal{E}^{+}_{\rm SCC} - \mathcal{E}^{-}_{\rm SCC} = \Sigma_{\rm ss}/\mu$, where $\Sigma_{\rm ss}$ is the steady-state stress under monotonous strain loading. Refer to text for further details.

the interval $\mathcal{E}^{-}_{\rm SCC} < \epsilon < \mathcal{E}^{+}_{\rm SCC}$, the resulting sequence of mesostates must remain confined to the SCC. This follows from the observation made before, namely that for any mesostate $A$, $\epsilon^{+}[A] < \epsilon^{+}[\mathbf{U}A]$ and $\epsilon^{-}[\mathbf{D}A] < \epsilon^{-}[A]$.

In the case of multiple **U**- or **D**-exits from an SCC, we define $\mathcal{E}^{+}_{\rm SCC}$ and $\mathcal{E}^{-}_{\rm SCC}$ as the largest, respectively lowest, strain triggering the outgoing transitions. It actually turns out that for the SCCs considered in our catalogs only a very small fraction of SCCs have multiple **U**- or **D**-exits.[2]

Assuming therefore that each SCC has exactly one outgoing **U**- and **D**-transition, it follows that in order for the SCC to support cyclic response under the strain protocol $0 \to \epsilon_{\mathrm{amp}} \to -\epsilon_{\mathrm{amp}} \to 0 \cdots$, we must require that $\mathcal{E}^{+}_{\mathrm{SCC}} > \epsilon_{\mathrm{amp}}$ and $\mathcal{E}^{-}_{\mathrm{SCC}} < -\epsilon_{\mathrm{amp}}$. In particular, this implies that :

$$\mathcal{E}^{-}_{\mathrm{SCC}} < 0 < \mathcal{E}^{+}_{\mathrm{SCC}}. \tag{5.2}$$

Distinguishing the SCCs by (i) their size, and (ii) whether they support a symmetric cycle or not, we now ask how these SCCs are scattered in the plane spanned by $\mathcal{E}^{-}_{\mathrm{SCC}}$ and $\mathcal{E}^{+}_{\mathrm{SCC}}$. Panels (a) and (b) of Fig. 5.3 show the SCC scatter plots obtained from single catalogs of our atomistic poorly-aged and moderately-aged samples, while panels (c) and (d) show the same for catalogs obtained from our mesoscopic poorly-aged and moderately-aged $N = 32$ samples. Panels (e) and (f) show SCC scatter plots obtained from even further aged mesoscopic samples, with an average of 150 and 4000 aging steps per site, respectively (details of these catalogs are provided in Section 5.7). In each panel of the figure the number after the # sign indicates the particular sample from which the data shown came from. The size of the symbols represent the size of the SCCs, as indicated in the legend, while the boxed symbol shape indicates that the SCC actually supports a limit-cycle, as determined by inspecting our catalogs. The highlighted upper left quadrant of each plot corresponds to the region where the inequality (5.2) holds. Since this is the region where any SCC which supports cyclic response under symmetric oscillatory shear must be located, we will refer to it as the *cycle-quadrant*.

We start with a comparison of the poorly-aged (PA) and moderately-aged (MA) SCC scatter plots obtained from our atomistic and mesoscopic glasses, panels (a) – (d). Comparing the catalogs obtained from the PA samples, panels (a) and (c), with those of the MA samples, panel (b) and (d), we see that in all cases the cycle supporting SCCs (boxes) are indeed confined to the cycle-quadrant, i.e. the highlighted region in the top left part of the figure, as they should. Moreover, note the relative sparsity of cycle-supporting SCCs in the atomistic (b) and mesoscopic (d) MA samples, when compared with their poorly-aged counterparts, panels (a) and (c). This is consistent with our earlier observation, namely that relative to the poorly-aged samples, in the MA catalogs only a small fraction of SCCs actually support symmetric cycles.

Plotting the SCCs against their exit strains $(\mathcal{E}^{-}_{\mathrm{SCC}}, \mathcal{E}^{+}_{\mathrm{SCC}})$ also visualizes possible correlations in the locations of cycle supporting SCCs. For the poorly-aged samples, panels (a) and (c), these SCCs fill out the cycle-quadrant rather uniformly and the extent to which this region is filled seems to be limited mainly by the size of the catalog we have sampled, i.e. the number of

---

[2] For the 6 catalogs shown in Fig. 5.3 the percentages of SCCs with more than one **U**- or **D**-exits are: 1.7% (AS Fast), 1.7% (AS Slow), 2.9% (PA), 3.6% (MA), 0.9% (WA), and 7.2% (UA). The low number of exits from SCCs is also apparent from the transition graph excerpts shown in Figs. 5.1 and 5.5.

generations we tracked[3]. This is in contrast to the case of the moderately-aged samples, panels (b) and (d): not only are there fewer SCCs in the cycle-quadrant, but these SCCs tend to cluster around its boundaries, $\mathcal{E}^{+}_{\mathrm{SCC}} = 0$ and $\mathcal{E}^{-}_{\mathrm{SCC}} = 0$, implying thereby that these SCCs can only support cycles with low amplitudes of a symmetrical shear protocol. In fact, for the mesoscopic samples we find that the scarcity of SCCs within the cycle-quadrant and their clustering near its boundary becomes even more pronounced when the samples are aged more, as shown in the SCC scatter plots of panels (e) and (f) which were generated from samples that underwent 150 and 4000 aging steps per site, respectively.

Thus panels (a) – (d) reveal that the SCC scatter plots obtained from our mesoscopic model are qualitatively very similar to their atomistic counterparts: our mesoscopic model captures rather well the difference of the samples due to their aging as well the spatial distribution of the SCCs in the plane plane of exit strains $(\mathcal{E}^{-}_{\mathrm{SCC}}, \mathcal{E}^{+}_{\mathrm{SCC}})$.

Before proceeding, we should note that there are sample-to-sample fluctuations in the scatter plots obtained from the individual glasses. This is also apparent in the variation of catalog properties listed in Tables 5.1 and 5.2, as well as in the tables for the other catalogs given in Section 5.7. In particular, the spatial population of SCCs in the cycle-quadrant varies from sample to sample. Moreover, within a given sample the populations of SCCs in the $(\mathcal{E}^{-}_{\mathrm{SCC}}, \mathcal{E}^{+}_{\mathrm{SCC}})$-plane does not perfectly display the statistical $\mathcal{E}^{\pm}_{\mathrm{SCC}} \to -\mathcal{E}^{\mp}_{\mathrm{SCC}}$ symmetry which arises under interchange of the forward and reverse shearing directions, even though the number of SCCs shown in these plots are rather large. Nevertheless, the features we have been discussing so far and in the following are typical and appear to be robust from sample to sample. Section 5.5.1 contains a discussion of the strip-like arrangement of the SCCs in the plain of exit strains, which is highly pronounced in the case of the atomistic samples, as well as the better-aged mesoscopic ones.

### 5.5.1 Arrangement of SCCs on the plane of exit strains $\mathcal{E}^{\pm}_{\mathrm{SCC}}$

We discuss the spatial arrangement of SCCs along a strip-like region in the $(\mathcal{E}^{-}_{\mathrm{SCC}}, \mathcal{E}^{+}_{\mathrm{SCC}})$, that is clearly evident for the atomistic systems as well as the WA and UA mesoscopic samples in the SCC scatter plots of Fig. 5.3. The diagonal dashed line in each of the plots corresponds to:

$$\Delta\mathcal{E}_{\mathrm{SCC}} = \mathcal{E}^{+}_{\mathrm{SCC}} - \mathcal{E}^{-}_{\mathrm{SCC}}. \tag{5.3}$$

As one would expect, the larger the strain range $\Delta\mathcal{E}_{\mathrm{SCC}}$ over which mesostates are trapped within an SCC, the larger the size of the SCC itself. This trend is clearly visible in all six panels of the plots. The smallest (and most numerous) SCCs are clustered around small values $\Delta\mathcal{E}_{\mathrm{SCC}}$,

---

[3] Note the different strain ranges when comparing atomistic and mesoscopic catalogs, panels (a) – (d) of Fig. 5.3. While the atomistic catalogs sample SCCs whose exit strains well exceed the yield-strain (about 0.13), the mesoscopic catalogs stay well below yielding. This is due to the fact, that the $N = 32$ mesoscopic systems correspond to much larger atomistic systems, then the ones we simulated.

while particularly for the WA and UA samples there appears to be a value $\Delta\mathcal{E}_{\mathrm{SCC}} = \Delta\mathcal{E}_{\max}$ beyond which it is unlikely to find SCCs, except for the outlier SCCs that we have associated with mesostates not having experienced the stress-peak. A naive estimate for $\Delta\mathcal{E}_{\max}$ can be made as follows. Denote by $\Sigma_{\mathrm{ss}}$ the steady-state yield stress reached under monotonous loading (*cf.* Fig. 3.5). Assuming that between $-\Sigma_{\mathrm{ss}}$ and $\Sigma_{\mathrm{ss}}$ the system responds purely elastically, we obtain the estimate $\Delta\mathcal{E}_{\max} = \Sigma_{\mathrm{ss}}/\mu$. From Fig. 3.5 we find that for the mesoscopic samples $\Sigma_{\mathrm{ss}} \approx 0.85$, while for the atomistic samples $\Sigma_{\mathrm{ss}} \approx 2.4$. The dashed lines shown in Fig. 5.3 correspond to these choices, i.e. $\mathcal{E}^{+}_{\mathrm{SCC}} - \mathcal{E}^{-}_{\mathrm{SCC}} = \Sigma_{\mathrm{ss}}/\mu$.

## 5.6 The disorder landscape: Dependence of plastic strains on aging

Having established that the SCC scatter plots are a good proxy to probe topological features of the disorder landscape, we next look more closely at the effect of aging on our mesoscopic glasses. Panels (c) – (f) of Fig. 5.3 show SCC scatter plots obtained from increasingly better aged samples of our mesoscopic glass which – apart from the PA, MA and WA samples we considered so far – now includes also an ultra-aged (UA) glass, obtained from a treatment with 4000 aging steps per site. The properties of the 10 catalogs extracted from these glasses are listed in Table 5.5 of Section 5.7.

Note that the moderately-aged (MA), well-aged (WA), and ultra-aged (UA) samples each display distinct outlier SCCs in the cyclic quadrant. For the MA sample these SCCs are located around $(\mathcal{E}^{-}_{\mathrm{SCC}}, \mathcal{E}^{+}_{\mathrm{SCC}}) = (-0.05, 0.05)$, while for the WA samples these are found at larger strains. These SCCs turn out to be formed by mesostates that can be reached from the initially prepared glass by strain deformation protocols that do not go beyond the stress-peak and hence do not suffer the subsequent large stress-drop.

To understand why with increased aging the cyclic quadrant becomes less densely populated by SCCs and why these tend to cluster near its boundaries, we consider next the plastic strains. Recall that with each mesostate $A$ we associate an elastic branch in the stress-strain plane. In the case of our mesoscopic model, this branch is by construction linear and the plastic strain $\epsilon^{\mathrm{pl}}[A]$ associated with the branch is the (extrapolated) value of the strain where the stress vanishes. By averaging over the plastic strains of the mesostates that belong to an SCC, we obtain a coarse-grained plastic strain for each SCC. The colors of the plot symbols shown in Fig. 5.3 represent the plastic strains of the SCCs, as indicated by the color table legends. Note that for the mesoscopic samples, panels (c) – (f), we have color-coded the same range of plastic strains. Thus the shift of colors towards blue and red as the samples get better aged indicates that the magnitudes of typical plastic strains increase with aging.

Moreover, we see that the distribution of plastic strains across SCCs is strikingly different for the differently aged samples. The well- and ultra-aged samples reveal a clear bi-modal

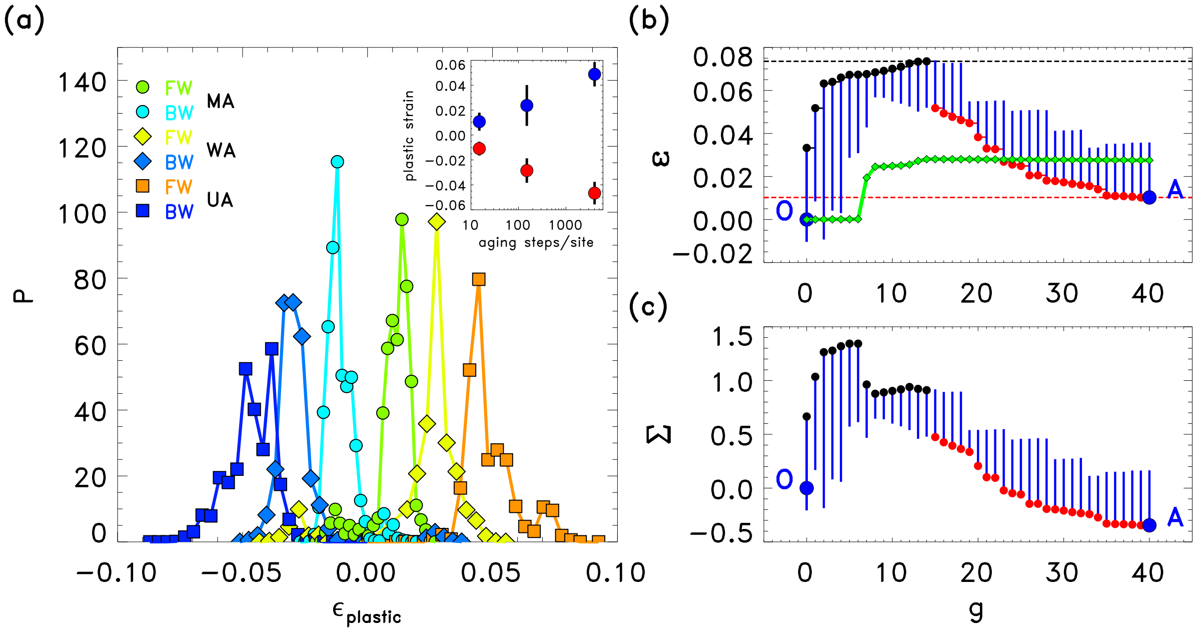

Fig. 5.4 (a) Distribution of plastic strains of mesostates whose deformation paths have passed through the forward (FW) or backward (BW) stress peak. The distributions were extracted from all moderately-, well- and ultra-aged catalogs aged, respectively, by 15 (MA), 150 (WA) and 4000 (UA) aging steps per site, and are labeled by circle-, diamond- and square-shaped plotting symbols. Each color refers to a different choice of aging and whether the FW or BW stress peak was encountered first, as indicated in the legend. The inset shows the evolution of the mean values of the FW (red symbols) and BW (blue symbols) plastic strain distributions. The standard deviation of the distributions is indicated by the black bars. (b) and (c) sample strain and stress deformation path for a mesostate $A$ from the WA sample #8, which experiences the FW stress peak first. $A$ is reached from the well-aged glass by undergoing 15 **U**-transitions followed by 25 **D**-transitions. The $x$-axis indexes the sequence of transitions while the black and red circles on the $y$-axis indicate the strains, panel (b), and stresses, panel (c), at which the transitions occur. The vertical blue lines indicate the extents of each of the elastic branches of the mesostates encountered along the deformation path from $O$ to $A$. The FW stress drop of $\Delta\Sigma \approx 0.4$ occurs during the **U**-transition at $g = 7$, as visible in panel (c). The green diamonds in panel (b) mark the plastic strains associated with the elastic branches visited. Refer to the text for further details.

distribution of plastic strains, characterized by very few SCCs that have vanishing plastic strains[4]. For the poorly-aged sample, panel (c), the distribution of plastic strains appears to be unimodal, with a large number of SCCs, particularly those in the cycle quadrant, having plastic strains of very small magnitude.

To understand better the segregation of SCCs by plastic strain, we turn to the mesostates and their deformation histories. Given a mesostate $A$, we consider the deformation path that leads to it from the initially prepared glass state $O$. In particular, we are interested in mesostates whose deformation path experiences the stress-peaks and subsequent stress-drops, that are encountered

---

[4] In all four panels of Fig. 5.3 the green color used in the legend of the SCCs sizes corresponds to the color-coding of vanishing plastic strains.

during monotonous shearing in the forward or backward direction. We distinguish such states by whether the stress-drop in the forward or backward direction was experienced first, and call these FW, respectively BW mesostates. In Fig. 5.6(a) we plot for each level of aging (MA, WA, or UA) the plastic strain distribution extracted from the elastic branches associated with the FW mesostates found in all 10 catalogs. We do the same for BW mesostates. For each level of aging we have thus two distributions of plastic strains: one associated with FW, and one associated with BW mesostates. We see that these distributions are peaked and the location of the peaks move away from each other as the samples are better aged. This can also be seen in the inset of Fig. 5.6(a) where we plot the averages of these distributions against the aging level. The bars accompanying each symbol indicate the standard deviation of these distributions.

Panels (b) and (c) of Fig. 5.6 show the deformation path of one particular FW mesostate $A$ from the WA catalog. In both panels the horizontal axis labels the mesostate transitions starting from the initial glass state $O$ and leading to $A$. Panel (b) shows the evolution of strain, while (c) depicts the evolution of stress. Black and red circles mark the values at which each transition occurs, respectively indicating whether the transition happened as a result of a strain increase (black) or decrease (red). The blue vertical lines indicated the extent in strain (b) and stress (c) for each of the elastic branches associated with the mesostates encountered along the deformation path.

The protocol of applied strain that leads from $O$ to $A$ has an initial segment where the strain is monotonously increased to about $\varepsilon = 0.08$ (black dashed horizontal line), giving rise to 15 $U$-transitions. Subsequently, the strain is monotonously decreased to about zero (red dashed horizontal line) over 25 $D$-transitions. The large FW stress drop of $\Delta\Sigma \approx 0.4$ is seen to occur at step $g = 7$, while the strain is still increasing. The green curve superimposed in panel (b) shows the plastic strain associated with each of the mesostate elastic branches along the deformation path. We see that the stress-drop at step $g = 7$ is accompanied by a large increase in the plastic strain. As we keep on increasing the driving strain, the plastic strain continues to increase with $g$, though much more slowly. Remarkably, once we start decreasing the strain again, the plastic strain does not change appreciably. This shows that the changes in plastic strain accrued as a result of experiencing the stress drop are subsequently very difficult to undo, since even a monotonous and prolonged decrease of strain does not seem to change the plastic strain value very much.

We verified that for the better aged glasses, MA, WA and UA, that all mesostates with an appreciable plastic strain have a deformation history that experiences the stress drop. We thus are able to link the bi-modal nature of the SCC plastic strain distribution to the passage through the corresponding stress peak which is then accompanied by a stress-drop, as demonstrated in Fig. 5.6(b), (see also the $t$-graph excerpts shown in Fig. 5.5 of Section 5.7, where transitions accompanied by larger stress drops have been marked). The better the aging, the larger the stress drops, and hence the larger the jumps in plastic strain, and the more separated are the peaks of the FW and BW distributions.

More importantly, as the evolution of plastic strains in Fig. 5.6(b) clearly shows, these gains in plastic strain due to the experienced stress drop are apparently very hard to undo by subsequently shearing in the reverse direction. We find that under shearing in the reverse direction the sample has now been significantly softened, i.e. it has become more plastic (the last 5 transitions from $g = 35$ to 40 happen at nearly constant strain), indicating a rejuvenation of the sample [8]. Thus for the well-aged and ultra-well-aged samples the diagonal $\mathcal{E}^{-}_{\mathrm{SCC}} + \mathcal{E}^{+}_{\mathrm{SCC}} = 0$ divides the plane of exit strains into an upper and lower half. SCCs located in the upper (lower) half of the plot are SCCs whose mesostates were reached by passing through the forward (reverse) stress peak. This is also consistent with the excerpts from the corresponding transition graphs shown in Fig. 5.5 of Section 5.7.

## 5.7 Catalogs extracted from simulations of the atomistic model and the mesoscopic model with well-aged reference configurations.

In addition to the Tables 5.1 and 5.2 in the main text, which describe the properties of catalogs extracted from moderately- and poorly-aged glasses of our mesoscopic model with $N = 32$, we also list here the properties of (i) two increasingly better-aged mesoscopic catalogs, prepared from glasses subjected to 150 and 4000 aging steps per site, which we will refer to as the well-aged (WA) and ultra-aged (UA) glasses, respectively, and (ii) atomistic catalogs obtained from 8 poorly-aged and 30 well-aged reference configurations. The aging of the atomistic glasses is controlled by the rate of quenching to zero temperature from a high temperature liquid, as described in Section 3.3. We refer to these as fast (AS Fast) and slowly (AS Slow) quenched atomistic glasses, respectively.

Fig. 5.5 shows an excerpt of the transition graph extracted from samples of sample #8 of our WA glass, panel (a), and sample #3 of the ultra-stable UA glass, panel (b). The number of mesostates displayed in the $t$-graph excerpts shown are 1665 and 4610, respectively. We have obtained the graphs shown in Fig. 5.1 of the main text as well as in Fig. 5.5 by starting out in the reference configuration and following SCCs and the transitions between them until at least 1500 mesostates have been collected. For every SCC reached in this way, we added also the remaining mesostates belonging to that SCC so that the total number of vertices constituting the graph excerpt is typically larger than 1500. The number of SCCs shown in the excerpts of the two graphs in Fig. 5.5 are 216 (WA) and 19 (UA). The sizes of SCCs seen in the WA excerpt are small ($s_{\mathrm{SCC}} \leq 56$), while the UA excerpt has three very large SCC with sizes $s_{\mathrm{SCC}} = 3173, 1271$, and 82, shown in pink, yellow, and green, respectively. These findings are consistent with the

(a) Meso WA #8

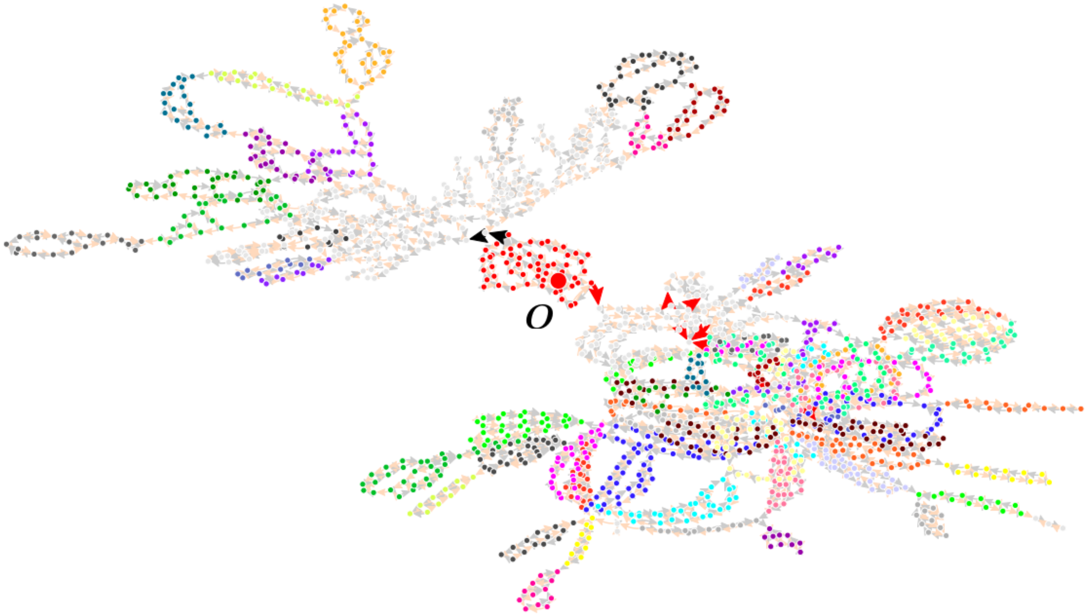

(b) Meso UA #3

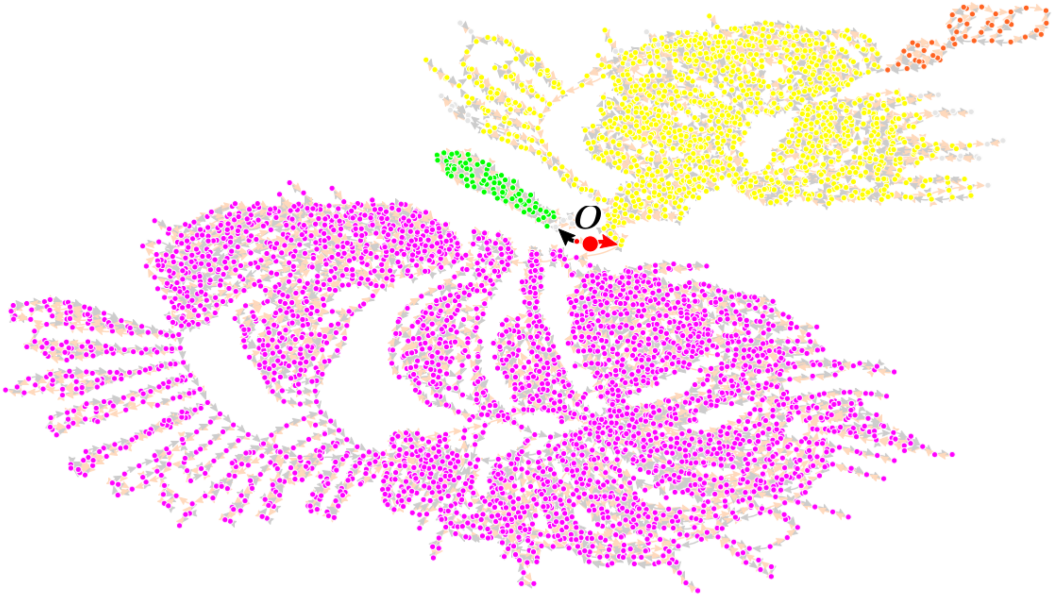

Fig. 5.5 Excerpts of transition graphs extracted from well-aged (WA) and ultra-well-aged (UA) mesoscopic glasses with $N = 32$. Refer to text for further details.

Table 5.4 Properties of the 10 catalogs obtained from the $N = 32$ well-aged (WA) reference configurations aged at 150 aging steps per site of our mesoscopic model. Refer to the caption of Table 5.1 for the description of the columns.

| Run | $g_{\text{comp}}$ | $N_0$ | $N_{\text{SCC}}$ | $n_{\text{cycles}}$ | $n_{\text{suppSCC}}$ | $s^{\text{max}}_{\text{suppSCC}}$ | $n^{\text{maxsuppSCC}}_{\text{cycles}}$ |
|---|---|---|---|---|---|---|---|
| 1 | 39 | 79565 | 25151 | 130 | 44 | 60 | 50 |
| 2 | 39 | 91201 | 27337 | 60 | 33 | 475 | 1 |
| 3 | 39 | 114686 | 36931 | 305 | 14 | 300 | 219 |
| 4 | 39 | 124298 | 33459 | 525 | 107 | 344 | 32 |
| 5 | 39 | 38629 | 13207 | 685 | 181 | 419 | 12 |
| 6 | 39 | 64475 | 13240 | 1388 | 606 | 127 | 7 |
| 7 | 39 | 26421 | 6677 | 115 | 45 | 38 | 12 |
| 8 | 39 | 80317 | 37092 | 122 | 65 | 56 | 50 |
| 9 | 39 | 68154 | 17009 | 43 | 5 | 26 | 38 |
| 10 | 39 | 84064 | 34515 | 66 | 2 | 88 | 42 |
| **ALL** | n/a | 771810 | 244618 | 3439 | 1102 | n/a | 463 |

Table 5.5 Properties of the 10 catalogs obtained from the $N = 32$ ultra-aged (UA) reference configurations aged at 4000 aging steps per site of our mesoscopic model. Refer to the caption of Table 5.1 for the description of the columns.

| Run | $g_{\text{comp}}$ | $N_0$ | $N_{\text{SCC}}$ | $n_{\text{cycles}}$ | $n_{\text{suppSCC}}$ | $s^{\text{max}}_{\text{suppSCC}}$ | $n^{\text{maxsuppSCC}}_{\text{cycles}}$ |
|---|---|---|---|---|---|---|---|
| 1 | 45 | 24999 | 2714 | 162 | 57 | 433 | 1 |
| 2 | 45 | 22443 | 1758 | 486 | 114 | 625 | 72 |
| 3 | 45 | 25541 | 1834 | 468 | 79 | 3173 | 43 |
| 4 | 45 | 28065 | 5796 | 205 | 77 | 703 | 5 |
| 5 | 45 | 77224 | 24002 | 94 | 51 | 168 | 8 |
| 6 | 45 | 19225 | 1643 | 314 | 107 | 2489 | 4 |
| 7 | 45 | 17750 | 1394 | 300 | 104 | 1292 | 1 |
| 8 | 45 | 15036 | 1066 | 681 | 107 | 1428 | 35 |
| 9 | 45 | 68780 | 14479 | 94 | 54 | 60 | 2 |
| 10 | 45 | 17118 | 1129 | 911 | 161 | 1467 | 93 |
| **ALL** | n/a | 316181 | 55815 | 3715 | 911 | n/a | 264 |

SCC scatter plots shown in panels (e) and (f) of Fig. 5.3. We believe that the emergence of the giant SCCs in the ultra-stable sample is a finite-size effect.

The stress-strain curves of the well-aged samples under uniform shear exhibit large stress changes across the yielding transition. For the WA and UA samples shown in Fig. 5.5, the magnitude of these stress-jumps under shear in the forward and reverse directions are $\Delta\Sigma = 0.46, 0.45$ for the WA glass and $\Delta\Sigma = 0.62, 0.70$ for the ultra-stable UA glass. In the graphs shown in Fig. 5.5 we have highlighted transitions that involve stress-jumps with a magnitude of at least 0.1, by fat black (**U**-transition) and red arrows (**D**-transition). Despite of the relative low threshold value chosen for these jumps, only very few transitions in the two graphs shown experience large stress changes. Note that for both the WA and UA samples the transitions involving the large stress-jumps under forward and reverse shear tend to partition the graph into two halves (at least to the resolution of the number of vertices shown). This effect is even more dramatic for the ultra-stable glass sample where the transitions with large stress jumps immediately leads to giant SCCs.

Table 5.6 Properties of the 8 catalogs obtained from poorly-aged (fast quench) reference configurations of our atomistic model. Refer to the caption of Table 5.1 for the description of the columns.

| Run | $g_{\text{comp}}$ | $N_0$ | $N_{\text{SCC}}$ | $n_{\text{cycles}}$ | $N^{\text{supp}}_{\text{SCC}}$ | $s^{\text{max}}_{\text{suppSCC}}$ | $n^{\text{maxSCC}}_{\text{cycles}}$ |
|---|---|---|---|---|---|---|---|
| 1 | 40 | 57638 | 24123 | 4650 | 1617 | 929 | 215 |
| 2 | 43 | 56158 | 27733 | 4515 | 1451 | 413 | 217 |
| 3 | 37 | 55658 | 24119 | 5380 | 1305 | 106 | 9 |
| 4 | 36 | 55057 | 24931 | 6972 | 1901 | 244 | 255 |
| 5 | 41 | 57602 | 27645 | 3297 | 834 | 458 | 396 |
| 6 | 35 | 53114 | 27939 | 4694 | 1453 | 259 | 244 |
| 7 | 41 | 65842 | 29580 | 4323 | 1185 | 379 | 253 |
| 8 | 45 | 58439 | 24794 | 5068 | 1187 | 234 | 235 |
| **ALL** | n/a | 459508 | 210864 | 38899 | 10933 | n/a | 1824 |

## 5.8 Estimating the mesoscopic equivalent of the size of atomistic simulations

Although our goal is not to quantitatively map the elastoplastic model onto atomistic simulations, we must ensure that the disordered landscape statistics are comparable between the two types of models. From this point of view, being able to estimate the number of simulated elements of the mesoscopic model, i.e. the system's number of degrees of freedom, is essential for a reasonable comparison which takes also into account possible finite-size effects.

To estimate the equivalent number of simulated elements, one must first determine the element size of the elastoplastic model below which the mechanical description is unresolved. This size corresponds to an upper limit of the characteristic plastic rearrangement size. Several experimental approaches have been performed to estimate the size of rearrangements ranging from direct observations in colloidal systems [110] to indirect estimations from strain rate sensitivity analysis in metallic glasses [74]. In all of these cases, the results show that plastic rearrangement cores contain a few dozen particles, so that the overall sizes of these cores range from about two to three particle diameters.

Table 5.7 Properties of the 30 catalogs obtained from well-aged (slow quench) references configurations of our atomistic model. Refer to the caption of Table 5.1 for the description of the columns.

| Run | $g_{\mathrm{comp}}$ | $N_0$ | $N_{\mathrm{SCC}}$ | $n_{\mathrm{cycles}}$ | $N^{\mathrm{supp}}_{\mathrm{SCC}}$ | $s^{\max}_{\mathrm{suppSCC}}$ | $n^{\mathrm{maxSCC}}_{\mathrm{cycles}}$ |
|---|---|---|---|---|---|---|---|
| 1 | 37 | 21105 | 11892 | 908 | 118 | 642 | 285 |
| 2 | 39 | 16416 | 7202 | 797 | 211 | 196 | 148 |
| 3 | 34 | 13894 | 5774 | 1101 | 264 | 503 | 135 |
| 4 | 34 | 13710 | 5188 | 874 | 246 | 328 | 153 |
| 5 | 37 | 18417 | 10118 | 552 | 140 | 371 | 120 |
| 6 | 40 | 17618 | 6659 | 1660 | 275 | 718 | 302 |
| 7 | 31 | 21250 | 10511 | 1373 | 371 | 330 | 64 |
| 8 | 37 | 20940 | 8876 | 907 | 349 | 802 | 170 |
| 9 | 43 | 18145 | 8578 | 664 | 26 | 980 | 78 |
| 10 | 34 | 16847 | 6895 | 793 | 200 | 334 | 33 |
| 11 | 32 | 13849 | 7535 | 766 | 201 | 521 | 178 |
| 12 | 40 | 17723 | 7326 | 1200 | 233 | 356 | 148 |
| 13 | 36 | 19814 | 10441 | 465 | 106 | 343 | 193 |
| 14 | 41 | 22248 | 8824 | 1132 | 220 | 513 | 251 |
| 15 | 35 | 14288 | 7221 | 727 | 123 | 377 | 199 |
| 16 | 39 | 20930 | 7124 | 1562 | 257 | 2688 | 712 |
| 17 | 42 | 15207 | 4769 | 1884 | 252 | 1017 | 375 |
| 18 | 42 | 20779 | 7891 | 1719 | 271 | 1232 | 583 |
| 19 | 35 | 16019 | 7276 | 712 | 186 | 729 | 263 |
| 20 | 39 | 17477 | 6786 | 765 | 169 | 1489 | 307 |
| 21 | 37 | 22784 | 11117 | 447 | 78 | 486 | 226 |
| 22 | 38 | 17773 | 6717 | 473 | 96 | 853 | 181 |
| 23 | 34 | 18273 | 7791 | 549 | 180 | 118 | 48 |
| 24 | 42 | 24157 | 8904 | 1099 | 256 | 451 | 102 |
| 25 | 37 | 14743 | 4966 | 1092 | 207 | 1199 | 274 |
| 26 | 39 | 19295 | 9505 | 664 | 192 | 383 | 89 |
| 27 | 36 | 19070 | 9547 | 873 | 301 | 518 | 146 |
| 28 | 39 | 23452 | 10941 | 786 | 105 | 892 | 172 |
| 29 | 42 | 18683 | 8289 | 822 | 89 | 833 | 341 |
| 30 | 39 | 20426 | 9671 | 1493 | 141 | 963 | 883 |
| **ALL** | n/a | 555332 | 244334 | 28859 | 5863 | n/a | 7159 |

The determination of this length scale in atomistic simulations poses several difficulties. First, the presence of avalanches makes it challenging to identify the individual rearrangements. Second, there is no method yet to spatially distinguish between the non-linear and non-affine elastically strained zones from the non-reversible plastic responses. Finally, another complication arises from the fact that the same zone can contain several slip directions in a realistic particle system [7, 84, 108], resulting in an effective higher density of potential rearrangements than that of a scalar description. Several approaches have been implemented to deal with these difficulties. They rely on the analysis of long-range elastic fields [3, 84], the quantitative calibration of elasto-plastic models [40], the calculation of the spatial extension of rearrangements [100], the strain's spatial correlations [67, 85], and the reproduction of the mechanical response from the spatial density of barriers [91]. These approaches, particularly those using a two-dimensional system under AQS loading like ours, lead to a consistent estimate of the linear size of plastic rearrangements lying between 3 and 7 particle diameters. For our atomistic system containing 1024 atoms, these bounds lead to an equivalent mesoscopic system size between $N = 5$ and 10.

We conclude this section with a comparison of the SCC distributions obtained from our atomistic simulations with those obtained from catalogs of its mesocopic size-equivalent with $N = 8$. The properties of our $N = 8$ mesoscopic catalogs are given in Table 5.8 below. The distributions are broad, and a prominent size cut-off at largest SCC sizes is now less prominent for the mesoscopic distributions when compared with the SCC size distributions obtained from the $N = 32$ mesoscopic catalogs, shown in Fig. 5.2.

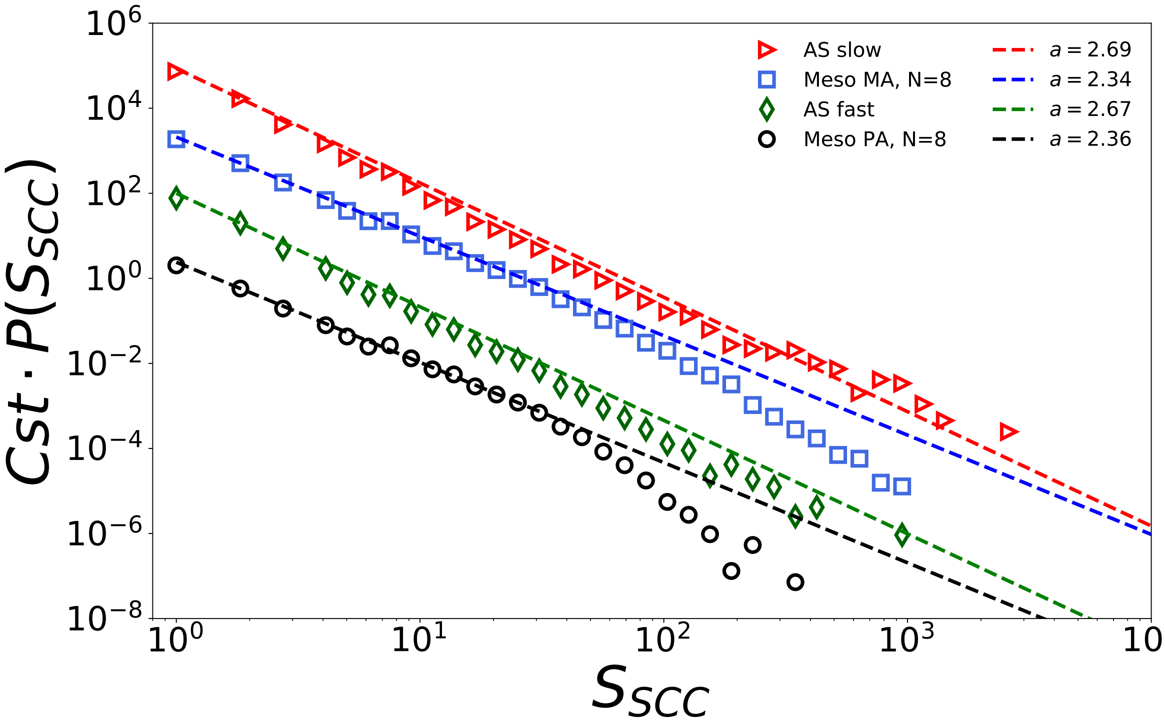

Fig. 5.6 Comparison of the SCC distribution obtained from the atomistic simulations with those obtained from a mesoscopic model with compatible system size $N = 8$. Shown are the distributions for poorly- and medium-aged glasses.

Table 5.8 Properties of the 10 catalogs obtained from the mesoscopic $N = 8$ poorly-aged and moderately-aged reference configurations, shown in the left and right table respectively. Refer to the caption of Table 5.1 for the description of the columns.

| Run | $g_{\text{comp}}$ | $N_0$ | $N_{\text{SCC}}$ |
|---|---|---|---|
| 1 | 35 | 154630 | 45402 |
| 2 | 35 | 88933 | 22904 |
| 3 | 35 | 53179 | 15172 |
| 4 | 35 | 72471 | 21710 |
| 5 | 35 | 121168 | 33327 |
| 6 | 35 | 26003 | 5610 |
| 7 | 35 | 45376 | 11676 |
| 8 | 35 | 74215 | 20657 |
| 9 | 35 | 66648 | 15469 |
| 10 | 35 | 31616 | 7181 |
| **ALL** | n/a | 734239 | 199108 |

| Run | $g_{\text{comp}}$ | $N_0$ | $N_{\text{SCC}}$ |
|---|---|---|---|
| 1 | 44 | 74274 | 17668 |
| 2 | 44 | 74301 | 18749 |
| 3 | 44 | 54534 | 12360 |
| 4 | 44 | 148645 | 39763 |
| 5 | 44 | 113394 | 26659 |
| 6 | 44 | 246908 | 76190 |
| 7 | 39 | 341077 | 99587 |
| 8 | 44 | 25234 | 4347 |
| 9 | 44 | 163766 | 38098 |
| 10 | 44 | 154641 | 33074 |
| **ALL** | n/a | 1396774 | 366495 |

# Chapter 6

# Conclusion and future directions

In this thesis, by using a novel ingredient for the well established elastoplastic models, we capture limit cycles to study the irreversibility transition in cyclically sheared amorphous solids by accounting the effects of sample preparation and system size. The key ingredient is a local stress landscape accessible to the individual lattice sites in our model which are quenched in "time", that is, along the direction of the deformation.

Irrespective of the degree of annealing of the glass sample, we have shown that the approach to the irreversibility transition depends significantly on system size. However, the nature of the transition marked by the disappearance of limit cycles across the irreversibility transition depends on the degree of annealing of glass samples. Poorly-aged samples show a power-law response for both the duration of transients and the mean period of limit cycles close to the irreversibility transition. Contrastingly, well-aged glass under cyclic shear at larger system sizes emerge with limit cycles almost immediately or not at all. This signals that the irreversibility transition under cyclic shear of well-aged glass is sharp and possibly a discontinuous transition. In the case of the better aged samples, we find that cyclic response under oscillatory shear emerges after only a few loading cycles. The dependence on system size is more pronounced in this case. Samples of small size exhibit a cyclic response containing many plastic events and this response continues up to strain amplitudes at which the system would have yielded under monotonous shear loading. However, as the sample size increases, the cyclic response becomes more elastic and the range of strain amplitudes at which it is exhibited shrinks. Changing the system size in our moderately- and well-aged samples allows us to gradually transition from a cyclic response whose phenomenology is characteristic of poorly-aged glasses to one where this cyclic response is dominantly elastic at larger sizes.

To further understand the role of annealing, we turn to transition graph or a $t$-graph representation of the dynamics of sheared amorphous solids. A $t$-graph representation captures the response to arbitrary shear driving protocols under any combination of forward and reverse shear. To study the effect of annealing, we generate $t$-graphs at different degrees of annealing and system size. We considered a particular topological quantity characterizing the $t$-graphs, its strongly connected components (SCCs), since any cyclic response has to be confined to a single SCCs. The size distribution of SCCs sampled from both atomistic and mesoscopic simulations of differently aged samples all follow a power-law with an exponent that varies little with the extent of aging but is slightly smaller for the mesoscopic systems than for the atomistic ones. A closer inspection that also takes into account physical properties associated with the SCCs, in particular their range of stability and typical plastic strains, turns out to be extremely informative. We find that the sample age induces a gradual phase separation between domains of stability centered either on the initial state or at a finite positive or negative plastic strain. The complex age-dependence of the interplay between the amplitude of the center of the domain and the width of the stability ranges has important consequences on the accessibility of limit cycles depending on the particular parameters of the cycling protocols.

Our studies on the effect of sample preparation on the dynamics of sheared amorphous solids is made possible by introducing a simple but physically motivated glass preparation protocol that helps tune the initial degree of annealing of the sample continuously. Such a preparation protocol is tested to recover the response of such samples against unidirectional shear. This includes a ductile to brittle transition as the degree of annealing is increased with a macroscopic response to strain that settle in the same stationary state irrespective of the degree of annealing of the sample.

Finally, using our elastoplastic model, we also study memory effects in cyclically sheared amorphous solids for poorly-aged glasses. We first show that we can capture memories of single and multiple training amplitudes. We also show how the emergence of multi-period limit cycles and/or absence of limit cycles affect the memories of training as the driving increases past the irreversibility transition. We complement these studies using our observations from $t$-graph. We showed that the memory of training is also encoded in the distributions measuring local distance to stress thresholds of the trained state. We then demonstrated that while it may take a glass sample many cycles to settle in a limit cycle especially in the vicinity of the irreversibility transition, the number of driving cycles required to encode memory of training can be significantly less. Our studies also highlight that, irrespective of the training amplitude, a trained state obtained under cyclic driving can encode memory of shear direction which can be revealed through suitably desgined read-out protocols. A memory of shear direction is established rather immediately under cyclic driving. Almost all these observations are supplemented under two different types of protocols that reveal memory of training. One that is accessible in simulations only while the other can be realised in experiments. Finally, we show that a glass sample that is trained under cyclic shear can have very different affinity towards learning additional memories of training against fresh undeformed glass samples. We also discuss some of our observations against well studied hysteron-based models and also make connections to previous studies where interactions are neglected or purely ferromagnetic.

## 6.1 Perspectives

Having demonstrated that our mesoscopic model reproduces key features of amorphous solids under variable athermal quasistatic loading, we conclude with a discussion of possible directions for future research. Compared to atomistic models, the computational cost of simulation of mesoscale models is rather low, allowing us to perform extensive numerical computations as well as probing system sizes not accessible to atomistic simulations. In this context, it would be nice to understand better the complex interplay between finite-size effects and the degree of aging that we have observed under oscillatory shear. In the same vein, a detailed statistical analysis of the spatial structure and correlations of sites that undergo plastic activity will be of interest both near the yielding transition, and also in the evolution of the transients toward cyclic response under oscillatory shear. In this context, it would be relevant to understand how the spatial structure of sites of plastic activity associated with transitions within an SCC correlates with the size of the SCC and its stability range. In fact, one can regard the set of such active sites as a fingerprint of its SCC and ask how this set changes under transitions to neighbouring SCCs, thereby defining an overlap function between SCCs. Since SCCs are containers of periodic response, the strength of such overlaps will have implications for memory formation. Strong overlaps would imply that similar cyclic responses can be realized in neighbouring SCCs. At the same time, such overlaps can also be used to characterize in greater detail the topology of the disorder landscape and its possible hierarchical organization.

Our findings have also implications for memory formation in amorphous solids. Cyclic response under oscillatory shear can encode information and thus form a “memory” about the forcing that caused the response [59]. Viewed within the framework of the $t$-graphs any periodic response must be confined to one of its SCCs. Thus the evolution under oscillatory shear is primarily a search for a confining SCC. In fact, such SCCs not only contain the cycle forming the cyclic response, but a hierarchy of nested cycles, one of which forms the cyclic response. A hierarchical organization of cycles is typically associated with return point memory [78, 79, 101]. In particular, the size of an SCC, i.e. the number of configurations they contain, can be regarded as a proxy for memory capacity [101].

Since we find that the distribution of SCC sizes is broad, irrespective of the thermal histories of the glasses from which these distributions were sampled, this suggest a high memory capacity even for well-aged glasses. However, a closer look at the stability ranges of the SCCs found in these glasses, reveals that only the poorly-aged samples have a large abundance of SCCs that can support symmetric cyclic shearing protocols. Contrastingly, in the case of the well-aged glasses very few SCCs support cyclic response to such oscillatory shear protocols. We find that those that do are characterized by loading/driving histories that did not experience the stress-peak and subsequent stress drop. Consequently, their cyclic response is largely elastic and confined to few and relatively small SCCs.

On the other hand, loading histories in which a stress peak and subsequent stress drop are encountered, invariably give rise to rejuvenation of the sample which is also accompanied by a jump of the plastic strain to non-zero values. As a result, a large number of SCCs become dynamically accessible. However, due to the jumps in plastic strain, these SCCs will only support cyclic response to oscillatory shear if the shear strain is centred around the value of their plastic strain.

# References

[1] Adhikari, M., Mungan, M., and Sastry, S. (2022). Yielding behavior of glasses under asymmetric cyclic deformation. *arXiv preprint arXiv:2201.06535*.

[2] Adhikari, M. and Sastry, S. (2018). Memory formation in cyclically deformed amorphous solids and sphere assemblies. *The European Physical Journal E*, 41:1–17.

[3] Albaret, T., Tanguy, A., Boioli, F., and Rodney, D. (2016). Mapping between atomistic simulations and Eshelby inclusions in the shear deformation of an amorphous silicon model. *Physical Review E*, 93(5):053002.

[4] Amon, A., Nguyen, V. B., Bruand, A., Crassous, J., and Clément, E. (2012). Hot Spots in an Athermal System. *Physical Review Letters*, 108(13):135502.

[5] Argon, A. (1979). Plastic deformation in metallic glasses. *Acta Metallurgica*, 27(1):47–58.

[6] Argon, A. and Kuo, H. (1979). Plastic flow in a disordered bubble raft (an analog of a metallic glass). *Materials Science and Engineering*, 39(1):101–109.

[7] Barbot, A., Lerbinger, M., Hernandez-Garcia, A., García-García, R., Falk, M. L., Vandembroucq, D., and Patinet, S. (2018). Local yield stress statistics in model amorphous solids. *Physical Review E*, 97(3):033001.

[8] Barbot, A., Lerbinger, M., Lemaître, A., Vandembroucq, D., and Patinet, S. (2020). Rejuvenation and shear banding in model amorphous solids. *Physical Review E*, 101(3):033001.

[9] Baret, J.-C., Vandembroucq, D., and Roux, S. (2002). An extremal model of amorphous plasticity. *Phys. Rev. Lett.*, 89:195506.

[10] Barker, J. A., Schreiber, D., Huth, B., and Everett, D. H. (1983). Magnetic hysteresis and minor loops: Models and experiments. *Proceedings of the Royal Society of London. A. Mathematical and Physical Sciences*, 386(1791):251–261.

[11] Barlow, H. J., Cochran, J. O., and Fielding, S. M. (2020). Ductile and brittle yielding in thermal and athermal amorphous materials. *Physical Review Letters*, 125(16):168003.

[12] Barrat, A., Barthelemy, M., and Vespignani, A. (2008). *Dynamical processes on complex networks*. Cambridge University Press, Cambridge.

[13] Ben-Zion, Y. and Rice, J. R. (1993). Earthquake failure sequences along a cellular fault zone in a three-dimensional elastic solid containing asperity and nonasperity regions. *Journal of Geophysical Research: Solid Earth*, 98(B8):14109–14131.

[14] Bense, H. and van Hecke, M. (2021). Complex pathways and memory in compressed corrugated sheets. *Proceedings of the National Academy of Sciences*, 118(50):e2111436118.

[15] Berthier, L., Coslovich, D., Ninarello, A., and Ozawa, M. (2016). Equilibrium sampling of hard spheres up to the jamming density and beyond. *Physical review letters*, 116(23):238002.

[16] Bhaumik, H., Foffi, G., and Sastry, S. (2021). The role of annealing in determining the yielding behavior of glasses under cyclic shear deformation. *Proceedings of the National Academy of Sciences*, 118(16):e2100227118.

[17] Bhaumik, H., Foffi, G., and Sastry, S. (2022a). Avalanches, clusters, and structural change in cyclically sheared silica glass. *Physical Review Letters*, 128(9):098001.

[18] Bhaumik, H., Foffi, G., and Sastry, S. (2022b). Yielding transition of a two dimensional glass former under athermal cyclic shear deformation. *The Journal of Chemical Physics*, 156(6):064502.

[19] Bitzek, E., Koskinen, P., Gähler, F., Moseler, M., and Gumbsch, P. (2006). Structural relaxation made simple. *Physical review letters*, 97(17):170201.

[20] Bocquet, L., Colin, A., and Ajdari, A. (2009). Kinetic theory of plastic flow in soft glassy materials. *Physical review letters*, 103(3):036001.

[21] Bonn, D., Denn, M. M., Berthier, L., Divoux, T., and Manneville, S. (2017). Yield stress materials in soft condensed matter. *Reviews of Modern Physics*, 89(3):035005.

[22] Budrikis, Z., Castellanos, D. F., Sandfeld, S., Zaiser, M., and Zapperi, S. (2017). Universal features of amorphous plasticity. *Nature Comm.*, 8:15928.

[23] Budrikis, Z. and Zapperi, S. (2013). Avalanche localization and crossover scaling in amorphous plasticity. *Phys. Rev. E*, 88:062403.

[24] Bulatov, V. V. and Argon, A. S. (1994a). A stochastic model for continuum elasto-plastic behavior. II. A study of the glass transition and structural relaxation. *Modelling and Simulation in Materials Science and Engineering*, 2(2):185–202.

[25] Bulatov, V. V. and Argon, A. S. (1994b). A stochastic model for continuum elasto-plastic behavior. II. A study of the glass transition and structural relaxation. *Modelling and Simulation in Materials Science and Engineering*, 2(2):185–202.

[26] Bulatov, V. V. and Argon, A. S. (1994c). A stochastic model for continuum elasto-plastic behavior. III. Plasticity in ordered versus disordered solids. *Modelling and Simulation in Materials Science and Engineering*, 2(2):203–222.

[27] Castellanos, D. F., Roux, S., and Patinet, S. (2022). History dependent plasticity of glass: A mapping between atomistic and elasto-plastic models. *Acta Materialia*, 241:118405.

[28] Chen, K., Bak, P., and Obukhov, S. (1991). Self-organized criticality in a crack-propagation model of earthquakes. *Physical Review A*, 43(2):625.

[29] Clauset, A., Shalizi, C. R., and Newman, M. E. (2009). Power-law distributions in empirical data. *SIAM Rev.*, 51(4):661–703.

[30] Coppersmith, S., Jones, T., Kadanoff, L., Levine, A., McCarten, J., Nagel, S., Venkataramani, S., and Wu, X. (1997). Self-organized short-term memories. *Physical review letters*, 78(21):3983.

[31] Corte, L., Chaikin, P. M., Gollub, J. P., and Pine, D. J. (2008). Random organization in periodically driven systems. *Nature Physics*, 4(5):420–424.

[32] da Rocha, H. B. and Truskinovsky, L. (2020). Rigidity-controlled crossover: From spinodal to critical failure. *Physical Review Letters*, 124(1):015501.

[33] Dahmen, K. A., Ben-Zion, Y., and Uhl, J. T. (2009). Micromechanical model for deformation in solids with universal predictions for stress-strain curves and slip avalanches. *Phys. Rev. Lett.*, 102:175501.

[34] Denisov, D. V., Dang, M. T., Struth, B., Zaccone, A., Wegdam, G. H., and Schall, P. (2015). Sharp symmetry-change marks the mechanical failure transition of glasses. *Scientific reports*, 5(1):1–8.

[35] Deutsch, J., Dhar, A., and Narayan, O. (2004). Return to return point memory. *Physical review letters*, 92(22):227203.

[36] Deutsch, J. M. and Narayan, O. (2003). Subharmonics and aperiodicity in hysteresis loops. *Physical review letters*, 91(20):200601.

[37] Eshelby, J. D. (1957a). The determination of the elastic field of an ellipsoidal inclusion, and related problems. *Proceedings of the royal society of London. Series A. Mathematical and physical sciences*, 241(1226):376–396.

[38] Eshelby, J. D. (1957b). The determination of the elastic field of an ellipsoidal inclusion, and related problems. *Proc. Roy. Soc. A*, 241:376–396.

[39] Falk, M. L. and Langer, J. S. (1998). Dynamics of viscoplastic deformation in amorphous solids. *Physical Review E*, 57(6):7192.

[40] Fernández Castellanos, D., Roux, S., and Patinet, S. (2021). Insights from the quantitative calibration of an elasto-plastic model from a Lennard-Jones atomic glass. *C. R. Phys.*, 22:135–162.

[41] Ferrero, E. E. and Jagla, E. A. (2019). Criticality in elastoplastic models of amorphous solids with stress-dependent yielding rates. *Soft Matter*, 15:9041.

[42] Fiocco, D., Foffi, G., and Sastry, S. (2013). Oscillatory athermal quasistatic deformation of a model glass. *Physical Review E*, 88(2):020301.

[43] Fiocco, D., Foffi, G., and Sastry, S. (2014). Encoding of memory in sheared amorphous solids. *Physical review letters*, 112(2):025702.

[44] Galloway, K., Teich, E., Ma, X., Kammer, C., Graham, I., Keim, N., Reina, C., Jerolmack, D., Yodh, A., and Arratia, P. (2022). Relationships between structure, memory and flow in sheared disordered materials. *Nature Physics*, 18(5):565–570.

[45] Gilbert, I., Chern, G.-W., Fore, B., Lao, Y., Zhang, S., Nisoli, C., and Schiffer, P. (2015). Direct visualization of memory effects in artificial spin ice. *Physical Review B*, 92(10):104417.

[46] Hébraud, P. and Lequeux, F. (1998). Mode-coupling theory for the pasty rheology of soft glassy materials. *Physical review letters*, 81(14):2934.

[47] Herschel, W. H. and Bulkley, R. (1926). Konsistenzmessungen von gummi-benzollösungen. *Kolloid-Zeitschrift*, 39:291–300.

[48] Homer, E. R., Rodney, D., and Schuh, C. A. (2010). Kinetic monte carlo study of activated states and correlated shear-transformation-zone activity during the deformation of an amorphous metal. *Physical Review B*, 81(6):064204.

[49] Homer, E. R. and Schuh, C. A. (2009). Mesoscale modeling of amorphous metals by shear transformation zone dynamics. *Acta Mat.*, 57:2823–2833.

[50] Homer, E. R. and Schuh, C. A. (2010). Three-dimensional shear transformation zone dynamics model for amorphous metals. *Modelling and Simulation in Materials Science and Engineering*, 18(6):065009.

[51] Jagla, E. A. (2007). Strain localization driven by structural relaxation in sheared amorphous solids. *Phys. Rev. E*, 76:046119.

[52] Jana, P. K., Alava, M. J., and Zapperi, S. (2017). Irreversibility transition of colloidal polycrystals under cyclic deformation. *Scientific Reports*, 7(1):1–8.

[53] Kawasaki, T. and Berthier, L. (2016). Macroscopic yielding in jammed solids is accompanied by a nonequilibrium first-order transition in particle trajectories. *Physical Review E*, 94(2):022615.

[54] Keim, N. C. and Arratia, P. E. (2014). Mechanical and microscopic properties of the reversible plastic regime in a 2d jammed material. *Physical review letters*, 112(2):028302.

[55] Keim, N. C., Hass, J., Kroger, B., and Wieker, D. (2020). Global memory from local hysteresis in an amorphous solid. *Physical Review Research*, 2(1):012004.

[56] Keim, N. C. and Medina, D. (2022). Mechanical annealing and memories in a disordered solid. *Science Advances*, 8(40):eabo1614.

[57] Keim, N. C. and Nagel, S. R. (2011). Generic Transient Memory Formation in Disordered Systems with Noise. *Phys. Rev. Lett.*, 107:010603.

[58] Keim, N. C. and Paulsen, J. D. (2021). Multiperiodic orbits from interacting soft spots in cyclically sheared amorphous solids. *Science Advances*, 7(33):eabg7685.

[59] Keim, N. C., Paulsen, J. D., Zeravcic, Z., Sastry, S., and Nagel, S. R. (2019). Memory formation in matter. *Reviews of Modern Physics*, 91(3):035002.

[60] Khirallah, K., Tyukodi, B., Vandembroucq, D., and Maloney, C. E. (2021). Yielding in an integer automaton model for amorphous solids under cyclic shear. *Phys. Rev. Lett.*, 126:218005.

[61] Kumar, D., Patinet, S., Maloney, C. E., Regev, I., Vandembroucq, D., and Mungan, M. (2022). Mapping out the glassy landscape of a mesoscopic elastoplastic model. *The Journal of Chemical Physics*, 157(17).

[62] Landau, L. D., Lifšic, E. M., Lifshitz, E. M., Kosevich, A. M., and Pitaevskii, L. P. (1986). *Theory of elasticity: volume 7*, volume 7. Elsevier.

[63] Lavrentovich, M. O., Liu, A. J., and Nagel, S. R. (2017). Period proliferation in periodic states in cyclically sheared jammed solids. *Physical Review E*, 96(2):020101.

[64] Le Bouil, A., Amon, A., McNamara, S., and Crassous, J. (2014). Emergence of cooperativity in plasticity of soft glassy materials. *Physical review letters*, 112(24):246001.

[65] Lees, A. and Edwards, S. (1972). The computer study of transport processes under extreme conditions. *Journal of Physics C: Solid State Physics*, 5(15):1921.

[66] Leishangthem, P., Parmar, A. D., and Sastry, S. (2017). The yielding transition in amorphous solids under oscillatory shear deformation. *Nature communications*, 8(1):1–8.

[67] Lemaître, A. and Caroli, C. (2009). Rate-Dependent Avalanche Size in Athermally Sheared Amorphous Solids. *Physical Review Letters*, 103(6):065501.

[68] Lerner, E. and Procaccia, I. (2009). Locality and nonlocality in elastoplastic responses of amorphous solids. *Physical Review E*, 79(6):066109.

[69] LIFSHITZ, E., KOSEVICH, A., and PITAEVSKII, L. (1986). Chapter iv - dislocations. In LIFSHITZ, E., KOSEVICH, A., and PITAEVSKII, L., editors, *Theory of Elasticity (Third Edition)*, pages 108–132. Butterworth-Heinemann, Oxford, third edition edition.

[70] Lin, J., Lerner, E., Rosso, A., and Wyart, M. (2014). Scaling description of the yielding transition in soft amorphous solids at zero temperature. *Proc. Nat. Acd. Sci.*, 111:14382–14387.

[71] Lin, J. and Wyart, M. (2016). Mean-field description of plastic flow in amorphous solids. *Physical review X*, 6(1):011005.

[72] Lindeman, C. W. and Nagel, S. R. (2021). Multiple memory formation in glassy landscapes. *Science Advances*, 7(33):eabg7133.

[73] Liu, C., Ferrero, E. E., Jagla, E. A., Martens, K., Rosso, A., and Talon, L. (2022). The fate of shear-oscillated amorphous solids. *The Journal of Chemical Physics*, 156(10):104902.

[74] Ma, Y., Ye, J., Peng, G., Wen, D., and Zhang, T. (2015). Nanoindentation study of size effect on shear transformation zone size in a Ni–Nb metallic glass. *Materials Science and Engineering: A*, 627:153–160.

[75] Maloney, C. E. and Lemaître, A. (2006). Amorphous systems in athermal, quasistatic shear. *Physical Review E*, 74(1):16118–16118.

[76] Maloney, C. E. and Robbins, M. O. (2008). Evolution of displacements and strains in sheared amorphous solids. *Journal of Physics: Condensed Matter*, 20(24):244128.

[77] Mukherji, S., Kandula, N., Sood, A., and Ganapathy, R. (2019). Strength of mechanical memories is maximal at the yield point of a soft glass. *Physical review letters*, 122(15):158001.

[78] Mungan, M., Sastry, S., Dahmen, K., and Regev, I. (2019). Networks and hierarchies: How amorphous materials learn to remember. *Physical Review Letters*, 123:178002.

[79] Mungan, M. and Terzi, M. M. (2019). The structure of state transition graphs in hysteresis models with return point memory: I. general theory. *Ann. Henri Poincaré*.

[80] Nagasawa, K., Miyazaki, K., and Kawasaki, T. (2019). Classification of the reversible–irreversible transitions in particle trajectories across the jamming transition point. *Soft matter*, 15(38):7557–7566.

[81] Nicolas, A. and Barrat, J.-L. (2013). Spatial cooperativity in microchannel flows of soft jammed materials: a mesoscopic approach. *Physical review letters*, 110(13):138304.

[82] Nicolas, A., Ferrero, E., Martens, K., and Barrat, J.-L. (2015). Deformation and flow of amorphous solids: a review of mesoscale elastoplastic models. *Rev. Mod. Phys.*, 90:045006.

[83] Nicolas, A., Martens, K., and Barrat, J.-L. (2014a). Rheology of athermal amorphous solids: Revisiting simplified scenarios and the concept of mechanical noise temperature. *EPL*, 107(4).

[84] Nicolas, A. and Rottler, J. (2018). Orientation of plastic rearrangements in two-dimensional model glasses under shear. *Physical Review E*, 97(6):063002.

[85] Nicolas, A., Rottler, J., and Barrat, J.-L. (2014b). Spatiotemporal correlations between plastic events in the shear flow of athermal amorphous solids. *The European Physical Journal E*, 37(6).

[86] Ozawa, M., Berthier, L., Biroli, G., Rosso, A., and Tarjus, G. (2018). Random critical point separates brittle and ductile yielding transitions in amorphous materials. *Proceedings of the National Academy of Sciences*, 115(26):6656–6661.

[87] Ozawa, M., Berthier, L., Biroli, G., and Tarjus, G. (2020). Role of fluctuations in the yielding transition of two-dimensional glasses. *Physical Review Research*, 2(2):023203.

[88] Ozawa, M., Berthier, L., Biroli, G., and Tarjus, G. (2022). Rare events and disorder control the brittle yielding of well-annealed amorphous solids. *Physical Review Research*, 4(2):023227.

[89] Panagopoulos, C., Majoros, M., Nishizaki, T., and Iwasaki, H. (2006). Weak magnetic order in the normal state of the high-t c superconductor la 2- x sr x cuo 4. *Physical review letters*, 96(4):047002.

[90] Parmar, A. D., Kumar, S., and Sastry, S. (2019). Strain localization above the yielding point in cyclically deformed glasses. *Physical Review X*, 9(2):021018.

[91] Patinet, S., Barbot, A., Lerbinger, M., Vandembroucq, D., , and Lemaître, A. (2020). Origin of the bauschinger effect in amorphous solids. *Physical Review Letters*, 124:205503.

[92] Patinet, S., Vandembroucq, D., Hansen, A., and Roux, S. (2014). Cracks in random brittle solids: From fiber bundles to continuum mechanics. *The European Physical Journal Special Topics*, 223(11):2339–2351.

[93] Paulsen, J. D., Keim, N. C., and Nagel, S. R. (2014). Multiple transient memories in experiments on sheared non-brownian suspensions. *Physical review letters*, 113(6):068301.

[94] Picard, G., Ajdari, A., Lequeux, F., and Bocquet, L. (2004). Elastic consequences of a single plastic event: A step towards the microscopic modeling of the flow of yield stress fluids. *The European Physical Journal E*, 15(4):371–381.

[95] Picard, G., Ajdari, A., Lequeux, F., and Bocquet, L. (2005). Slow flows of yield stress fluids: Complex spatiotemporal behavior within a simple elastoplastic model. *Physical Review E*, 71(1):010501.

[96] Pine, D. J., Gollub, J. P., Brady, J. F., and Leshansky, A. M. (2005). Chaos and threshold for irreversibility in sheared suspensions. *Nature*, 438(7070):997–1000.

[97] Preisach, F. (1935). Über die magnetische nachwirkung. *Zeitschrift für physik*, 94(5-6):277–302.

[98] Priezjev, N. V. (2013). Heterogeneous relaxation dynamics in amorphous materials under cyclic loading. *Physical Review E*, 87(5):052302.

[99] Princen, H. (1983). Rheology of foams and highly concentrated emulsions: I. elastic properties and yield stress of a cylindrical model system. *Journal of Colloid and interface science*, 91(1):160–175.

[100] Puosi, F., Olivier, J., and Martens, K. (2015). Probing relevant ingredients in mean-field approaches for the athermal rheology of yield stress materials. *Soft Matter*, 11(38):7639–7647.

[101] Regev, I., Attia, I., Dahmen, K., Sastry, S., and Mungan, M. (2021). Topology of the energy landscape of sheared amorphous solids and the irreversibility transition. *Physical Review E*, 103(6):062614.

[102] Regev, I. and Lookman, T. (2018). Critical diffusivity in the reversibility–irreversibility transition of amorphous solids under oscillatory shear. *Journal of Physics: Condensed Matter*, 31(4):045101.

[103] Regev, I., Lookman, T., and Reichhardt, C. (2013). Onset of irreversibility and chaos in amorphous solids under periodic shear. *Physical Review E*, 88(6):062401.

[104] Regev, I., Weber, J., Reichhardt, C., Dahmen, K. A., and Lookman, T. (2015). Reversibility and criticality in amorphous solids. *Nature communications*, 6(1):8805.

[105] Reichhardt, C., Regev, I., Dahmen, K., Okuma, S., and Reichhardt, C. (2023). Reversible to irreversible transitions in periodic driven many-body systems and future directions for classical and quantum systems. *Physical Review Research*, 5(2):021001.

[106] Rodney, D., Tanguy, A., and Vandembroucq, D. (2011). Modeling the mechanics of amorphous solids at different length scale and time scale. *Modelling and Simulation in Materials Science and Engineering*, 19(8):083001.

[107] Rossi, S. and Tarjus, G. (2022). Emergence of a random field at the yielding transition of a mean-field Elato-Plastic model. *arxiv*, page 2201.06388.

[108] Ruan, D., Patinet, S., and Falk, M. L. (2022). Predicting plastic events and quantifying the local yield surface in 3d model glasses. *Journal of the Mechanics and Physics of Solids*, 158:104671.

[109] Salmon, J. K., Moraes, M. A., Dror, R. O., and Shaw, D. E. (2011). Parallel Random Numbers: As easy as 1, 2, 3. *SC'11: Proceedings of 2011 International Conference for High Performance Computing, Networking, Storage and Analysis*, pages 1–12.

[110] Schall, P., Weitz, D. A., and Spaepen, F. (2007). Structural Rearrangements That Govern Flow in Colloidal Glasses. *Science*, 318(5858):1895–1899.

[111] Schuh, C., Hufnagel, T., and Ramamurty, U. (2007). Mechanical behavior of amorphous alloys. *Acta Materialia*, 55(12):4067–4109.

[112] Schuh, C. A. and Lund, A. C. (2003). Atomistic basis for the plastic yield criterion of metallic glass. *Nature Materials*, 2(7):449–452.

[113] Sethna, J. P., Dahmen, K., Kartha, S., Krumhansl, J. A., Roberts, B. W., and Shore, J. D. (1993). Hysteresis and hierarchies: Dynamics of disorder-driven first-order phase transformations. *Physical Review Letters*, 70(21):3347.

[114] Sethna, J. P., Dahmen, K. A., and Perkovic, O. (2004). Random-field ising models of hysteresis. *arXiv preprint cond-mat/0406320*.

[115] Shi, Y. and Falk, M. (2005). Strain localization and percolation of stable structure in amorphous solids. *Physical Review Letters*, 95(9).

[116] Shohat, D., Hexner, D., and Lahini, Y. (2022). Memory from coupled instabilities in unfolded crumpled sheets. *Proceedings of the National Academy of Sciences*, 119(28):e2200028119.

[117] Singh, M., Ozawa, M., and Berthier, L. (2020). Brittle yielding of amorphous solids at finite shear rates. *Physical Review Materials*, 4(2):025603.

[118] Sollich, P., Lequeux, F., Hébraud, P., and Cates, M. E. (1997). Rheology of soft glassy materials. *Physical review letters*, 78(10):2020.

[119] Srolovitz, D., Vitek, V., and Egami, T. (1983). An atomistic study of deformation of amorphous metals. *Acta Metallurgica*, 31(2):335–352.

[120] Talamali, M., Petäjaä, V., Vandembroucq, D., and Roux, S. (2012). Strain localization and anisotropic correlations in a mesoscopic model of amorphous plasticity. *Comptes Rendus Mécanique*, 340(4-5):275–288.

[121] Tanguy, A., Leonforte, F., and Barrat, J. L. (2006). Plastic response of a 2D Lennard-Jones amorphous solid: Detailed analysis of the local rearrangements at very slow strain rate. *The European Physical Journal E*, 20(3):355–364.

[122] Taylor, G. I. (1967). Film notes for low reynolds number flow. *Illustrated Experiments in Fluid Mechanics: The National Committee for Fluid Mechanics Films Book of Film Notes*.

[123] Terzi, M. M. and Mungan, M. (2020). State transition graph of the preisach model and the role of return-point memory. *Physical Review E*, 102(1):012122.

[124] Tyukodi, B., Barbot, A., García-García, R., Lerbinger, M., Patinet, S., and Vandembroucq, D. (2023). Coarse-graining amorphous plasticity: impact of rejuvenation and disorder. *Comptes Rendus. Physique*, 24(S1):1–19.

[125] Tyukodi, B., Patinet, S., Roux, S., and Vandembroucq, D. (2016). From depinning transition to plastic yielding of amorphous media: A soft modes perspective. *Phys. Rev. E*, 93:063005.

[126] Tyukodi, B., Vandembroucq, D., and Maloney, C. E. (2018). Diffusion in Mesoscopic Lattice Models of Amorphous Plasticity. *Physical Review Letters*, 121(14).

[127] van Hecke, M. (2021). Profusion of transition pathways for interacting hysterons. *Physical Review E*, 104(5):054608.

[128] Vandembroucq, D. and Roux, S. (2011). Mechanical noise dependent aging and shear-banding behavior in a mesoscopic model of amorphous plasticity. *Phys. Rev. B*, 84:134210.

[129] Yeh, W.-T., Ozawa, M., Miyazaki, K., Kawasaki, T., and Berthier, L. (2020). Glass stability changes the nature of yielding under oscillatory shear. *Physical review letters*, 124(22):225502.

## RÉSUMÉ

Les solides amorphes (verres, polymères, émulsions, etc.) sont omniprésents dans notre vie quotidienne. Lorsqu'ils sont soumis à une contrainte externe importante, ils s'écoulent et/ou se cassent. Comprendre leurs propriétés mécaniques est donc une question d'importance à la fois fondamentale, mais aussi une technologique. Nous construisons un nouveau modèle élasto-plastique minimal pour étudier la déformation dans les solides amorphes soumis à un cisaillement oscillatoire. Sous l'effet des oscillations, ces matériaux peuvent atteindre des cycles limites entièrement réversibles et même encoder une mémoire, par exemple, de l'amplitude du forçage. Notre modèle permet de saisir ces effets de mémoire et de comprendre leur dépendance à l'égard des protocoles de préparation, d'apprentissage et de lecture. Nous étudions également l'effet du vieillissement sur la transition d'écoulement et utilisons une technique de graphe de transition pour analyser les résultats.

## MOTS CLÉS

mémoire, plasticité, amorphe, cycles limites, graphes de transitioon

## ABSTRACT

Amorphous solids, ranging from hard glasses to soft materials such as polymers and emulsions are ubiquitous in our daily life. When subjected to large external stress they yield and display plastic flow and/or break. Understanding the mechanisms governing their mechanical properties is therefore a question of both fundamental importance and technological significance. We build a novel and minimal elasto-plastic model to study yielding in amorphous solids under oscillatory shear. Under oscillatory driving such materials can reach fully reversible limit cycles and even encode memory, for example, of the amplitude of forcing. We capture such memory effects through our model and understand their dependence on yielding, training and read-out protocols. We also study the effect of glass preparation on the approach to the yielding transition and use a transition graph technique to analyse our results. Finally, we discuss mechanical training protocols designed to store multiple memories.

## KEYWORDS

memory, plasticity, amorphous, limit cycles, transition graphs